Challenge Journal of STRUCTURAL MECHANICS

Vol.8 No.3 (2022)

Mindlin's theory buckling columns compressive strength dynamic analysis dynamic response earthquake finite element analysis finite element method mechanical properties metaheuristic algorithms modal analysis natural frequency optimization pushover analysis reinforced concrete seismic analysis seismic design seismic isolation steel silo teaching-learning based optimization [illegible]plate

TULPAR ACADEMIC PUBLISHING

ISSN 2149-8024

Challenge Journal of Structural Mechanics

E-mail: *cjsmec@challengejournal.com*

Web page: *cjsmec.challengejournal.com*

TULPAR Academic Publishing
www.tulparpublishing.com

Challenge Journal of Structural Mechanics

CONTENTS

Research Articles

TULPAR ACADEMIC PUBLISHING

Challenge Journal of Structural Mechanics

Research Article

Robustness evaluation of optimum tuned liquid dampers for uncertain variable loading of structures

Ayla Ocak [a], Gebrail Bekdaş [a], Sinan Melih Nigdeli [a,*]

[a] *Department of Civil Enginering, İstanbul University-Cerrahpaşa, 34320 İstanbul, Turkey*

ABSTRACT

This study focuses on the performance analysis of optimum tuned liquid dampers (TLDs) under the different live loads of three different structure models, designed as both single and multi-story, under earthquake excitations. For this purpose, single, ten, and forty story structure models have been created and tuned liquid damping devices that contain liquids of different densities and viscosities such as acetone, mercury, and seawater are placed on the structure. For the analysis conducted under earthquake excitations, optimum damping device parameters were previously obtained with the Adaptive Harmony Search Algorithm (AHS), and minimizing the movement of the structure was aimed. The effect of the damping device on the control performance was investigated under increasing and decreasing live loads for the uncertain mass of the structure because of variable actions. When the results are examined, it has been determined that the increase in the story number of the structure will less affect the displacement reduction performance of TLDs for the structure under uncertain variable loading.

ARTICLE INFO

Article history:
Received 28 March 2022
Revised 1 May 2022
Accepted 20 May 2022

Keywords:
Tuned liquid damper
Structural control
Optimization
Adaptive harmony search

1. Introduction

Tuned liquid dampers (TLD) are passive control systems that dampen the movement by utilizing the spring stiffness and the sloshing energy of a liquid mass. Similar to other passive control systems, it provides control with the help of the main mass it contains. TLDs are designed according to the selected mass ratio considering the structure mass. However, apart from the mass of the initially accepted structure, the effect of live loads affecting the movement of the structure should be investigated. In structures, the off-tuning of the live load has been investigated for situations such as vibration tests and the addition of a mass damper. Setareh et al. (2006) investigated pendulum-type mass dampers and the optimum values were tested for possible mass change in the controlled floor system. Xing et al. (2014) proposed a tuned mass damper type counterweight for cable-stayed bridges under wind excitation to reduce the live-load amount. The increase in the damping of live loads in suspension bridges due to the mass damper-like motion caused by the presence of vehicles has been investigated in various studies (Wibowo et al. 2014; Shaban et al. 2015). In their study, Venanzi and Materazzi (2013) investigated the effect of uncertain mass distribution on floors in hybrid control of high-rise buildings under the influence of wind loads and conducted a hybrid control design that is resistant to uncertainties in load distribution. In the design of both single and multi-story structures, situations such as the increase in the number of visitors depending on the purpose of use of the structure make it necessary to investigate the live load situation.

TLDs are also known as liquid mass-containing types of tuned mass dampers (TMDs). Due to the presence of a liquid mass in it, the period of the sloshing liquid and its stable mass are both considered in the design. Appropriate selection of the characteristic properties of liquids facilitates control. Properties such as the density and kinematic viscosity of the TLD liquid have been observed in studies that modified TLD derivatives in which various mixtures, balls, and mixtures are used together to have a

* *Corresponding author*. Tel.: +90-212-473-7070 ; Fax: +90-212-473-7176 ; E-mail address: melihnig@iuc.edu.tr (S. M. Nigdeli)
ISSN: 2149-8024 / DOI: https://doi.org/10.20528/cjsmec.2022.03.001

churning and damping effect (Hitchcock et al. 1997; Tanveer et al. 2020; Shah et al. 2022). It is known that the optimization of these parameters with various optimization methods can increase control efficiency. Generally, parametric optimization has been performed for TLDs since the 90s (Gao et al. 1997; Xue et al. 2000; Taflanidis et al. 2005; Shum 2009; Debbarma et al. 2010; Mehrikan and Altay 2020; Ocak et al. 2022).

In this study, the optimum TLD parameters obtained from the Ocak et al. (2022) using different liquids with single-story, ten-story, and 40-story structure models were investigated for different structure mass situations on the same structure models. The optimum parameters for a constant mass of the structure are taken in all cases and possible changes in live loads were considered for TLD performance. All comparisons of the control system were done with the results of uncontrolled structure with the changing masses. As known, the most effective index in the optimum tuning of mass dampers is the critical natural frequency of the structure, and the mass change will change the frequency of the structure and the optimum TLD system may get out of tune.

In their study, Ocak et al. (2022) investigated the effects of viscosity and density on the selection of the optimum TLD liquid of different liquids and different structure models. In the results obtained for a single-story structure, it was determined that less dense liquid with lower viscosity is optimum, as the number of stories increases, viscosity, and density are desired to be higher, and in heavy structures such as 40 floors, viscosity loses its importance and density comes to the fore (Ocak et al. 2022). In this study, considering the work of Ocak et al. (2022), acetone and mercury liquids, which are the optimum TLD liquids obtained in the single-story and forty-story structure model, were used. In the ten-story structure model they used in the study, propanol and seawater liquids were very close in percentage, and small fractional differences were found. In the study, seawater liquid was preferred for the ten-story structure model, since it would be more cost-effective to obtain seawater.

Critical earthquake analysis was carried out for all cases. The control performance of TLDs has been investigated in case the structure mass changes. FEMA records, which include 22 earthquake records, were excited as an excitation to the structure models via Matlab Simulink (FEMA P-695 2009; Matlab 2018). Analyzes were made using optimum TLD parameters and optimum liquid. The effect of the increase and decrease in the mass of the multi-story structure models on the damper performance has been investigated. Performance analysis was made by increasing or decreasing the structure mass up to 25%. The impact of structure and variable actions on TLD performance has been researched. The results obtained for the multi-story structures were compared with the mass change results obtained in the single-story structure model obtained by Ocak et al. (2022).

2. Design of Tuned Liquid Dampers

2.1. Equations of motion

Tuned liquid dampers dampen the movement of the structure with the mechanical energy arising from the sloshing of the liquid in the tank. The main parameters affecting this energy depend on the damper mass, tank geometry and period, and properties such as damping ratio. It is suggested in the literature that the mass ratio of TLDs can be selected between 1-5%, considering the recommended ratio for mass dampers (Sun et al. 1992; Yu et al. 1999; Vickery et al. 1983; Rana and Soong 1998). In the sloshing model of a cylindrical tank created according to the linear hydrodynamic theory, TLD liquid is divided into two sloshing and non-sloshing liquids (Abramson 1966). It is designed according to the assumption that while the sloshing liquid moves with separate freedom, the inactive liquid moves together with the tank. In Fig. 1, the TLD mechanical model placed on a single-story structure is given.

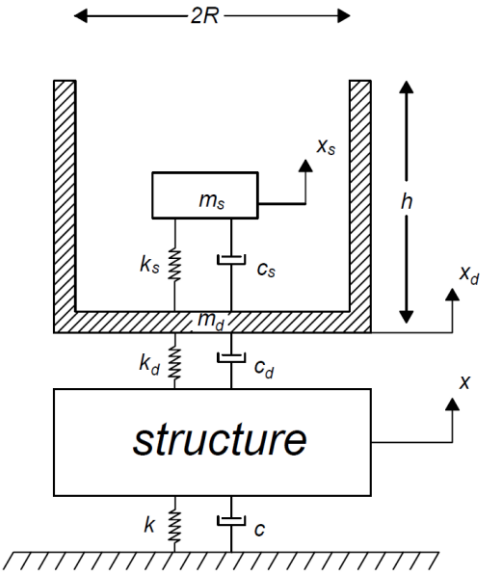

Fig. 1. Cylindrical TLD model placed in a single-story structure (Ocak et al. 2022).

For the calculation of the sloshing liquid mass, the damping ratio parameter (ξmn) with tangential (m) and radial (n) directions, which is expressed as the roots of the Bessel function used in the wave propagation of cylindrical bodies, is used (Sharma et al. 2019). By setting this parameter to the 1st Vibration mode, the sloshing liquid mass equation is created with a coefficient of 1.84, and by using it in the calculation of the lateral forces in the tank, the frequency and stiffness of the sloshing liquid are calculated (Bauer 1964; Rouf 2005; Sharma et al. 2019). The calculation of the sloshing active liquid mass (m_s) in the tank is shown in Eq. (1).

$$m_s = m_{st} \times R \times \frac{\tanh\left(\frac{1.84h}{R}\right)}{2.2h} \quad (1)$$

where m_{st} is the total mass of liquid in the tank, R is the radius of the cylindrical tank and h is the height of the liquid in the tank.

The non-sloshing liquid, which represents the second freedom of the damper, and the mass in which the tank moves together are expressed as m_d. It is obtained by subtracting the mass of sloshing liquid from the total mass of TLD (m_{TLD}). In Eq. (2), the empty mass of the tank and the total mass of the liquid that is not sloshing (m_d) are calculated.

$$m_d = m_{TLD} - m_s \tag{2}$$

The stiffnesses (k_d and k_s) of the damper and the sloshing liquid are shown in Eqs. (3) and (4), respectively, and the damping coefficients (c_d and c_s) are shown in Eqs. (5) and (6), respectively.

The stiffnesses (k_d and k_s) of the damper and the sloshing liquid are shown in Eqs. (3) and (4), respectively, and the damping coefficients (c_d and c_s) are shown in Eqs. (5) and (6), respectively.

$$k_d = m_d \times \left(\frac{2\pi}{T_d}\right)^2 \tag{3}$$

$$k_s = m_{st} \times \frac{g\left\{\tanh\left(\frac{1.84h}{R}\right)\right\}^2}{1.19h} \tag{4}$$

$$c_d = 2 \times \zeta_d \times \sqrt{m_d \times k_d} \tag{5}$$

$$c_s = \zeta_s \times 2\sqrt{m_s k_s} \tag{6}$$

The T_d parameter used in Eq. (3) represents the period of the damper tank. The damping ratio (ζ_d) of the damper is given in Eq. (7). The damping ratio (ζ_s) calculation of the shaking is obtained by experimental studies and calculated as in Eq. (8).

$$\zeta_d = \frac{c_d}{2m_d\sqrt{\frac{k_d}{m_d}}} \tag{7}$$

$$\zeta_s = 4.98 v^{\frac{1}{2}} R^{-\frac{3}{4}} g^{-\frac{1}{4}} \left[1 + \frac{0.318}{\sinh\left(\frac{1.84h}{R}\right)} \frac{1-\frac{h}{R}}{\cosh\left(\frac{1.84h}{R}\right)}\right] \tag{8}$$

The g in the equations denotes the gravitational acceleration and v denotes the kinematic viscosity.

The equation of motion of the system in its simplest form, which includes the information about the sloshing liquid, TLD tank + passive liquid, and structure, is shown in Eq. (9), and the mass, stiffness, and damping coefficient matrices are shown in Eq. (10-12), respectively. Terms such as mass, stiffness, and damping coefficient of the structure are included without indexes in the equations.

$$[M]\{\ddot{X}\} + [C]\{\dot{X}\} + [K]\{X\} = -[M]\{1\}\,\ddot{X}_g \tag{9}$$

A dot in the equations represents the velocity vector, the double dot represents the acceleration vector. Parameter $\ddot{X}_a$ with double dot specifies ground acceleration. {1} represents a vector of ones.

$$[M] = \begin{bmatrix} m & 0 & 0 \\ 0 & m_d & 0 \\ 0 & 0 & m_s \end{bmatrix} \tag{10}$$

$$[K] = \begin{bmatrix} k + k_d & -k_d & 0 \\ -k_d & k_d + k_s & -k_s \\ 0 & -k_s & k_s \end{bmatrix} \tag{11}$$

$$[C] = \begin{bmatrix} c + c_d & -c_d & 0 \\ -c_d & c_d + c_s & -c_s \\ 0 & -c_s & c_s \end{bmatrix} \tag{12}$$

3. Numerical Examples

In this study, a structure model with three different floors was used. A single-story structure with a weight of 100 tons, a ten-story structure with a weight of 3600 tons, and a forty-story structure with a weight of 39200 tons were designed. The single-story structure model is designed with 3 degrees of freedom (3DOF) taking into account the freedom of the structure, the sloshing liquid, and the TLD tank. Fig. 2 shows a single-story structure model. The period of the single-story structure was chosen as 1 second, and the stiffness and damping coefficients were taken as 3.95 MN/m and 0.06 MNs/m, respectively.

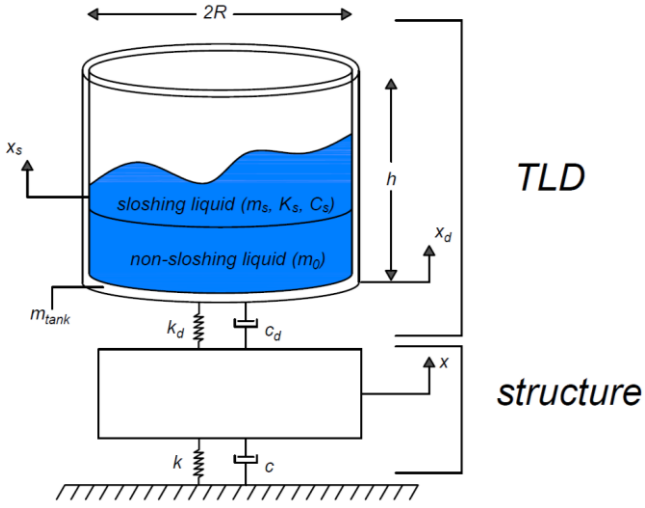

Fig. 2. Cylindrical TLD model placed in a single-story structure.

Twelve degrees of freedom (12DOF) as ten-story structure, ten-story freedom, sloshing liquid freedom, and TLD tank freedom were taken into account, and the structural stiffness and damping coefficient values were taken as 650 MN/m and 6.2 MNs/m, respectively (Singh et al. 2002). For the forty-story structure model, these values were used in the analysis as 2130 MN/m and 42.6 MNs/m on the first floor of the structure and 998 MN/m and 20 MNs/m on the last floor of the structure (Liu et

al. 2008). The multi-story structure model used is shown in Fig. 3. Here, the "*i*" index indicates the floor number, and the "*n*" index indicates the top floor number of the structure.

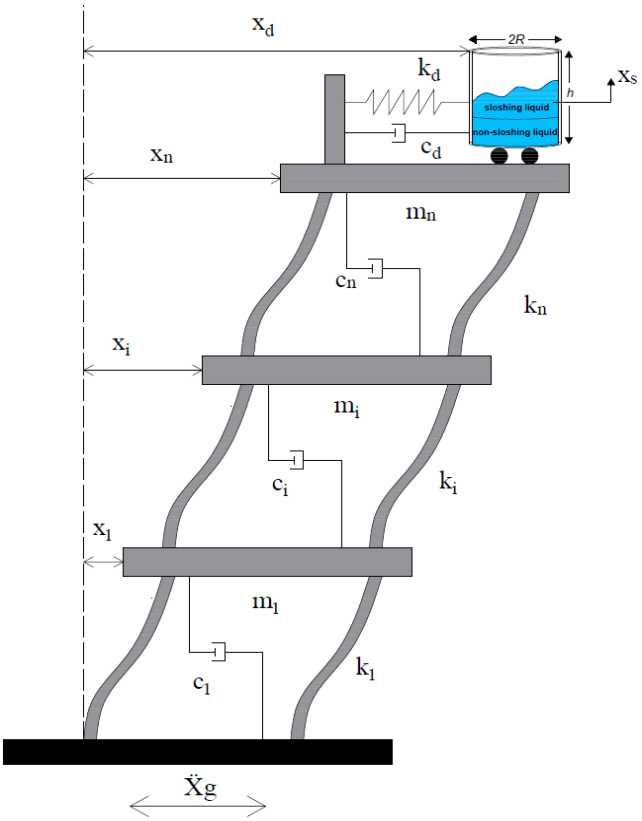

Fig. 3. Cylindrical TLD model placed in a multi-story structure.

TLDs are placed on the models created for the application. FEMA earthquake records consisting of various earthquakes were excited to the structures in Matlab Simulink and optimum results were found in Ocak et al. (2022). The earthquake records are listed in Table 1.

Ocak et al. (2022) determined that among the liquids they used, acetone for a single-story liquid, seawater for a ten-story structure, and mercury for a forty-story structure were the optimum liquids as TLD liquids. These liquid types were used for each structure model in which TLD was placed. The optimum TLD parameters for single-story, ten, and forty-story structure models are shown in Table 2.

As a result of the earthquake analysis, the critical earthquake record for the single-story and ten-story structures was DUZCE/BOL090, CHICHI/CHY101-N for the forty-story structure according to results in Ocak et al. (2022). In the analysis conducted with optimum TLD parameters, the effects of live loads on displacement and total acceleration with ∓25% mass change for selected liquids were investigated. The displacement and total acceleration values obtained under the effect of live loads for critical earthquake recording in a single-story, ten- and forty-story structure are shown in Table 3. In Table 3, the critical earthquake analysis results obtained from the multi-story building models are presented together with the mass change results on the single-story building model in the work of Ocak et al. (2022).

As a result of the critical earthquake analysis, the displacement-time and total acceleration-time graphs obtained at -25% mass decrease for a single-story structure are given in Fig. 4, and the displacement-time and total acceleration-time graphs obtained at +25% mass increase are also shown in Fig. 5.

Table 1. FEMA earthquake records list.

Earthquake Number	Date	Earthquake Name	Component 1	Component 2
1	1994	Northridge	NORTHR/MUL009	NORTHR/MUL279
2	1994	Northridge	NORTHR/LOS000	NORTHR/LA270
3	1999	Duzce, Turkey	DUZCE/BOL0000	DUZCE/BOL090
4	1999	Hector Mine	HECTOR/HEC000	HECTOR/HEC090
5	1979	Imperial Valley	IMPVALL/H-DLT262	IMPVALL/H-DLT352
6	1979	Imperial Valley	IMPVALL/H-E11140	IMPVALL/H-E11230
7	1995	Kobe, Japan	KOBE/NIS000	KOBE/NIS090
8	1995	Kobe, Japan	KOBE/SHI000	KOBE/SHI090
9	1999	Kocaeli, Turkey	KOCAELI/DZC180	KOCAELI/DZC270
10	1999	Kocaeli, Turkey	KOCAELI/ARC000	KOCAELI/ARC090
11	1992	Landers	LANDERS/PLACE270	LANDERS/YER360
12	1992	Landers	LANDERS/CLW-LN	LANDERS/CLW-TR
13	1989	Loma Prieta	LOMAP/CAP000	LOMAP/CAP090
14	1989	Loma Prieta	LOMAP/G03000	LOMAP/G03090
15	1990	Manjil, Iran	MANJIL/ABBAR--L	MANJIL/ABBAR--T
16	1987	Superstition Hills	SUPERST/B-ICC000	SUPERST/B-ICC090
17	1987	Superstition Hills	SUPERST/B-POE270	SUPERST/B-POE360
18	1992	Cape Mendocino	CAPEMEND/RIO270	CAPEMEND/RIO360
19	1999	Chi-Chi, Taiwan	CHICHI/CHY101-E	CHICHI/CHY101-N
20	1999	Chi-Chi, Taiwan	CHICHI/TCU045-E	CHICHI/TCU045-N
21	1971	San Fernando	SFERN/PEL090	SFERN/PEL180
22	1976	Friuli, Italy	FRIULI/A-TMZ000	FRIULI/A-TMZ270

Table 2. Optimum TLD parameters for single, ten, and forty story structure models (Ocak et al. 2022).

Variables	Single story structure	10-storey structure	40-storey structure
	Acetone	Seawater	Mercury
T_d (s)	0.9454	0.9962	3.5626
ζ_d	0.0810	0.1841	0.2270
R (m)	0.5418	1.1087	4.1312
h (m)	2.2884	0.7556	2.3684

Table 3. Displacement and total acceleration values obtained by the effect of live load in the critical earthquake record for single-story, ten and forty-story structure models.

Structure mass increase/decrease percentage	Single-story Structure with TLD-Acetone		10-story Structure with TLD-Seawater		40-story Structure with TLD-Mercury	
	Displacement (m)	Total Acceleration (m/s²)	Displacement (m)	Total Acceleration (m/s²)	Displacement (m)	Total Acceleration (m/s²)
-25%	0.2016451	10.5720449	0.2559605	15.1735650	1.0073726	5.0971812
-20%	0.2121752	10.4000571	0.2696159	15.2311032	1.0755072	4.8098033
-15%	0.2208049	10.1468190	0.2806673	15.1687362	1.1373364	5.0038573
-10%	0.2274021	9.8344712	0.2890280	14.9887245	1.1940244	5.2571767
-5%	0.2319002	9.4777271	0.2944632	14.7042480	1.2967174	5.2711654
0%	0.2343740	9.0757597	0.2971696	14.3177283	1.4018155	5.1254171
+5%	0.2386721	8.6500651	0.3031982	13.8256268	1.5088005	4.9823147
+10%	0.2446614	8.4727027	0.3104425	13.2362306	1.6210147	4.9097424
+15%	0.2493544	8.2673290	0.3160396	12.5673918	1.7406651	4.8223275
+20%	0.2526405	8.0375150	0.3198721	11.8227165	1.8659784	4.6367295
+25%	0.2544804	7.7830968	0.3219217	11.4095860	1.9924649	4.8080075

As a result of the critical earthquake analysis, the displacement-time and total acceleration-time graphs obtained at -25% mass decrease for the ten-story structure are shown in Fig. 6, and the displacement-time and total acceleration-time graphs obtained at +25% mass increase are also given in Fig. 7.

As a result of the critical earthquake analysis, the displacement-time and total acceleration-time graphs obtained at -25% mass decrease for the forty-story structure are reported in Fig. 8, and the displacement-time and total acceleration-time graphs obtained at +25% mass increase are plotted in Fig. 9.

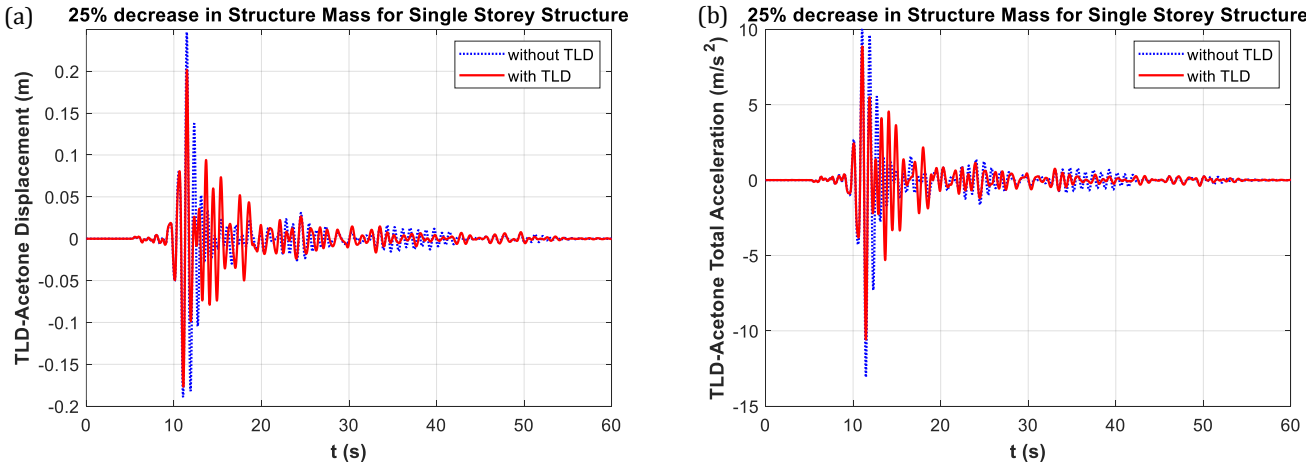

Fig. 4. Graphs obtained from the critical earthquake analysis for a single-story structure at a 25% mass decrease: (a) Displacement-time; (b) Total acceleration-time.

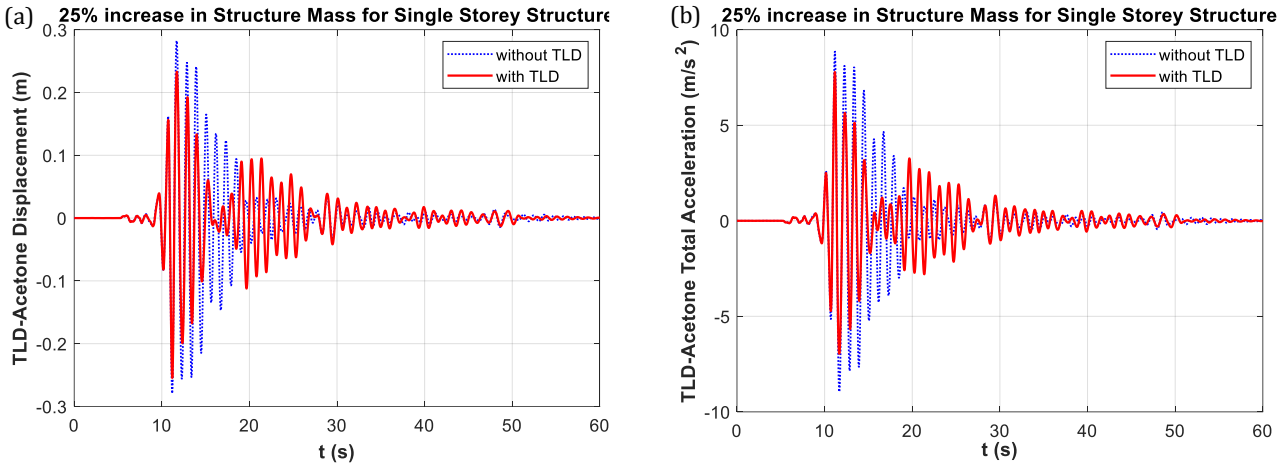

Fig. 5. Graphs obtained from the critical earthquake analysis for a single-story structure at a 25% mass increase: (a) Displacement-time; (b) Total acceleration time.

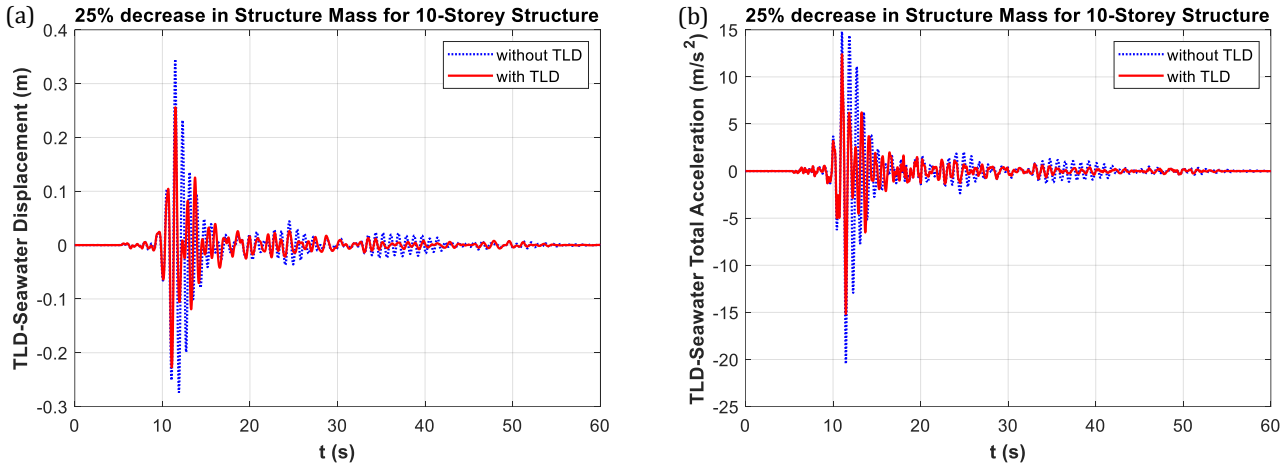

Fig. 6. Graphs obtained from the critical earthquake analysis for a 10-story structure at a 25% mass decrease: (a) Displacement-time; (b) Total acceleration-time.

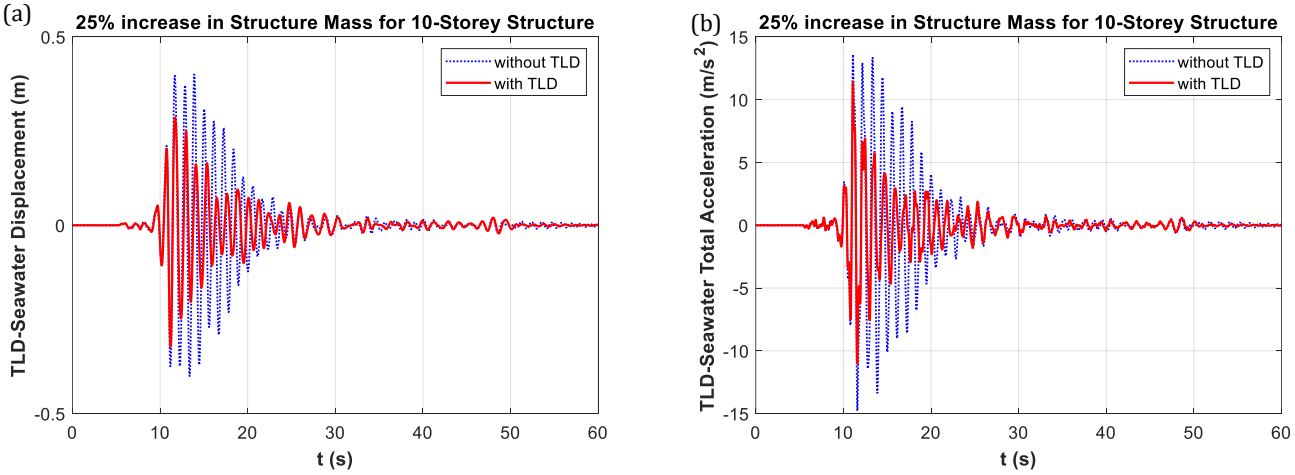

Fig. 7. Graphs obtained from the critical earthquake analysis for a 10-story structure at a 25% mass increase: (a) Displacement-time; (b) Total acceleration-time.

(b)

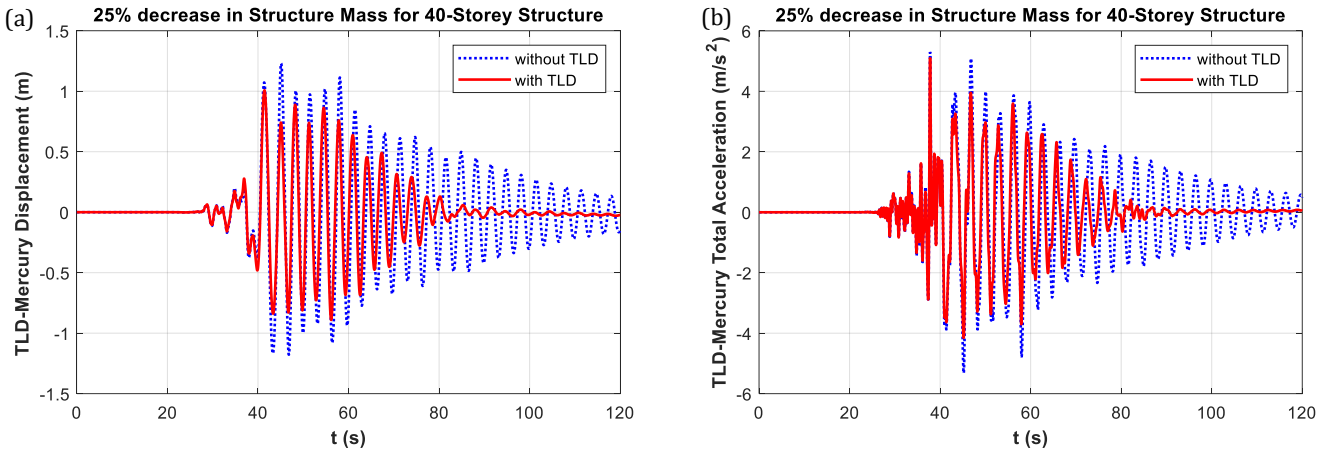

Fig. 8. Graphs obtained from the critical earthquake analysis for a 40-story structure at a 25% mass decrease: (a) Displacement-time; (b) Total acceleration-time.

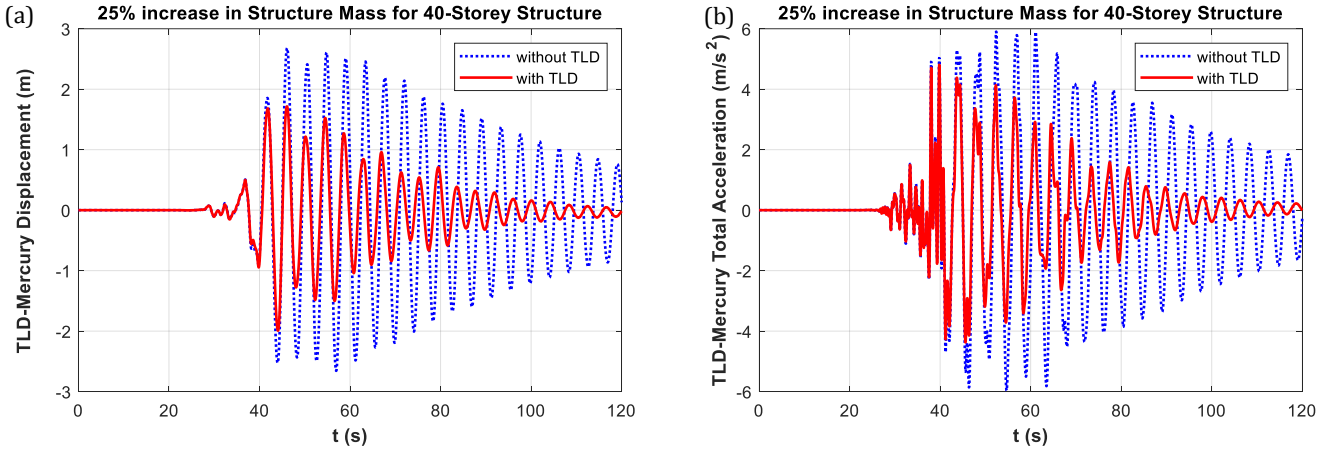

Fig. 9. Graphs obtained from the critical earthquake analysis for a 40-story structure at a 25% mass increase: (a) Displacement-time; (b) Total acceleration-time.

4. Discussion

In this study, analyzes were made under earthquake excitations to observe the effect of live load on single-story ten-story, and forty-story structure models using optimum TLD parameters and optimum liquid types. Critical earthquake record was determined in FEMA earthquake records for each structure model and TLD was analyzed under these earthquake excitations. Results evaluated for up to 25% increase and decrease of structure mass. In Table 4, displacement and total acceleration decrease percentages are given.

When Table 4 is examined, in the analyzes made for a single-story structure, the maximum displacement reduction performance was observed at a rate of 18.79%, and the minimum displacement reduction performance was observed at a rate of 9.91% when the structure mass was decreased by 15%. While the displacement reduction quality of TLDs shows an increasing graph up to the case where the structure mass is reduced by 15% for the example single-story structure model, the increased load state after this value is adversely affected. In the 100 tons model, the mass change in the structure with the effect of live load from 85 tons to 125 tons reduced the displacement reduction ability of TLD performance by approximately 9%. Although the total acceleration reduction performance did not lose as fast as the displacement with the increase in mass, each increase after the 5% increase in the mass also negatively affected the total acceleration. When comparing the optimum overall deceleration performance with the worst TLD performance, a performance loss of 7.5% is observed. For single-story structures, it can be said that the increase in mass significantly affects both the displacement and the overall acceleration reduction performance of TLDs.

In the ten-story structure analyzes, the maximum displacement reduction percentage of TLD was 27.55% and the minimum displacement reduction percentage was 19.67%. From the moment the mass started to be increased, the displacement reduction effect started to decrease, while each other increased mass percentage from the case where the mass was reduced by 10% also negatively affected the total acceleration. There is a performance loss for a displacement of about 8% and a reduction of total acceleration of 4%. It is seen that the live load effect does not significantly affect the TLD performance in terms of acceleration reduction of ten-story structures, but there is still a loss in displacement that should be noted.

Table 4. Displacement and total acceleration reduction percentages obtained by the effect of live load in the critical earthquake record for single-story, 10-storey, and 40-story structure models.

Structure mass increase/decrease percentage	Single-story Structure with TLD-Acetone		10-story Structure with TLD-Seawater		40-story Structure with TLD-Mercury	
	Displacement (m)	Total Acceleration (m/s²)	Displacement (m)	Total Acceleration (m/s²)	Displacement (m)	Total Acceleration (m/s²)
-25%	18.27	19.17	25.88	25.85	18.02	4.17
-20%	18.71	19.80	26.90	26.61	23.08	16.42
-15%	18.79	20.15	27.40	26.79	26.41	18.77
-10%	18.71	20.32	27.53	26.61	28.73	17.70
-5%	18.57	20.38	27.55	26.21	27.92	17.10
0%	18.43	20.44	27.54	25.75	27.28	16.98
+5%	17.13	20.52	26.19	25.44	26.96	17.32
+10%	14.88	18.23	24.17	25.29	26.79	17.93
+15%	12.86	16.16	22.25	25.26	26.55	18.38
+20%	11.17	14.40	20.78	25.31	26.15	18.68
+25%	9.91	13.02	19.67	22.70	25.66	19.36

In the critical earthquake analysis of the forty-story building model, each mass increase since the 10% reduction in the mass weakened the displacement reduction effect of the TLD. The maximum displacement reduction percentage, which was 28.73% for different structure mass situations given in Table 4, decreased to 25.66% as the mass increased. TLD performance loss was observed in terms of displacement reduction of approximately 3%. In the forty-story structure model, the increase in structure mass increased the overall acceleration performance by about 15%, in contrast to the decrease in displacement.

Above, the effect of change in structure mass on TLD displacement and total acceleration reductions is described. By converting TLD performance from the structure mass change to a percentage, it becomes easier to understand the effect of mass on performance. The optimum displacement reduction value in a single-story structure was observed at 15% mass reduction. From this to the case where the mass is increased by up to 25%, the TLD displacement reduction performance is reduced by approximately 47% and the total acceleration performance by approximately 37%. While the mass reduction in the ten-story structure affected the displacement reduction performance by approximately 6%, the 25% mass increase decreased the displacement and total acceleration reduction performance of the TLD by approximately 29% and 12%. In the forty-story structure example, the displacement reduction performance of the TLD decreased by approximately 10.7%, from 10% mass reduction where the optimum displacement reduction percentage was observed, to 25% mass increase. The effect of reducing the total acceleration showed a regular increase from 25% mass reduction to 25% mass increase. The overall deceleration performance of the TLD increased by approximately 8.6% for the final state of the increased mass from the state where the optimum displacement reduction percentage was shown.

5. Conclusions

According to the results, the following information is obtained.

- It is seen that the increase in mass of the structure creates a performance loss of approximately 47% for displacement and approximately 37% for total acceleration. It is understood that considering the live load effect in the design of a single-story structure is of great importance for the safety of the design.
- Although the live load creates less performance loss for a ten-story structure model than for a single-story structure, it is seen that the damper's displacement reduction performance affects 29% seriously and it should be taken into account in the designs.
- While decreasing the displacement reduction percentage in a forty-story structure, it is seen that the increase in mass has a positive effect on the damper in terms of reducing the total acceleration. There is a lower performance loss in terms of displacement compared to a single-story and ten-story structure. Based on this, it is understood that as the number of floors increases, the mass change decreases the effect of the damper on the displacement reduction performance.
- For the 40-story structure with TLD-Mercury, the mass change is not so effective on the change of the total acceleration values.

In light of all the information, it can be said that live loads can seriously affect the damper performance, especially in structures with a small number of floors.

Acknowledgements

None declared.

Funding

The authors received no financial support for the research, authorship, and/or publication of this manuscript.

Conflict of Interest

The authors declared no potential conflicts of interest with respect to the research, authorship, and/or publication of this manuscript.

References

Abramson HN (1966). The dynamic behavior of liquids in moving containers. *NASA Special Publication*, SP-106.

Bauer HF (1964). Tables and graphs of zeros of cross-product Bessel functions. *Mathematics of Computation*, 18(85), 128.

Debbarma R, Chakraborty S, Ghosh SK (2010). Optimum design of tuned liquid column dampers under stochastic earthquake load considering uncertain bounded system parameters. *International journal of mechanical sciences,* 52(10), 1385-1393.

FEMA P-695 (2009). Quantification of Structure Seismic Performance Factors. Washington.

Gao H, Kwok KCS, Samali B (1997). Optimization of tuned liquid column dampers. *Engineering Structures,* 19(6), 476-486.

Hitchcock PA, Kwok KCS, Watkins RD, Samali B (1997). Characteristics of liquid column vibration absorbers (LCVA)–I. *Engineering Structures*, 19(2), 126-134.

Liu, M. Y., Chiang, W. L., Hwang, J. H., & Chu, C. R. (2008). Wind-induced vibration of a high-rise building with tuned mass damper including soil-structure interaction. *Journal of Wind Engineering and Industrial Aerodynamics*, 96(6-7), 1092-1102.

Matlab R2018a (2018). The MathWorks, Natick, MA.

Mehrkian B, Altay O (2020). Mathematical modeling and optimization scheme for omnidirectional tuned liquid column dampers. *Journal of Sound and Vibration,* 484, 115523.

Ocak A, Bekdaş G, Nigdeli SM, Kim S, Geem ZW (2022). Optimization of tuned liquid damper including different liquids for lateral displacement control of single and multi-story structures. *Buildings*, 12(3), 377.

Rana R and Soong TT (1998). Parametric study and simplified design of tuned mass dampers. *Engineering Sructures,* 20(3), 193-204.

Rouf AI (2005). Liquid Sloshing Dynamics: Theory and Applications, Cambridge University Press, ISBN: 0-521-83885-1.

Setareh M, Ritchey JK, Baxter AJ, Murray TM (2006). Pendulum-tuned mass dampers for floor vibration control. *Journal of Performance of Constructed Facilities*, 20(1), 64-73.

Shaban N, Caner A, Yakut A, Askan A, Karimzadeh Naghshineh A, Domanic A, Can G (2015). Vehicle effects on seismic response of a simple-span bridge during shake tests. *Earthquake Engineering & Structural Dynamics*, 44(6), 889-905.

Shah MU, Usman M, Farooq SH, Kim IH (2022). Effect of tuned spring on vibration control performance of modified liquid column ball damper. *Applied Sciences*, 12(1), 318.

Sharma V, Arun CO, Krishna IP (2019). Development and validation of a simple two degree of freedom model for predicting maximum fundamental sloshing mode wave height in a cylindrical tank. *Journal of Sound and Vibration*, 461, 114906.

Shum KM (2009). Closed-form optimal solution of a tuned liquid column damper for suppressing harmonic vibration of structures. *Engineering Structures*, 31(1), 84-92.

Singh MP, Singh S, Moreschi LM (2002). Tuned mass dampers for response control of torsional buildings. *Earthquake Engineering & Structural Dynamics*, 31(4), 749-769.

Sun LM, Fujino Y, Pacheco BM, Chaiseri P (1992). Modeling of tuned liquid damper (TLD). *Journal of Wind Engineering and Industrial Aerodynamics,* 43(1-3), 1883-1894.

Taflanidis AA, Angelides DC, Manos GC (2005). Optimal design and performance of liquid column mass dampers for rotational vibration control of structures under white noise excitation. *Engineering Structures,* 27(4), 524-534.

Tanveer M, Usman M, Khan IU, Farooq SH, Hanif A (2020). Material optimization of tuned liquid column ball damper (TLCBD) for the vibration control of multi-story structures using various liquid and ball densities. *Journal of Structure Engineering*, 32, 101742.

Venanzi I, Materazzi AL (2013). Robust optimization of a hybrid control system for wind-exposed tall buildings with uncertain mass distribution. *Smart Structures and Systems*, 12(6), 641-659.

Vickery BJ, Isyumov N, Davenport AG (1983). The role of damping, mass, and acceleration *Journal of Wind Engineering and Industrial Aerodynamics*, 11(1-3), 285-294.

Wibowo H, Sanford DM, Buckle IG, Sanders DH (2014). Preliminary parametric study of the effects of live load on seismic response of highway bridges. In *Proceedings of the 10th US National Conference on Earthquake Engineering. Earthquake Engineering Research Institute*.

Xing C, Wang H, Li A, Xu Y (2014). Study on wind-induced vibration control of a long-span cable-stayed bridge using TMD-type counterweight. *Journal of Bridge Engineering*, 19(1), 141-148.

Xue SD, Ko JM, Xu YL (2000). Optimum parameters of tuned liquid column damper for suppressing pitching vibration of an undamped structure. *Journal of Sound and Vibration*, 235(4), 639-653.

Yu JK, Wakahara T, Reed DA (1999). A non-linear numerical model of the tuned liquid damper. *Earthquake Engineering & Structural Dynamics,* 28(6), 671-686.

Challenge Journal of Structural Mechanics

Research Article

Statistical investigation of the effect of different damage conditions on the modal frequency value of a steel beam

Emre Alpaslan [a,*]

[a] *Department of Civil Engineering, Ondokuz Mayıs University, 55139, Samsun, Turkey*

ABSTRACT

This study aimed to parametrically investigate the changes in modal frequency values on a steel beam caused by specified damaged schemes. In this context, the ANSYS Workbench software program was used to create a steel profile's finite-element model. A cantilever steel beam profile is created with a 60x60 mm cross-section and 3m length utilizing single-sided fixed support. In the finite-element model, the crack depth, width, and distance to the support were parametrically assigned as the damaged scheme to the steel profile. To investigate the effects of those damages on the modal frequency values of the steel profile, first of all, the modal frequency values for undamaged cases corresponding to the first ten-mode shapes were obtained. Then, the specified crack properties were determined parametrically, and the changes in frequency values for damaged cases were examined. In addition, a comparative evaluation of the effect of crack properties on the natural frequency of the steel element was performed by utilizing response surface and six sigma analysis. The analysis results demonstrated that specified crack schemes have different effects on different modal natural frequencies. The applied response surface and six sigma analysis provided important statistical data on the modal natural frequency values of the steel beam.

ARTICLE INFO

Article history:
Received 27 April 2022
Revised 23 May 2022
Accepted 9 June 2022

Keywords:
Response surface
Six sigma analysis
Modal analysis
Finite-element model
Probability distribution

1. Introduction

The methods of assessing and detecting structural damage by examining the dynamic behavior of structures were started in 1980 when fast Fourier transforms could be made with software programs. In general, this method has been used in mechanical engineering, fuel industry companies, companies that build spaceships, and civil engineering. In this direction, many studies have been carried out by these groups on the early detection of damage to structures. Studies have revealed different approaches, test methods, and analysis techniques. It is not an effective and correct approach to use a single method in all situations that may exist in all types of buildings (Montalvao et al. 2006; Choi et al. 2005).

Significant progress has been made in the determination of damage effects in various subjects in mechanical engineering. The greatest success in damage assessment has been achieved by studies on marine structures by the fuel industry between 1970 and 1980. Although significant progress has been made in making damage assessments based on changes in dynamic behavior, the application of these techniques in real structures has been very difficult and limited. The spaceship building industry achieved significant success in dynamic-based damage assessment studies in the early 1980s.

In parallel with these, civil engineers started to use similar techniques in the early 80s. Health monitoring of buildings has been the primary field of study in bridge assessments and has quickly spread to other building types. In the literature, there are many applications of this method in beam structures (concrete and steel), truss systems, frames, shells, and plates, buildings, bridges, and composite materials (Gounaris and Dimarogonas 1988; Ostachowicz and Kraawczuk 1991; Srinivasan and Kot 1992; Mohammad 1997).

The basis of structural health monitoring is that regional damages in structures cause a stiffness reduction

* *Corresponding author*. Tel.: +90-362-312-1919 ; Fax: +90-362-457-6094 ; E-mail address: emre.alpaslan@omu.edu.tr (E. Alpaslan)
ISSN: 2149-8024 / DOI: https://doi.org/10.20528/cjsmec.2022.03.002

in the relevant region. In this respect, updating the stiffness parameters of the finite-element (FE) model by taking into account several different damage conditions provides full and accurate information about the current state of the structure. Rytter (1993) stated the following 4 steps in determining the damage that may occur in an existing structure; 1) Determination of damage to the structure, 2) Evaluating the damage location in the structural geometry, 3) Determining the extent and significance of the damage, 4) Estimating how much time the structure will have to serve. The first three steps of these include studies on estimating the presence, location, and magnitude of damage. Although the first three steps are important, the last step is the most fundamental section of structural health monitoring and is also the most difficult step in terms of implementation.

By using the parameters obtained from the modal analysis techniques that can be applied to the structures, the presence, location, and size of existing damage can be determined. This approach is based on the fact that structural damage affects the entire behavior of the structure (mass, stiffness, or damping) and thus changes the dynamic characteristics of the structure (natural frequency, damping ratio, and mode shape) (Doebling et al. 1998). Therefore, the dynamic properties of any structure that can be obtained periodically play an important role in determining the current state of the structures. Based on the change values in these dynamic parameters that will occur in undamaged and damaged structures, it is possible to estimate the region and size of the structural damage.

Mermertas and Erol (2001) investigated the effect of mass attachment on the transverse vibration characteristics of a cracked cantilever beam by relative changes of the first three natural frequencies. They resulted in the study that the decreasing effects of the cracked beam on natural frequencies were more apparent with added mass to the beam in different cases. Owolabi et al. (2003) investigated the effects of cracks and damages on structural integrity by using two sets of aluminum beams as fixed and simple supports. As a result, it was emphasized that the vibration behavior of beams is very sensitive according to the amount, depth, and region of cracks. Gillich et al. (2012) presented a method to detect, locate and evaluate the damage severity of Euler-Bernoulli beams, based on the changes in the natural frequencies due to damage. The accuracy and reliability of the proposed method were validated by numerous experiments.

Dey et al. (2016) stated that crack parameters were revealed to a significant extent in their study to establish the relationship between the input parameters (crack zone and crack depth ratio) and the output parameter (natural frequencies) to estimate the crack parameters, region and depth ratio. Yendhe et al. (2016) investigated beam vibration behavior both experimentally and with the help of the FEM program ANSYS. Vibration analysis is carried out on several cantilever beams with transverse cracks and various boundary conditions in the current study. Altunışık et al. (2017a) performed a comprehensive study on the automated model updating of a cantilever beam with box cross-section including multiple cracks for damage detection experimentally and numerically. Modal Assurance Criterion and Coordinate Modal Assurance Criterion factors were employed to recognize and locate damaged elements within the beam.

Multiple damage schemes with different ranges of magnitudes such as crack depth, crack width and crack distance to the support point emerge as important parameters for vibration analysis of beams. This vibration analysis is generally carried out by examining the change of natural frequency values on the beam depending on the size and position of the damages. In the performed studies, parametric analyzes were made for one or two different damage cases at critical points for the types of damage that may occur on beam-type structures (Altunışık et al. 2017b). It is also important to investigate the effect of different crack types at different positions on natural frequency values at all points along the beam to ensure the safety and performance of beam-type structural elements. The scope of this study is aimed to investigate the relationships between input and output variables with a probabilistic approach, taking into account the uncertainty of various damages that may occur in structures. In this context, various crack schemes were chosen as random input variables and the effects of a steel beam on the modal natural frequency were evaluated using the response surface (RS) method and six sigma (SS) analysis. The FE model of the steel beam was created by ANSYS Workbench and modal parameters were obtained for the undamaged case. Then, the crack depth, width, and distance from the support point were defined as variable input parameters, and statistical analysis was performed by comparing the modal natural frequency values obtained for damaged cases with those values calculated in the undamaged condition. As a result of the analysis, valuable results were achieved to better understand the effects of damage schemes on the natural modal frequency values depending on the obtained mode shapes.

2. Methodology

2.1. Overview

In this study, the ANSYS DesignXplorer (ANSYS 2013) platform was utilized for the FE model of the steel profile and the SS Analysis for parametric studies to understand the effects of the damage cases on the modal behavior of the selected structure. The SS analysis system consists of a Design of Experiments (DoE) cell, an RS cell, and an SS analyses cell. The DoE cell allows to set up of the input parameters, which SS analyses refer to as uncertainty parameters, and generates the samples for the analysis. RS method is an approximate optimization method that seeks multiple design variables and their responses by employing the minimum number of design samples for the best experimental design, to determine the combination of design variables. It can be accomplished a good accuracy between the FE model-generated data and the experimental data by utilizing the RS method (Cheng et al. 2007; Landman et al. 2007).

2.2. Design of experiments

The design of experiments is a method for determining the location of sample points scientifically. In engineering research, there are several different designs of experiments algorithms or procedures, including star, complete factorial, central composite, and Box-Behnken designs. All of the strategies have one thing in common: they all strive to locate sampling points in the space of random input parameters in the most efficient way or with the fewest sample points possible to get the information they need. Sample points in effective locations not only lower the number of sampling points necessary but also improve the accuracy of the RS calculated from the sampling points' findings. Guo and Zhang (2004) revealed in their study that the central composite design and the D-optimal design give approximately the same results in the RS-based FE update approach. In addition, the efficiency of central composite design, Box-Behnken design, and D-optimal design for damage assessment of structures was evaluated by Umar et al. (2018) and it was stated that the central composite design is more effective in damage detection. The central composite design was chosen as a sampling strategy for three variables in this investigation.

There are different distribution types for input parameters in the DoE namely Triangular, Uniform Normal, Lognormal, Exponential Truncated, Weibull, and Beta. The goal of this study was to employ the Gaussian (Normal) Distribution, which is a fundamental and widely used statistical distribution. It's a term that's frequently used to describe the distribution of measurement data for a wide range of physical phenomena. If the random variable is a linear mixture of two or more other effects, and those effects also follow a Gaussian distribution, the Gaussian distribution is valid. The mean value and standard deviation of the random variable can be provided as input values (ANSYS 2013).

2.3. Response surface method

The genetic aggregation technique was employed to create RS models in this work. The method automates the process of selecting, configuring, and creating the RS. Due to various RS solutions and cross-validation methods, it automatically develops the most appropriate approach for each output and gives more dependable results than previous RS models. After their fitness has been evaluated, the fitted RS models should be utilized to update the FE model. For multi-RSM and sophisticated models, the R2 criterion and the root mean squared error (RMSE) criterion are commonly used (Box and Draper 1987; Fang and Perera 2009). The R-square statistic and the relative mean square error are presented in Eqs. (1) and (2), respectively, are used to assess the accuracy of fitted RS models.

$$R^2 = 1 - \frac{\sum_{j=1}^{N}[y_{RS}(j)-y(j)]^2}{\sum_{j=1}^{N}[y(j)-\bar{y}]^2} \tag{1}$$

$$RMSE = \frac{1}{N*\bar{y}}\sqrt{\sum[y_{RS}(j)-y(j)]^2} \tag{2}$$

The larger the value of R Square is, the more accurate the RS model is. The smaller the value of RSME is, the more accurate the RS model is.

2.4. Six sigma analysis

A technique known as SS analysis is used to assess the impact of unclear input parameters and assumptions on a model. It may be evaluated how much the model's uncertainties affect the analysis outcomes using an SS analyses system. Uncertainty (random quantity) is a parameter whose value is impossible to predict at a specific time or location (if it is time-dependent) (if it is location-dependent). The fundamental goal of an SS analysis is to determine the impact of uncertainties associated with the design's input parameter. Various statistical studies and post-processing analyses are used to attain this goal (ANSYS 2013).

2.4.1. Mean value

The average of a group of observations is measured by the mean. The following is the definition of the mean of a set of observations;

$$\hat{\mu} = \frac{1}{n}\sum_{i=1}^{n} y_i \tag{3}$$

2.4.2. Standard deviation

The standard deviation is a measure of how far a group of data deviates from the mean. The following is how a set of observations' standard deviation is calculated;

$$\hat{\sigma} = \sqrt{\frac{1}{(n-1)}\sum_{i=1}^{n}(y_i-\hat{\mu})^2} \tag{4}$$

2.4.3. Sigma level

The inverse cumulative distribution function of a conventional Gaussian distribution in a particular percentile is used to compute the sigma level. To measure the data distribution from the mean, the sigma level is employed in conjunction with the standard deviation.

2.4.4. Skewness

The degree of asymmetry around the mean for a group of observations is measured by skewness. The observations are symmetrical if the distribution of the observations looks the same to the left and right of the mean. Negative skewness denotes a left-skewed distribution of observations. Positive skewness denotes a right-skewed distribution of observations. A collection of observations' skewness is defined as follows;

$$\hat{\gamma} = \frac{n}{(n-1)(n-2)}\sum_{i=1}^{n}\left(\frac{y_i-\hat{\mu}}{\hat{\sigma}}\right)^3 \tag{5}$$

2.4.5. Kurtosis

For a set of observations, kurtosis is a measure of the distribution's relative peak/flatness. When compared to the normal distribution, it's usually a relative comparison. The normal distribution is generally used as a reference point. As shown in Fig. 1, negative kurtosis indicates that the distribution of data is comparatively flat when compared to the normal distribution, whereas positive kurtosis indicates that the observations peaked substantially. As a result, calibration concerning the normal distribution defines the kurtosis of a set of observations as follows;

$$\hat{\kappa} = \left\{\frac{n(n+1)}{(n-1)(n-2)(-3)}\sum_{i=1}^{n}\left(\frac{y_i-\hat{\mu}}{\hat{\sigma}}\right)^4\right\} - \frac{3(n-1)^2}{(n-2)(n-3)} \quad (6)$$

where $\hat{\sigma}$ and $\hat{\mu}$ represent mean and standard deviation, respectively.

2.4.6. Shannon entropy

The term "entropy" was first used in classical thermodynamics. It is a measure of a system's dysfunction. Later, in the realm of information/communication, Claude Shannon extended and adopted the concept of entropy as a measure of uncertainty over the actual content of a message. Entropy is recast as a function of mass density in statistics as follows;

$$H = -\sum P_i ln P_i \quad (7)$$

where P_i represents mass density of a parameter. Entropy is a measure of a parameter's complexity and predictability in the context of statistics and probability. Entropy increases as a parameter becomes more complex and unpredictable, and vice versa.

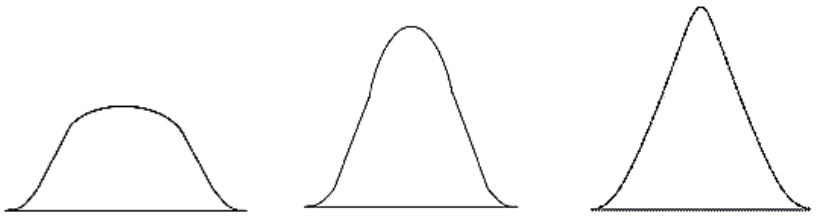

Fig. 1. Different types of kurtosis.

3. Application and Results

This study aimed to parametrically investigate the changes in modal frequency values on a steel profile caused by specified damaged schemes. For this, the ANSYS Workbench software program was performed to create a steel profile's FE model. The steel profile is modeled as a cantilever beam with a 60·60 mm cross-section as represented in Fig. 2 and 3m length utilizing single-sided fixed support. The material properties of the steel profile are E=2·10^{11} N/m^2, ρ= 7850 kg/m^3, and ν=0.3.

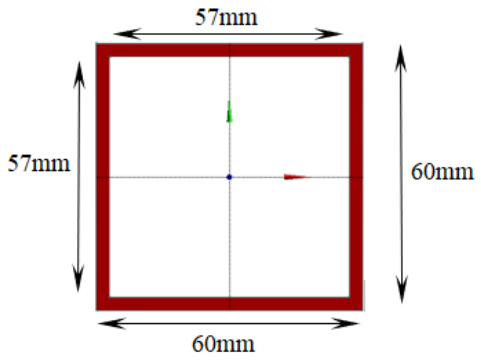

Fig. 2. Cross-section of the steel profile.

3.1. Finite element model

A 3D dimensional FE model of the steel profile as demonstrated in Fig. 3(a) has been created by using the ANSYS Workbench software program to obtain the dynamic characteristics such as natural frequency and mode shapes numerically. The FE model of the steel beam is assumed homogenous and isotropic elastic material. Since the effect of the mesh size of the structure on the calculated modal natural frequency values is important in modal analysis, the mesh convergence study is carried out to establish a satisfactory mesh size in this study. The initial mesh length was chosen as 0.5 m. The mesh size was reduced to such an amount that the corresponding mode shapes did not cause a significant change in the natural frequency values, and thus, the appropriate mesh size for the steel beam model was determined as 0.02m mesh size. The obtained modal natural frequency values of the undamaged steel beam are considered to compare the modal analysis results for damaged cases. In the FE model, the crack depth, width, and distance to the support were parametrically assigned as the damaged scheme to the steel profile as presented in Fig. 3(b). To investigate the effects of those effects on the modal frequency values of the steel profile, first of all, the modal frequency values for undamaged cases corresponding to the first ten-mode shapes were obtained as shown in Fig. 4. The first ten natural frequencies are calculated between 7.31 and 397.83 Hz for the undamaged beam. Also, the mode shapes of the steel beam appear as a bending mode in the x and y direction in all modes except the seventh mode which shows torsional modal behavior. The obtained undamaged case natural frequency values corresponding to ten-mode shapes are presented in Table 1. Also, the specified crack properties were determined parametrically, and the changes in frequency values for damaged cases were examined.

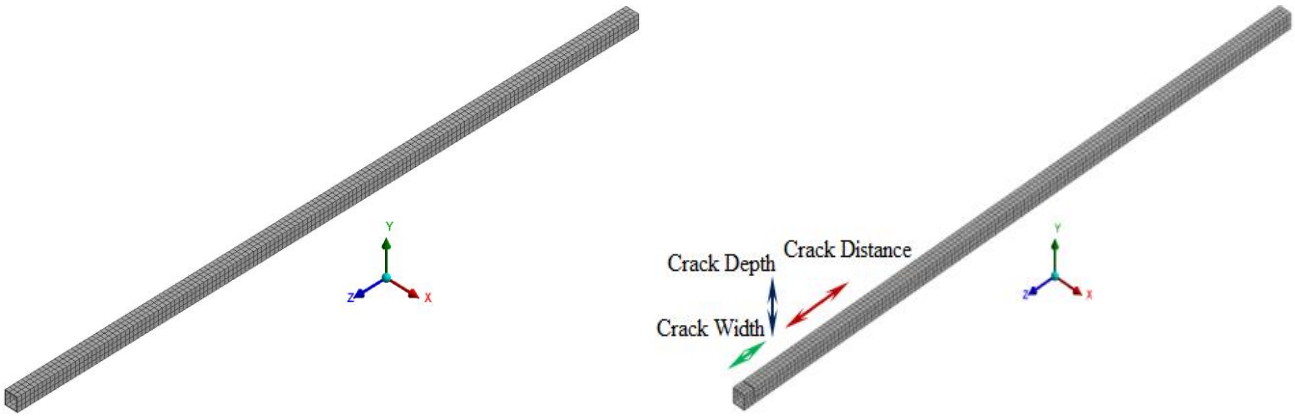

(a) (b)

Fig. 3. FE model of the steel profile: (a) Undamaged; and (b) damaged case.

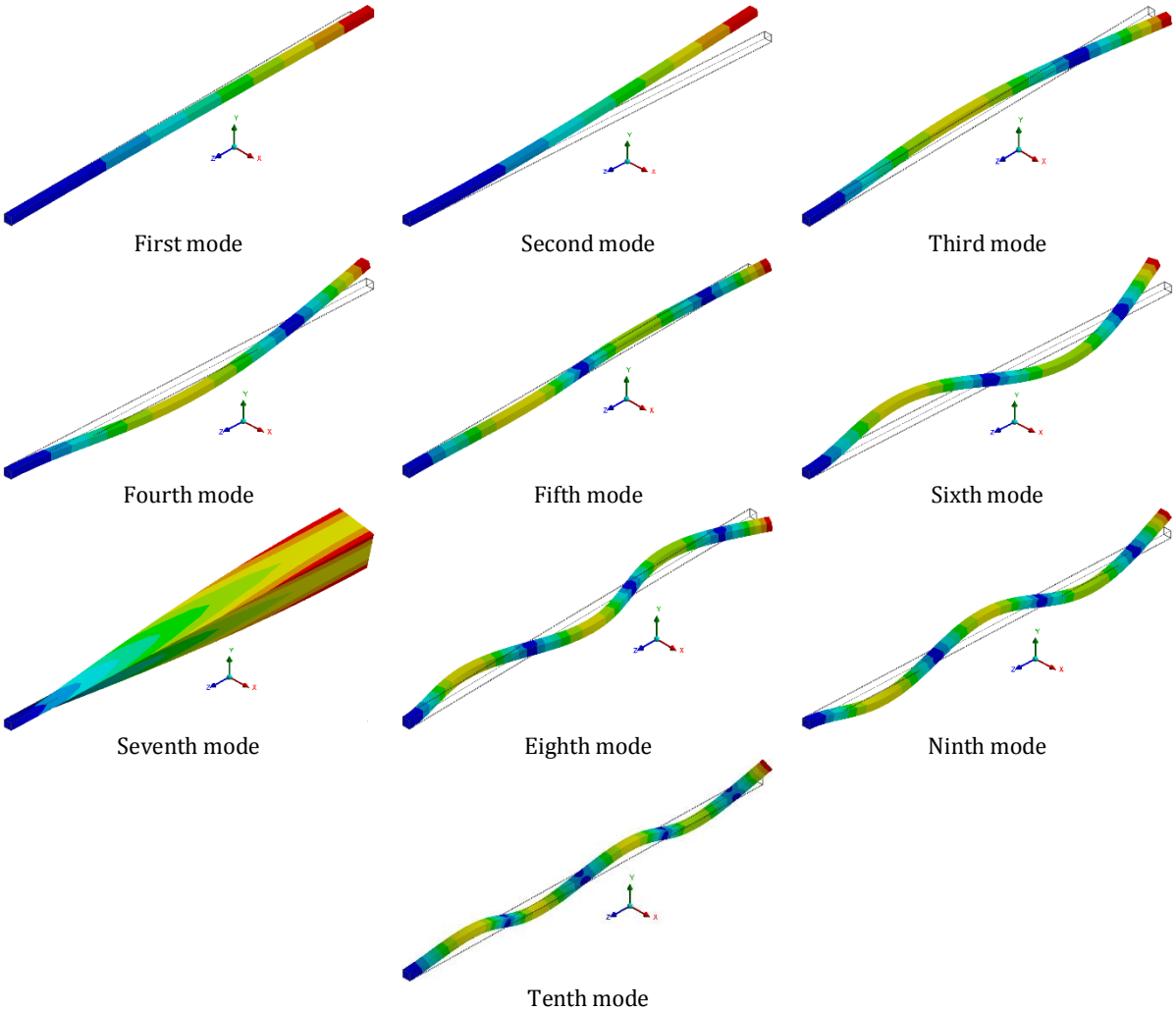

Fig. 4. Mode shapes of the steel beam.

Table 1. Undamaged beam modal frequencies.

Mode number	1	2	3	4	5	6	7	8	9	10
Frequencies (Hz)	7.31	7.31	45.56	45.56	126.45	126.45	229.93	244.64	244.64	397.83

3.2. Creating design of experiments

To achieve satisfactory design space for a good representation of an underlying physical problem and not able to miss capturing an unexpected change in some regions of the design space, an enhanced Face-Centered design type was used (Wagner et al. 2014). For an enhanced design of the experiment, to be able to catch any drastic changes in the design space, a mini-CCD is added to a standard CCD design, where a second alpha value is added and arranged to half the alpha value of the standard CCD. Therefore, in this study, the central composite design is selected as a sampling method (Ren and Chen 2010).

The lower and upper limits of the damage scenario including crack depth, width, and distance, as input parameters of the steel beam model for experimental design, are shown in Table 2. In the experimental design, a total of 29 design points (one center point, 2x ($2 \cdot 3$=6 axis point, and 2^3=8 (factorial points)) were evaluated using the enhanced face-centered central composite design approach at these upper and lower limits of the input parameters. The natural frequency values of the corresponding ten-mode shapes were selected as output parameters. In the experimental design calculated min frequency values depending on the upper and lower limits of input varying parameters are represented in Table 2.

Table 2. Upper and lower limits of input parameters and obtained corresponding min natural frequency values.

Input parameters	Parameter name	Lower upper limit (mm)	Mean/standard deviation
P1	Crack depth	1-40	20.5/6.31
P2	Crack width	1-20	10.5/3.075
P3	Crack distance	50-2950	1500/469.22
Output parameters		Min (Hz)	
P5	Mode 1	4.02	
P6	Mode 2	6.58	
P7	Mode 3	33.66	
P8	Mode 4	42.25	
P9	Mode 5	102.30	
P10	Mode 6	117.82	
P11	Mode 7	159.00	
P12	Mode 8	200.68	
P13	Mode 9	231.05	
P14	Mode 10	360.83	

3.3. Generating response surfaces

The RS models are created using a genetic aggregation approach. The R2 and RMSE metrics are used to assess the correctness of the RS models. Table 3 shows the R2 and RMSE values obtained for each related mode. It is generally shown that R2 and RMSE values are close to one and zero, respectively, which means that the RS models obtained have a high regression accuracy. Although minor deviations in RMSE values occur only in the seventh and tenth modal frequency values as marked in Fig. 5(a) the relevant values are still within an acceptable range.

Another indicator that shows the accuracy of the generated RS is the predicted-observed graph. This graph demonstrates the predicted values from the RS and the observed values from the design points. This provides a quick understanding of the compatibility of the RS to the experimental design points. The closer the points are to the diagonal line, the more the RS is aligned with the points. Otherwise, it cannot adequately capture the parametric behavior of the RS. Therefore, it is necessary to reconstruct the RS. Fig. 5(a) shows the predicted-observed graph created at this point. All output parameters and output values are normalized in the graph. As can be seen, the values on the RS are in good agreement with the values at the experimental design points.

Table 3: Accuracy check for response surfaces.

Modes	1	2	3	4	5	6	7	8	9	10
R2	1	0.99	1	0.99	1	0.99	0.92	0.99	0.99	0.98
RMSE	4.3E-7	0.013	1.9E-5	0.027	8.2E-6	0.081	5.57	0.46	0.18	1.35

The local sensitivity plots of RS models according to the average value of the input parameters as a response point are shown in Fig. 5(b). In general, crack width seems to have the lowest effect compared to the other two damage conditions, considering all-natural frequency values. The effects of crack depth and distance on natural frequency values vary in each mode. It is observed that the crack distance has the most important effect on the first, second, fifth, and sixth modal natural frequency values, while the crack depth has the most influence on the natural frequency values for the other mode shapes. It can also be seen that there is no significant effect on the fifth and sixth natural frequency values in the case of crack depth compared to those in other modal natural frequency values. The local sensitivity of the crack depth ranges from approximately 3% to 90%, with the greatest sensitivity occurring in the eighth mode shapes. On the other hand, the local sensitivity range of the crack distance is not as variable as the crack depth and it seems to be between 20 and 45%. The mode in which the crack distance is most effective corresponds to the seventh mode which is the torsional mode.

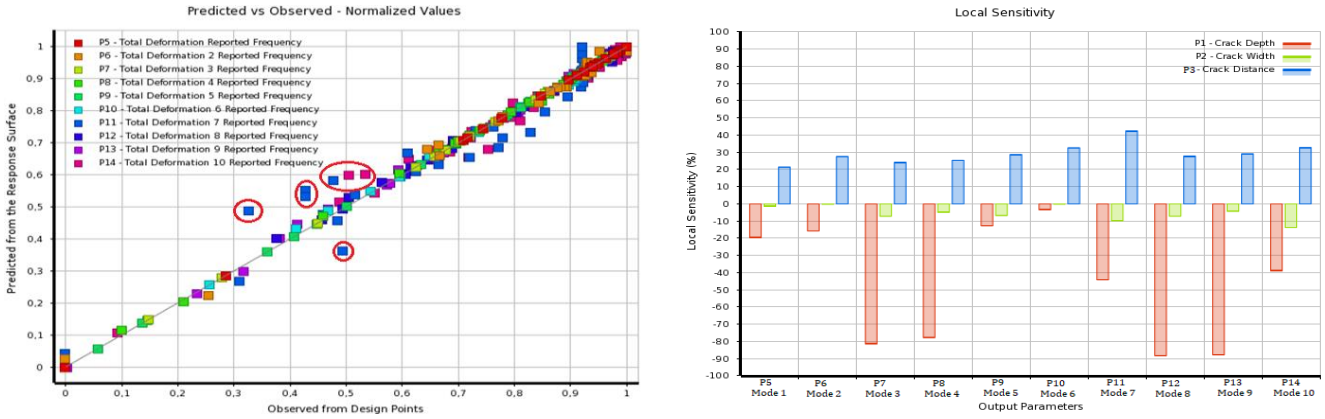

(a) (b)

Fig. 5. (a) Predicted vs. observed points; (b) Sensitivity analysis of input-output parameters.

In the result of the RS analysis, another significant view to understanding the effects of damage scenarios on the steel beam is the min search matrix of output parameters as depicted in Table 4. The importance of the min search matrix of the output parameters is valuable in terms of determining the convergence and divergence of the min modal natural frequency values in the lower and upper limit values given in damage scenarios.

The min values for all modal natural frequencies occur when the crack depth converges to the upper limit value. Also, in general, crack width shows the same behavior as crack depth, just the last two natural frequencies are close to the upper limit values. On the other hand, the min values of the first, second, fourth, sixth, seventh, and tenth modal natural frequencies are revealed when the crack distance converges to the lower limit value. Furthermore, in third, eighth, and ninth mode shapes, natural frequencies converge towards the mean value of lower and upper limit values in the crack distance.

Table 4. Min search of output parameters.

	Input parameters (mm)			Output parameters (Hz)								
Name	P1	P2	P3	P5	P6	P7	P8	P9	P10	P11	P12	P13	P14
Output parameter minimums													
P5 - Mode 1	40.00	20.00	50.00	4.02	6.58	35.87	42.25	109.67	117.82	159.00	222.02	234.56	360.85
P6 - Mode 2	40.00	20.00	50.00	4.02	6.58	35.87	42.25	109.67	117.82	159.00	222.02	234.56	360.85
P7 - Mode 3	40.00	20.00	1499.36	6.32	7.17	33.66	42.62	122.01	125.96	187.61	200.68	231.22	377.97
P8 - Mode 4	40.00	20.00	50.00	4.02	6.58	35.87	42.25	109.67	117.82	159.00	222.02	234.56	360.85
P9 - Mode 5	40.00	20.00	2224.63	6.96	7.28	40.41	44.37	102.30	119.83	206.53	217.23	235.80	381.68
P10 - Mode 6	40.00	20.00	50.00	4.02	6.58	35.87	42.25	109.67	117.82	159.00	222.02	234.56	360.85
P11 - Mode 7	40.00	20.00	50.00	4.02	6.58	35.87	42.25	109.67	117.82	159.00	222.02	234.56	360.85
P12 - Mode 8	40.00	20.00	1498.31	6.32	7.17	33.66	42.62	122.01	125.96	187.58	200.68	231.22	377.97
P13 - Mode 9	40.00	15.15	1497.28	6.52	7.18	33.84	42.61	122.46	126.05	191.92	201.09	231.05	378.82
P14 - Mode 10	40.00	18.73	50.00	4.11	6.59	35.94	42.28	109.72	117.96	160.49	222.06	234.57	360.83

The last investigation in this section is to present the created RS that allows understanding the effect of each input parameter on the output parameters. Each damage scenario is examined for all ten modal natural frequency values corresponding to mode shapes as illustrated in Fig. 6.

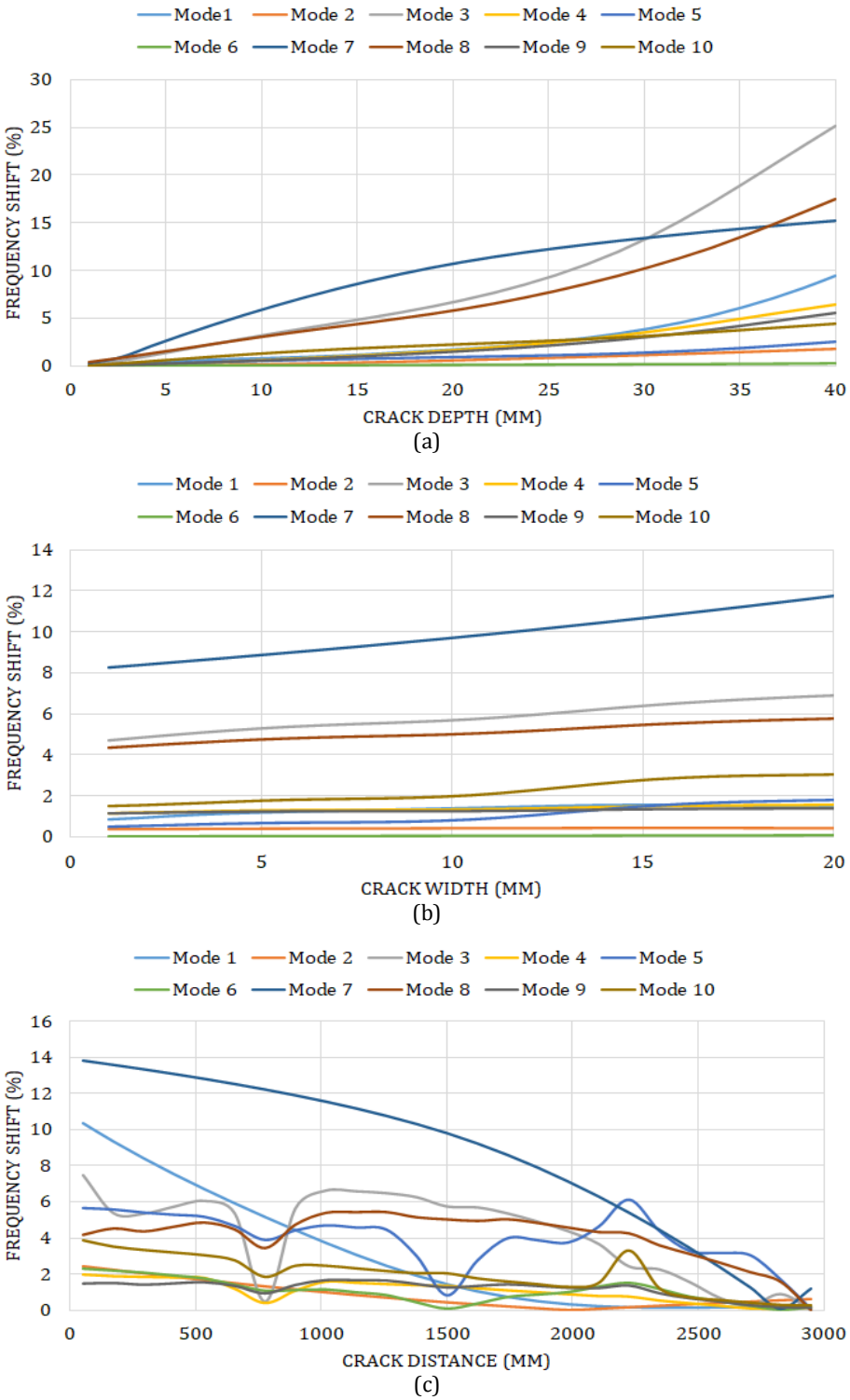

Fig. 6. Obtained response surfaces of input-output parameters: (a) Crack depth; (b) Crack width; (c) Crack distance.

The increase in crack depth and crack width causes an increase in the all-modal natural frequency values of the steel beam model. The frequency changes for corresponding modes caused by the crack depth and width vary between about 0.25%-25% and 0.02%-3.5%, respectively, depending on the lower and upper limits. In the case of crack depth, the max shift in natural frequency occurs in the third mode with an approximate increase of 25%, and the modal frequency values in torsional mode 7 follow it with a raise of about 15%, while the results show that percentage of increase in modal natural frequency is the minimum at mod 6 with a value

of 0.25%. When the percentage increase of crack width on the modal frequency values is examined, it is observed that the lowest percentage increases are 0.015% in the sixth mode and 0.02% in the second mode. On the other hand, it turns out that the highest percentage increase is approximately 4% in the torsional mode, which is the seventh mode shape. In addition, when the crack width is analyzed as percentage increase values, it is revealed that it increases less than other crack parameters. Finally, for the crack distance, it is observed that the modal natural frequency increase values vary in the range of approximately 1.4%-10% in the corresponding mode shapes. It is seen that the percentage increase of the crack distance decreases as it moves away from the support area. The highest percentage increase is observed at the first natural frequency, and the lowest percentage increase is at the ninth natural frequency.

3.4. Six sigma analysis

The Latin Hypercube Sampling (LHS) approach is used by default in the ANSYS Workbench platform for SS assessments. With LHS, points are created at random over the design space in a square grid, but no two points have the same value input parameters. This means that no point in the grid shares a row or column with another point.

The statistical features described in previous sections of the input and output parameters are depicted in Tables 5 and 6, respectively. Although the standard deviations of the lower and upper limit values seem to be a little bit higher amount, especially in the crack distance due to a better understanding of the effects of cracks schemes in the input parameters, the standard deviation values obtained in the output parameters were not that high. Considering the numerical magnitudes of the modal frequency values obtained from the modal analysis, it can be said that the standard deviation values obtained in the output parameters are suitable for statistical analysis. This can be also said for the sigma level and skewness which shows enough convergence of both input and output parameters. In the kurtosis of input and output parameters, all of the input parameters demonstrate normal distributions, whereas all of the output parameters illustrate peak distribution except the seventh and tenth modes which are close to normal distribution. Finally, The Shannon entropy which presents a measure of the complexity and predictability of input and output parameters is calculated as enough small amount that demonstrates less complex, and more predictable distributions of the corresponding parameters.

Also, probability density function histograms and cumulative density functions of the random variable distribution after 10,000 simulations of the 3 input and 10 output parameters are represented in Figs. 7 and 8, respectively. The histogram of random variable sample distribution can describe the distribution of random variables. As it can be seen from the probability density distributions of the parameters, the input and output parameter distribution curves are smooth and without any gaps, presenting that enough input simulations are converging the statistical requirements.

Table 5. Description of input parameters.

Properties	Crack depth	Crack width	Crack distance
Mean	20.50	10.50	1500
Standard deviation	6.31	3.07	469.41
Skewness	-5.71E-04	4.22E-04	1.59E-03
Kurtosis	-3.54E-03	-2.15E-03	1.93E-02
Shannon entropy	3.26	2.54	7.57
Sigma minimum	-3.81	-3.81	-3.81
Sigma maximum	3.81	3.81	3.81

Table 6. Description of output parameters.

Modes	1	2	3	4	5	6	7	8	9	10
Mean	7.12	7.26	42.64	44.89	121.12	125.20	206.67	230.66	240.54	388.80
Standard deviation	0.20	0.05	1.33	0.34	2.26	0.87	8.18	4.63	1.56	3.59
Skewness	-2.12	-1.32	-0.42	-0.95	-0.65	-0.97	0.18	-0.50	-0.51	-0.10
Kurtosis	7.72	3.75	1.43	2.38	2.34	1.33	0.28	1.52	1.51	0.27
Shannon entropy	-0.48	-1.68	1.69	0.28	2.17	1.16	3.51	2.94	1.84	2.70
Sigma minimum	-3.81	-3.81	-3.81	-3.81	-3.81	-3.81	-3.81	-3.81	-3.81	-3.81
Sigma maximum	3.81	3.81	3.81	3.81	3.81	3.81	3.81	3.81	3.81	3.81

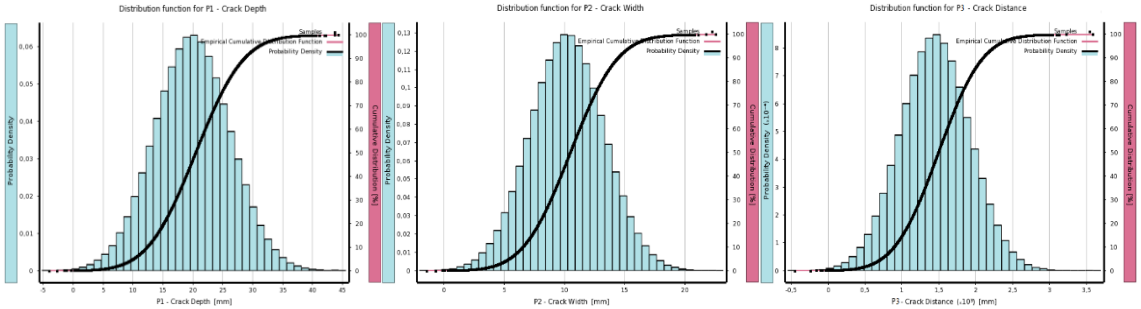

(a) (b) (c)

Fig. 7. Probability density of parameters: (a) Crack depth, P1; (b) Crack width, P2; (c) Crack distance, P3.

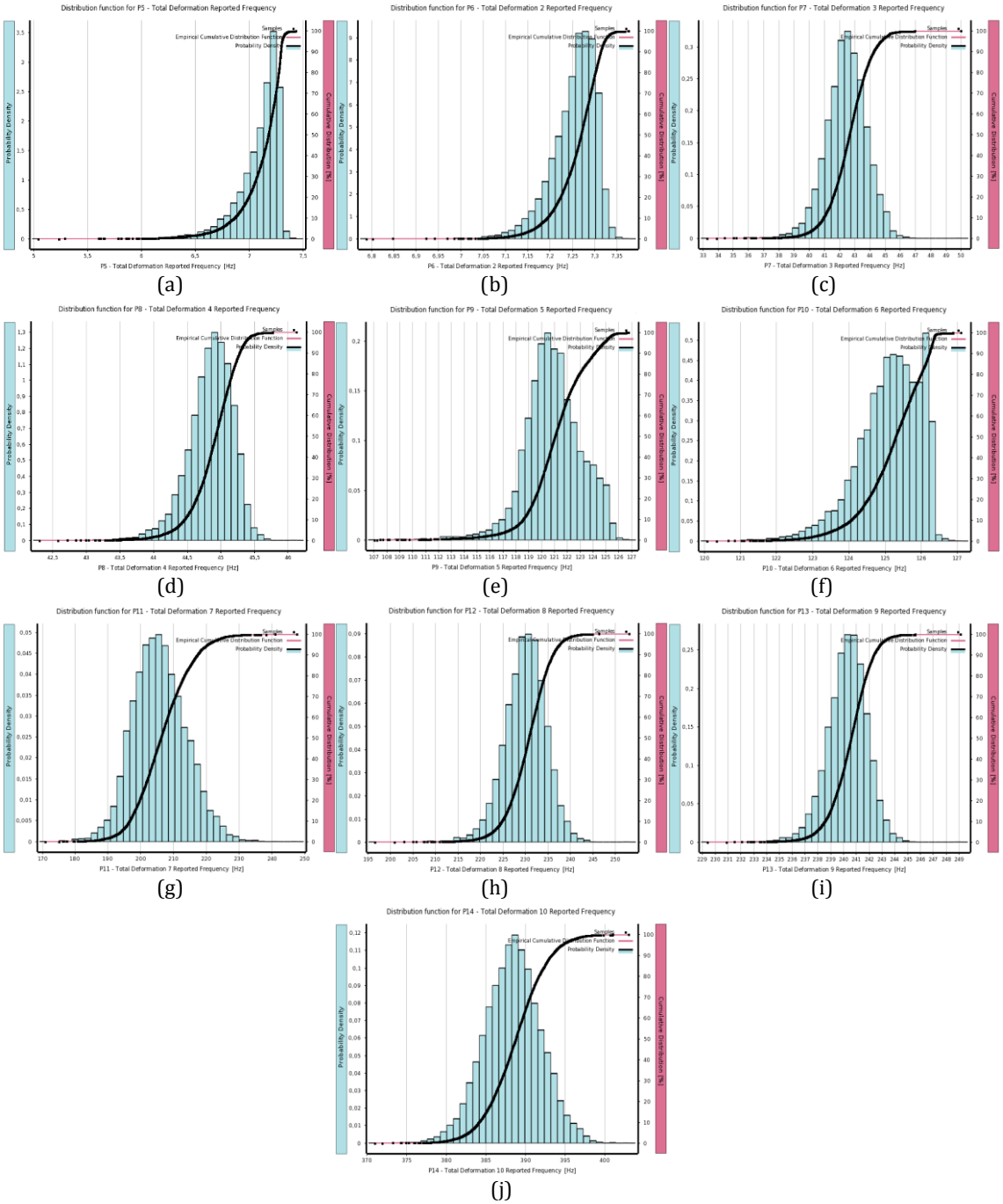

(d) (e) (f)

(g) (h) (i)

(j)

Fig. 8. Probability density of parameters: (a) Mode 1, P5; (b) Mode 2, P6; (c) Mode 3, P7;(d) Mode 4, P8; (e) Mode 5, P9; (f) Mode 6, P10; (g) Mode 7, P11; (h) Mode 8, P12; (i) Mode 9, P13; (j) Mode 10, P14.

A cumulative distribution function plot is a useful tool for calculating the probability that a project's design meets or fails to meet reliability standards, as well as assessing the project's reliability and failure probability. Reliability is defined as the probability that no failure occurs. The probability that an output parameter will remain below a given level as shown by the values on the X-axis of the plot is represented by the value of a cumulative distribution function of that output parameter. In the context of this study, the eigenfrequencies can be chosen to be above a specific permissible limit, and if an eigenfrequency falls below this limit, a failure event happens. As a result, the cumulative distribution function is understood as the steel beam's failure probability curve.

It can be seen from Fig. 8 that the distributions for first, second, fourth, and sixth modal natural frequency values increase as those get closer to the natural frequency value obtained in the undamaged condition. It is observed that the natural frequency values of the third, fifth, seventh, eighth, ninth, and tenth mode shapes are concentrated at about 7, 5, 10, 6, 2, and 3% of undamaged modal natural frequency values, respectively.

4. Conclusions

This study aimed to examine the effect of damage schemes specified on the steel beam model on the modal frequency value of the steel beam, by using the natural frequency values representing the undamaged state obtained by creating a FE model of a box section steel profile modeled as a fixed beam. For damage schemes, crack depth, width, and distance from the support point were selected and were defined as the input variable parameters. The effects of the generated crack schemes on the modal natural frequencies of the steel beam were investigated statistically with the help of RS and SS analyses. The following conclusions can be drawn from the present study;

- The first ten modal natural frequency values were evaluated between 7.31 Hz and 397.83 Hz for the undamaged steel beam model. For the damage cases in the steel beam, the max decrease in those frequency values for the corresponding mode shapes was calculated as 4 Hz and 360.8 Hz.
- Considering the three damage conditions, crack width seems to be the least sensitive effect on the natural frequency change corresponding to all mode shapes when compared with crack depth and distance.
- Crack depth has the most influence on first, second, fifth, sixth, and tenth bending modes and torsion modes, whereas, the crack distance presents the most sensitive behavior in third, fourth, eighth, and ninth mode shapes.
- The max decrease in modal natural frequency values is approximately 25, 3.5, and 10% for crack depth, width, and distance, respectively compared to those with undamaged cases in the steel beam.
- SS analyses demonstrate that there is enough convergence of both input and output parameters from the statistical analysis point of view and less complex, and more predictable distributions are achieved.
- The first, second, fourth, and sixth modal natural frequency distributions obtained in the damaged condition converge to the frequency values calculated by the natural frequency values in the undamaged condition. The natural frequency values of the other mode shapes are concentrated in approximately 7, 5, 10, 6, 2, and 3% of the frequency values obtained in the undamaged condition, respectively.

The fundamental of structural health monitoring is that the damage in the structures will cause a general decrease in stiffness, which will cause a change in the general dynamic behavior of the structures. This decrease in stiffness causes a decrease in the modal frequency values of the structure. As a result of the analyses performed in this study, the fact that the damages to the steel beam model caused a significant decrease in the modal frequency values of the structure shows parallelism with this issue. The employed analysis will enable which type of damage plays a more critical role in the modal natural frequency values of the structure, thus determining the resonance frequency values of the structure and taking the necessary precautions beforehand. In addition, in cases where existing damage to the structure is known, the progression of the damage will provide statistically significant data on the modal behavior of the structure.

Acknowledgements

None declared.

Funding

The author received no financial support for the research, authorship, and/or publication of this manuscript.

Conflict of Interest

The author declared no potential conflicts of interest with respect to the research, authorship, and/or publication of this manuscript.

References

Altunışık AC, Okur FY, Kahya V (2017a). Automated model updating of multiple cracked cantilever beams for damage detection. *Journal of Constructional Steel Research*, 138, 499-512.

Altunışık AC, Okur FY, Kahya V (2017b). Modal parameter identification and vibration-based damage detection of a multiple cracked cantilever beam. *Engineering Failure Analysis*, 79, 154-170.

ANSYS (2013). Swanson Analysis System. Canonsburg, Pennsylvania.

Box GEP, Draper NR (1987). Empirical model-building and response surfaces. John Wiley and Sons, Inc., New York.

Cheng J, Zhang J, Cai CS, Xiao RC (2007). A new approach for solving inverse reliability problems with implicit response functions. *Engineering Structures*, 29(1), 71-79.

Choi S, Park S, Stubbs N (2005). Non-destructive damage detection in structures using changes in compliance. *International Journal of Soils and Structures*, 42(15), 4494-4513.

Dey P, Talukdar S, Bordoloi DJ (2016). Multiple-crack identification in a channel section steel beam using a combined response surface methodology and genetic algorithm. *Structural Control Health Monitoring*, 23(6), 938-959.

Doebling SW, Farrar CR, Prime MB (1998). A summary review of vibration-based damage identification methods. *The Shock and Vibration Digest*, 30(2), 91-105.

Fang SE, Perera R (2009). A response surface methodology-based damage identification technique. *Smart Material and Structures*, 18(6), 065009.

Gillich GR, Praisach ZI, Iavornic CM (2012). Reliable method to detect and assess damages in beams based on frequency changes. *Proceedings of the ASME International Design Engineering Technical Conferences and Computers and Information in Engineering Conference*, New York, USA, 129-137.

Gounaris G, Dimarogonas A (1988). A finite element of a cracked prismatic beam for structural analysis. *Computer and Structures*, 28(3), 309-313.

Guo QT and Zhang LM (2004), Finite element model updating based on response surface methodology. *Proceedings of the 22nd International Modal Analysis Conference (IMAC)*, Dearborn, USA, 306-309.

Landman D, Simpson J, Vicroy D, Parker P (2007). Response surface methods for efficient complex aircraft configuration aerodynamic characterization. *Journal of Aircraft*, 44(4), 1189-1195.

Mermertas V, Erol H (2001). Effect of mass attachment in the free vibration of cracked beam. *Proceedings of the 8th International congress on Sound and Vibration*, Hong Kong, China, 2803-2810.

Mohammad HD (1997). A comprehensive crack identification algorithm for beams under different end conditions. *Applied Acoustics*, 51(4), 381-398.

Montalvao D, Maia NMM, Riberio AMR (2006). A review of vibration-based structural health monitoring with special emphasis on composite materials. *The Shock and Vibration Digest*, 38(4), 295-324.

Ostachowicz WM, Kraawczuk M (1991). Analysis of the effect of cracks on the natural frequencies of a cantilever beam. *Journal of Sound and Vibration*, 150(2), 191-201.

Owolabi GM, Swamidas ASJ, Seshadri R (2003). Crack detection in beams using changes in frequencies and amplitudes of frequency response functions. *Journal of Sound and Vibration*, 265(1), 1-22.

Ren WX, Chen HB (2010). Finite element model updating in structural dynamics by using the response surface method. *Engineering Strucures*, 32(8), 2455–2465.

Rytter A (1993). Vibrational Based Inspection of Civil Engineering Structures. *PhD thesis*, Aalborg University, Aalborg, Denmark.

Srinivasan, MG Kot CA (1992). Effect of damage on the modal parameters of a cylindrical shell (No. ANL/CP-74111; CONF-920234-3). Argonne National Lab., IL, USA.

Umar S, Bakharya N, Abidin ARZ (2018), Response surface methodology for damage detection using frequency and mode shape. *Measurement*, 115, 258-268.

Wagner JR, Mount III EM, Giles HF (2014). Shear Rate, Pressure Drop, and Other Extruder Calculations. *William A editor.* In *Extrusion: The Definitive Processing Guide and Handbook, 2nd Edition*, USA, 203-206.

Yendhe VS, Kadlag PVL, Shelke PRS (2016). Vibration analysis of cracked cantilever beam for varying crack size and location. *International Research Journal of Engineering and Technology*, 3(8), 1913-1919.

Challenge Journal of Structural Mechanics

Research Article

Buckling resistance of the cylindrical shells with two secondary stiffening rings under external pressure

Özer Zeybek [a,*], Yasin Onuralp Özkılıç [b]

[a] *Department of Civil Engineering, Muğla Sıtkı Koçman University, 48000 Muğla, Turkey*
[b] *Department of Civil Engineering, Necmettin Erbakan University, 42090 Konya, Turkey*

ABSTRACT

The common way to amplify strength and stiffness of the tank wall is to use the stiffening rings. These stiffening rings can be classified as the primary and secondary stiffening rings (PSRs and SSRs). PSR is placed around the top of the tank shell and it assists to avoid ovalization at the top when the open-top tank is exposed to the external pressure. PSR having small dimensions may be used for fixed roof tanks since the roof system attached to the top of the cylindrical shell provides a natural restraint at this location. On the other hand, one or more SSRs may be required to preclude local buckling in both fixed and open-top cylindrical steel tanks (CSTs) which are exposed to external pressure. The requirements of single secondary stiffening ring have been investigated in detail in previous studies. However, in same cases, a single SSR does not provide sufficient resistance to maintain stability over the entire shell height. Thus, buckling capacity of the CSTs with two identical secondary stiffening rings have been explored in this present work. Pursuant to this aim, the requirements for stiffness of the SSRs which are given in terms of minimum second moment of area (SMA) were evaluated by performing Linear Elastic Bifurcation Analysis (LBA) of CSTs under uniform external pressure. Analysis results show that minimum SMA expression proposed by Blackler underestimates critical buckling value for the tanks, having especially low height-to-diameter ratios and low radius-to-thickness ratios. Furthermore, to trace strength reduction in the tank due to geometrical imperfections, Geometrically Nonlinear Analysis including Imperfections (GNIA) was performed. Analysis findings affirm that thin-walled structures are very sensitive to geometrical imperfections.

ARTICLE INFO

Article history:
Received 16 June 2022
Revised 13 July 2022
Accepted 28 July 2022

Keywords:
Cylindrical steel tanks
External pressure
Buckling
Imperfections
Secondary stiffening rings

1. Introduction

Cylindrical shells (CSs) are commonly employed in many structural and engineering applications such as cooling towers, chimneys, silos, tanks and pipelines. In these types of the cylindrical structures, curved thin steel plates are commonly used to form shell courses of storage tank structures. Using welds or bolts, the courses are mounted on each other to form the entire tank shell wall (Shokrzadeh and Sohrabi 2016a; 2016b, Hu et al. 2019; Mehretehran and Meleki 2022). Since these structures have small wall thickness, they are vulnerable to buckling due to external or internal loads, which are two main type of loads that they are subjected to. Pressures from the stored product and vacuum pressure due to process can be classified as internal loads. On the other hand, seismic action and wind are considered external loads. Seismic effects on the tank structures have been extensively studied by many researchers (Haroun and Housner 1981; Çelik et al. 2018, 2019; Hamdan 2000; Maheri and Abdollahi 2013; Güray and Yazici 2015; Spritzer and Guzey 2017a, 2017b; Çelik and Köse 2020; Çelik 2022). Effect of external pressure such as wind on the cylindrical shell structures was studied by Esslinger

* *Corresponding author*. Tel.: +90-252-211-1931 ; Fax: +90-252-211-1912 ; E-mail address: ozerzeybek@mu.edu.tr (Ö. Zeybek)
ISSN: 2149-8024 / DOI: https://doi.org/10.20528/cjsmec.2022.03.003

Nomenclature

t	thickness of the shell
H	height of the cylindrical shell
r	the radius of the cylindrical shell
D	the diameter of the cylindrical shell
E	modulus of elasticity
I_x	minimum second moment of area expression
$I_{x,\text{Blackler}}$	minimum second moment of area expression proposed by Blackler
ν	Poisson's ratio
q_{cr}	circumferential classical elastic buckling pressure
q_{LBA}	critical buckling pressure obtained from LBA
q_{GNIA}	critical buckling pressure obtained from GNIA
u_r	radial displacement

and Geier (1976), Guggenburger (1995), Greiner (2001), Sosa and Godoy (2010), Cao et al. (2018), Zeybek et al. (2019, 2021), Zeybek (2021), Zdravkov (2022), and Zeybek and Topkaya (2022). Either uniform or non-uniform external pressure was considered in these studies. Furthermore, the thin walls make the tank more vulnerable to instability under external pressure when empty or at low levels (Ansourian 1992; Flores and Godoy 1998; Maraveas 2015). Improving strength and stiffness of the tank can be performed with an increase in the wall thickness of it. However, this solution may not be economical in some cases. Another alternative is to use stiffening rings. Two main stiffening ring types for CSs are illustrated in Figs. 1-3, which are primary stiffening ring (PSR) and the secondary stiffening ring (SSR) (Zeybek 2022).

The primary job of PSR (Figs. 1-3) is restraining ovalization at the top of CSTs when the external pressure exposed to tank. The full tank height is stabilized by PSR in open-top tanks (EN 14015 2004). It is placed around the top of CSTs (EN 14015 2004; EN 1993-4-2 2007; API 650 2013). PSR can sometimes be called as the wind girder (Zeybek et al. 2021; Zeybek and Topkaya 2022). On the other hand, PSR having small dimensions may be used for fixed roof tanks since the roof system attached to the top of the cylindrical shell provides a natural restraint at this location (Zeybek 2022).

Zeybek et al. (2019, 2021), and Zeybek and Topkaya (2022) investigated both the requirements for strength and stiffness of the PSRs. Practical expressions for the stress resultants and required second moment area of the PSR were developed by considering interaction between CS and PSR. Furthermore, buckling strength curves were proposed for the open-top tanks by considering different imperfection amplitudes.

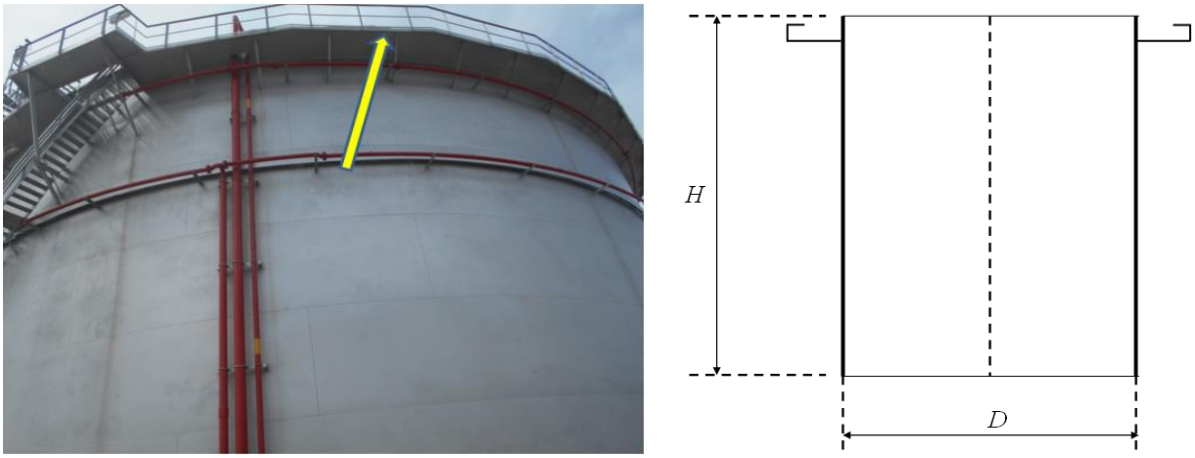

Fig. 1. A cylindrical steel tank with a PSR (https://epcmholdings.com/introduction-to-storage-tanks/).

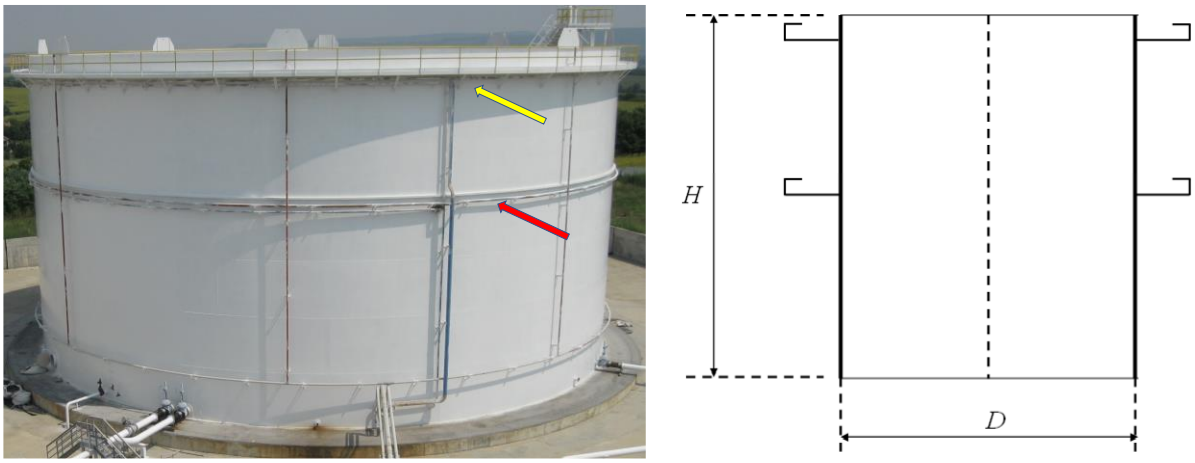

Fig. 2. A cylindrical steel tank with a PSR and a single SSR (courtesy of Dr. Zdravkov).

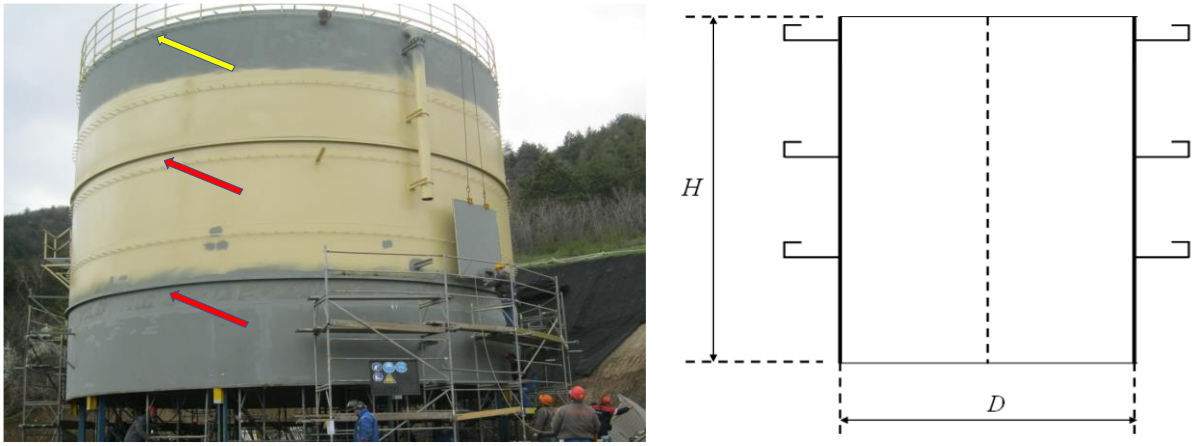

Fig. 3. A cylindrical steel tank with a PSR and a two SSRs (courtesy of Dr. Zdravkov).

When the PSR does not have enough strength for buckling resistance, it is expected that a global buckling can be formed, i.e., the edges of CSTs and the PSR buckle together (Schmidt et al. 1998; Sun et al. 2018). Both PSR and SSR are designed to not buckle even though the shell wall buckles. For both open-top and fixed roof CSTs, one or more SSRs may be necessary to prevent local buckling of the CSTs under external pressure. Sun et al. (2018) examined the open-topped CTSs with PSR and one SSR exposed to wind loads. The possibility of reducing sizes of stiffening rings was investigated by making use of numerical studies.

Zeybek (2022) developed the design expressions for anchored open top tanks with a single SSR. Both required stiffness and strength of the single SSR were obtained from proposed shell-ring stiffness ratio. A new criterion for the stability design of the tanks with one SSR was developed by considering shell-ring interaction.

2. Linear Elastic Bifurcation Analyses (LBA) to Evaluate the Current Approach to SSR Size

The buckling behavior of unstiffened CSs which were exposed to external pressure was examined by many researchers (von Mises 1914; Southwell 1913a, 1913b, 1915; Flugge 1932; Batdorf 1947; Ebner 1952; Donnell 1956, 1958). Based on these comprehensive studies, circumferential classical elastic buckling pressure was proposed as follows:

$$q_{cr} = 0.92E\left(\frac{t}{r}\right)^2\left(\frac{\sqrt{rt}}{H}\right) \quad (1)$$

As mentioned before, the most economical path of increasing the buckling resistance of the CS is to use SSRs (Greiner 2001). However, the main challenge for many designers is determining the required ring size. Many researches were conducted to obtain proper size of the ring. Biezeno and Koch (1939) showed that usage of a stiffening ring may increase load carrying capacity of the CS and it may assist to prevent out-of roundness of the shell under external pressure. Blackler (1986) investigated buckling resistance of the CS structures, which were uniformly exposed to external pressure. He proposed a stiffness requirement, which is related to minimum SMA, by considering classical eigenvalue analysis. Based on the simple boundary conditions and constant shell wall thickness, the minimum SMA expression for two identical stiffening rings was obtained as follows:

$$I_{x,\text{Blackler}} = 0.105Ht^3 \quad (2)$$

Abovementioned expression proposed by Blackler (1986) is assessed by considering comprehensive finite element analyses in this part of the study. According to the studies conducted by Godoy (2016) and Rotter et al. (2015), tanks are thinner and squatter structures having r/t ranging between 500 and 3000 ($500<r/t<3000$) and $H/D<1.0$. Thus, the geometrical properties of the tanks used in the numerical study are given in Table 1.

For this purpose, *H/D ratio*, *r/t ratio* and the dimension of the SSRs were selected for prime parameters. H/D ratios of 1.0, 0.75, 0.50, and 0.25 and r/t ratios of 500, 1000, 1500, 2000, 2500 and 3000 were utilized. In the numerical study, a total of 720 analyzes were performed by taking into account the different SSR ring sizes. Finite element software of ANSYS v12.1 (2010) was utilized to assess the effectiveness of current design approach. As demonstrated in Fig. 4, four-node shell elements (shell63) and two-node beam elements (beam4) were utilized to mesh tank shell and two identical SSRs, respectively. All freedoms were restrained at the base of the CS to represent the bottom edge of the CSTs. On the other hand, radial and tangential translational restraints ($U_r = U_\theta = 0$) were performed to the top of the CST to mimic the effects of the steel roof or PSR (Zhao and Lin 2014). E of 200 GPa and ν of 0.3 were utilized. Two identical SSRs were placed at the $H/3$ and $2H/3$ of the CSTs in all numerical models as depicted in Fig. 4. A uniform external pressure was applied around the circumference of the cylindrical shell in the models.

The critical buckling pressure (q_{LBA}) was determined by performing LBA. The requirement of SMA recommended by Blackler (1986) was assessed by taking into account of the entire dataset. Non-dimensional findings are depicted in Figs. 5-8. In this figure, the SMA of the annular plate rings (I_x) is normalized by the SMA recommended by Blackler (1986) ($I_{x,\text{Blackler}}$). q_{LBA} is normalized by the circumferential classical buckling pressure (q_{cr}) given in Eq. (1). It should be noted that normalized values ($I_x/I_{x,\text{Blackler}}$) are plotted on the logarithmic scale.

Table 1. Geometrical properties of the cylindrical steel tanks.

r	t	r/t	H	H/D
6000	12	500	12000	1
6000	6	1000	12000	1
12000	8	1500	24000	1
12000	6	2000	24000	1
12000	4.8	2500	24000	1
15000	5	3000	30000	1
8000	16	500	12000	0.75
8000	8	1000	12000	0.75
12000	8	1500	18000	0.75
12000	6	2000	18000	0.75
12000	4.8	2500	18000	0.75
15000	5	3000	22500	0.75
6000	12	500	6000	0.5
6000	6	1000	6000	0.5
12000	8	1500	12000	0.5
12000	6	2000	12000	0.5
12000	4.8	2500	12000	0.5
15000	5	3000	15000	0.5
12000	24	500	6000	0.25
12000	12	1000	6000	0.25
12000	8	1500	6000	0.25
12000	6	2000	6000	0.25
12000	4.8	2500	6000	0.25
15000	5	3000	6000	0.25

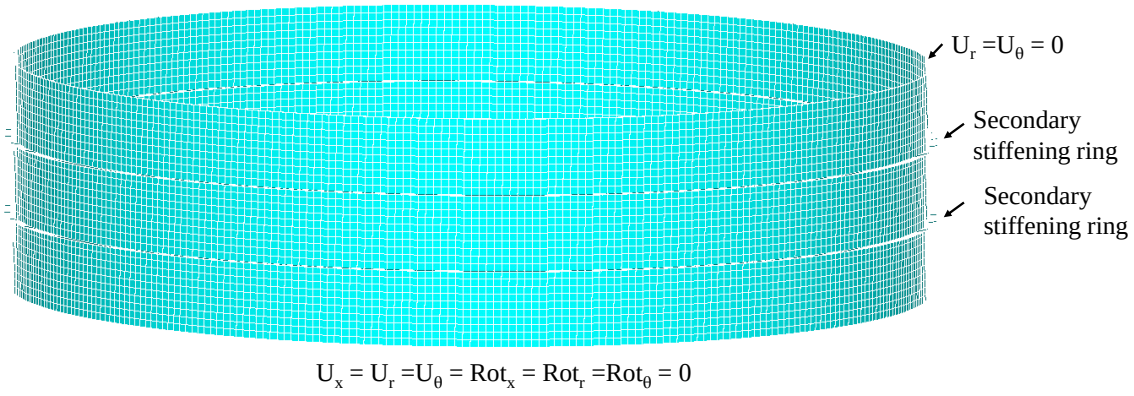

Fig. 4. Finite element modelling of a representative tank with two SSRs.

As shown in Fig. 5, proposal of Blackler (1986) provides sufficient stiffness for the secondary stiffening rings in the cylindrical shells having radius-to-thickness (r/t) ratio ranging between 500-3000. Two bounds (unstiffened and fully stiffened) are also shown in the same figures. In unstiffened case, there is no secondary stiffening ring in the cylindrical shells; however, relatively stiff two SSRs are installed in the fully stiffened case. For the unstiffened case, the normalized buckling pressures (q_{LBA}/q_{cr}) converge to the value of 1.25. On the other hand, normalized buckling pressures are 3.37, 3.28, 3.24, 3.23, 3.20, 3.19 for r/t of 500, 1000, 1500, 2000, 2500 and 3000 respectively, taking into account fully stiffened case considered.

In the same manner, Fig. 6 shows that Blackler's (1986) recommendation is almost sufficient for the all cases in the H/D of 0.75. For the unstiffened case, the normalized buckling pressures (q_{LBA}/q_{cr}) converge to the value of 1.25. On the other hand, normalized buckling pressures are 3.45, 3.35, 3.29, 3.27, 3.25, 3.24 for r/t of 500, 1000, 1500, 2000, 2500 and 3000 respectively, taking into account fully stiffened case considered.

Fig. 7 shows that Blackler's (1986) recommendation provides sufficient stiffness for the r/t of 2000, 2500 and

3000 in the H/D of 0.5. However, proposal of Blackler (1986) slightly underestimates required ring sizes for the r/t of 500, 1000 and 1500. For the unstiffened case, the normalized buckling pressures (q_{LBA}/q_{cr}) converge to the value of 1.25. On the other hand, normalized buckling pressures are 3.66, 3.5, 3.4, 3.35, 3.33, 3.31 for r/t of 500, 1000, 1500, 2000, 2500 and 3000 respectively, taking into account fully stiffened case considered.

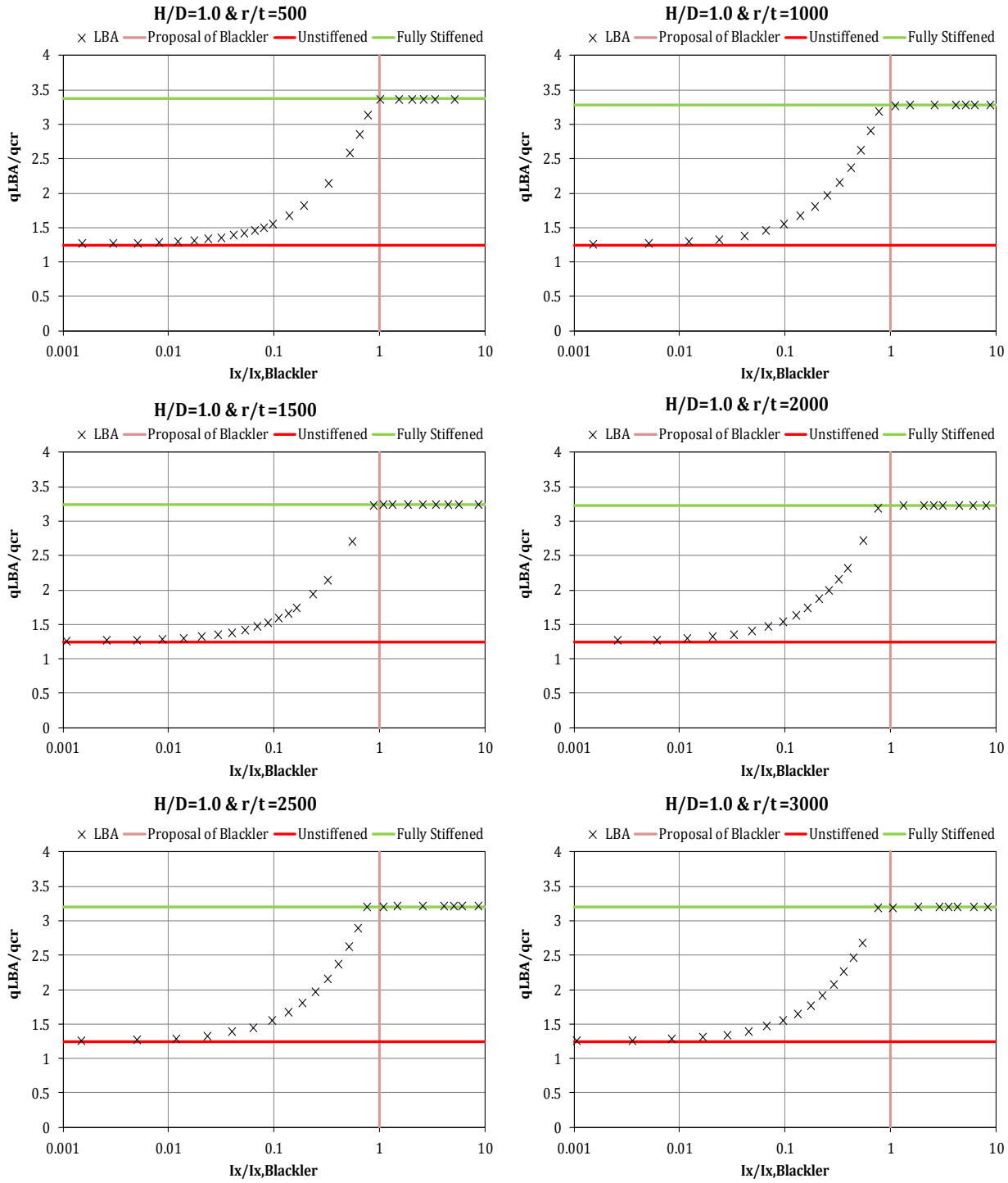

Fig. 5. Evaluation of SMA requirement proposed by Blackler for H/D=1.0.

As shown in Fig. 8, proposal of Blackler (1986) does not provide sufficient stiffness for all cases in the H/D of 0.25. For the unstiffened case, the normalized buckling pressures (q_{LBA}/q_{cr}) converge to approximately the value of 1.25. On the other hand, normalized buckling pressures are 4.56, 3.96, 3.76, 3.67, 3.6, 3.56 for r/t of 500, 1000, 1500, 2000, 2500 and 3000 respectively, taking into account fully stiffened case considered.

As already mentioned, two bounds representing unrestrained shell (no SSRs) and fully restrained with two identical stiff SSRs are also reported in Figs. 5-8. The data points fall in between these two bounds. Furthermore,

the proposed SMA by Blackler (1986) underestimates the critical size of the SSRs, especially for low height-to-diameter ratios and low radius-to-thickness ratios. For instance; ring size should be at least 1.88 times to proposal of Blackler to reach the critical size of the ring for H/D=0.5 with r/t=500 case. On the other hand, for H/D=0.25 with r/t =500 case, ring size should be at least 3.0 times to proposal of Blackler to reach the critical size of the ring.

A typical CST was chosen to investigate modes of buckling of the tank which is uniformly exposed to external pressure by considering different normalized SMA values ($I_x/I_{x,\text{Blackler}}$). For this purpose, a CS having diameter of 6000mm, height of 6000mm, and uniform wall thickness of 12mm was selected (H/D=0.5, r/t=500).

The buckled shapes of CSTs which is uniformly exposed to external pressure are presented for the $I_x/I_{x,\text{Blackler}}$=0.01, $I_x/I_{x,\text{Blackler}}$=0.2, $I_x/I_{x,\text{Blackler}}$=1.0, $I_x/I_{x,\text{Blackler}}$=1.88 in Fig. 9.

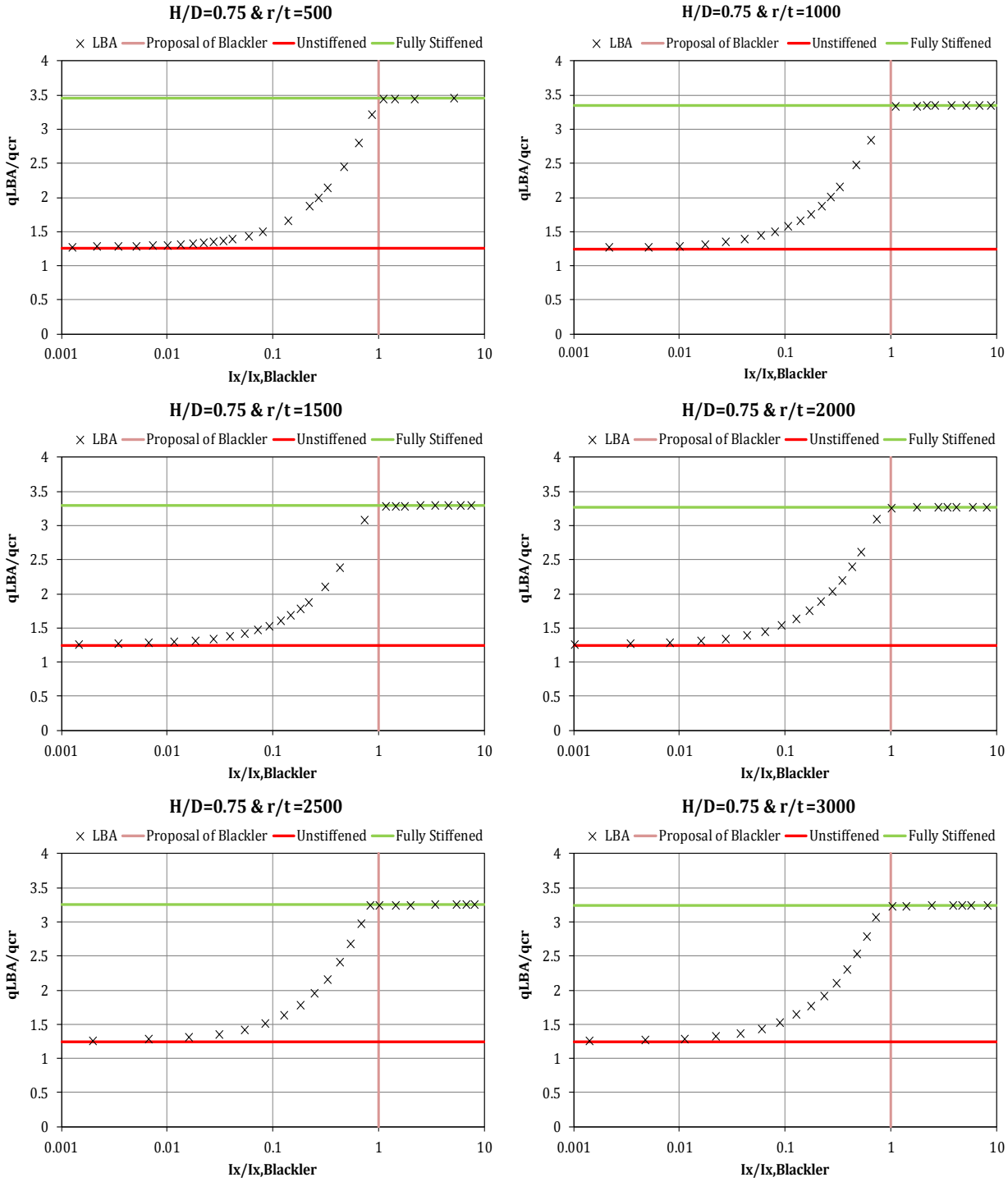

Fig. 6. Evaluation of SMA requirement proposed by Blackler for H/D=0.75.

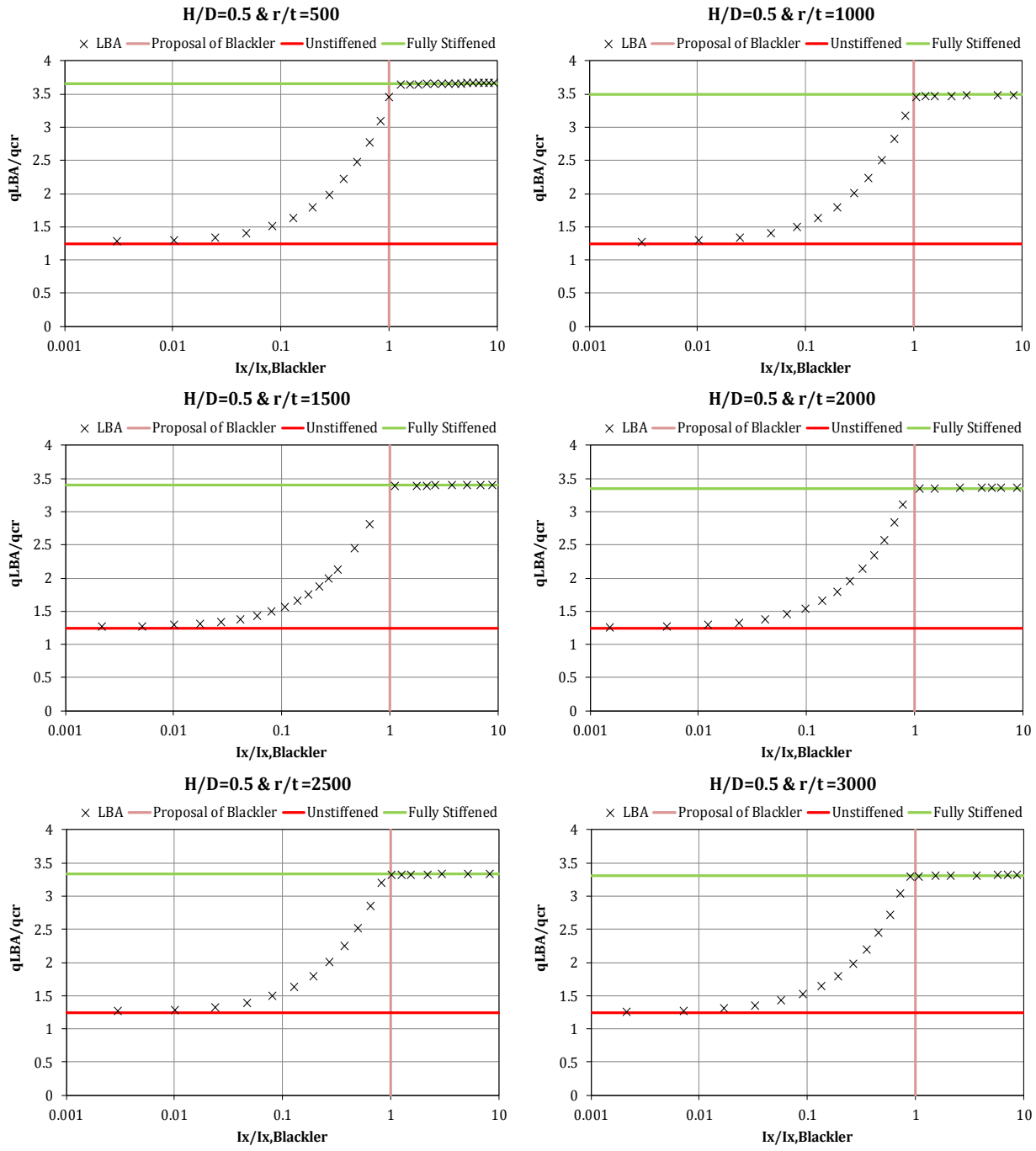

Fig. 7. Evaluation of SMA requirement proposed by Blackler for H/D=0.5.

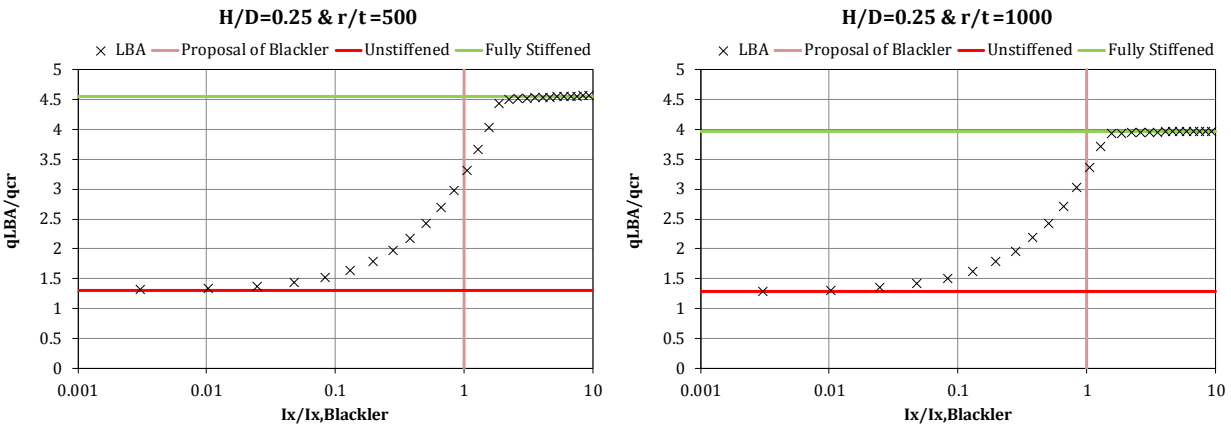

Fig. 8. (continued)

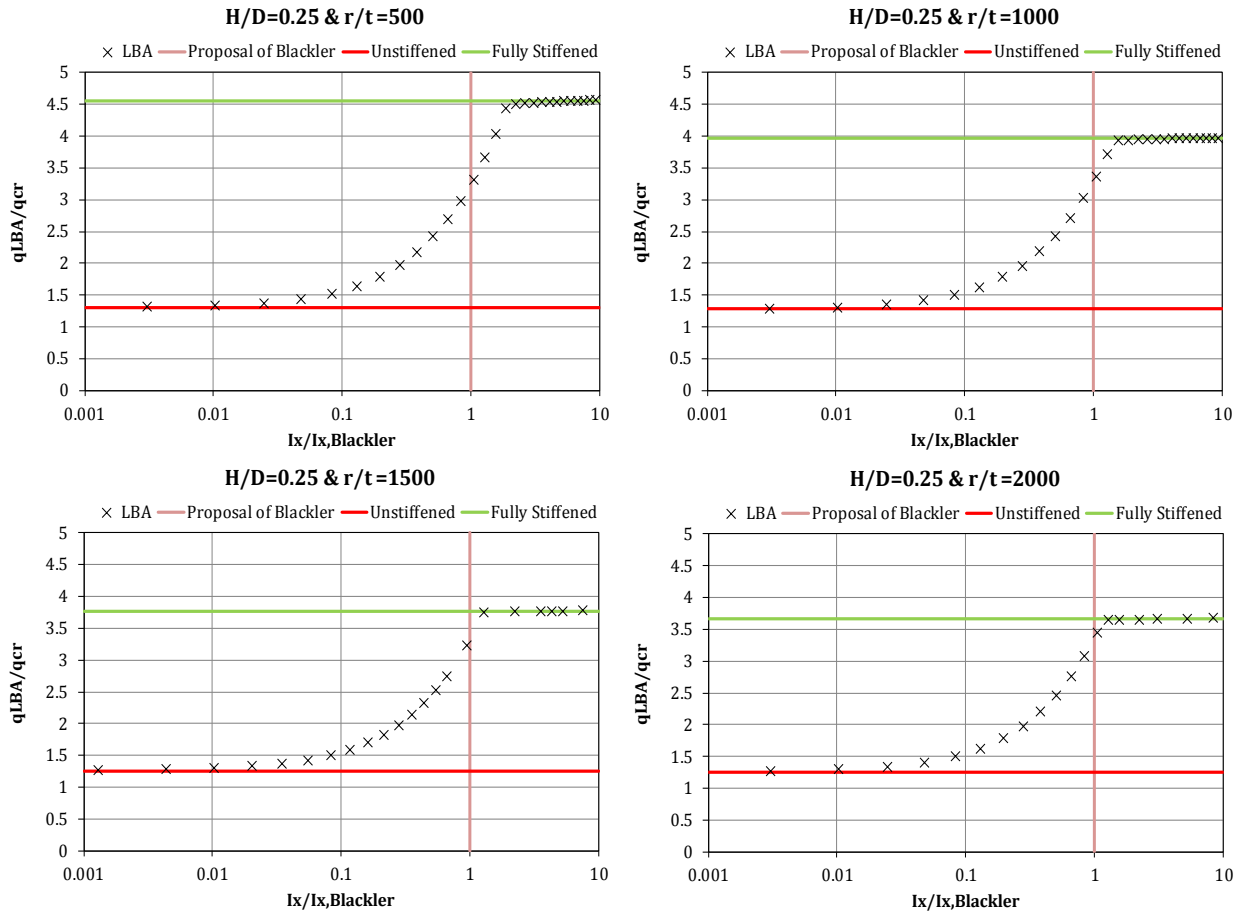

Fig. 8. Evaluation of SMA requirement proposed by Blackler for H/D=0.25.

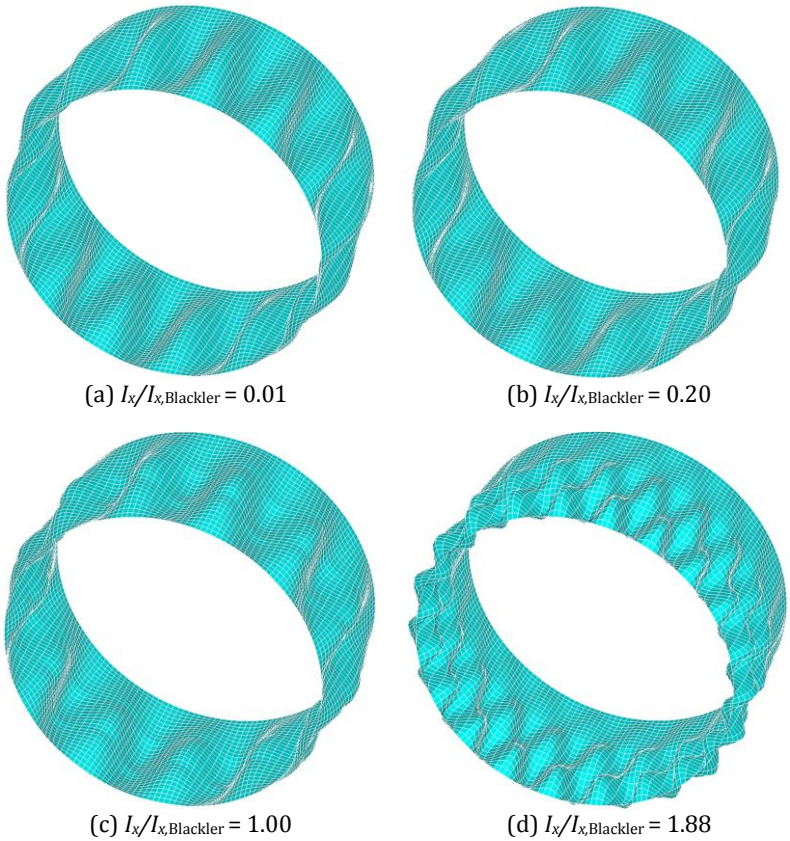

(a) $I_x/I_{x,\text{Blackler}}$ = 0.01 (b) $I_x/I_{x,\text{Blackler}}$ = 0.20

(c) $I_x/I_{x,\text{Blackler}}$ = 1.00 (d) $I_x/I_{x,\text{Blackler}}$ = 1.88

Fig. 9. Buckling mode shapes considering different SMA ratios ($I_x/I_{x,\text{Blackler}}$).

As shown in Fig. 9, the SSRs participate in the buckling of CS when $I_x/I_{x,\text{Blackler}}$=0.01, $I_x/I_{x,\text{Blackler}}$=0.2. Furthermore, for the proposed SMA by Blackler (1986) case ($I_x/I_{x,\text{Blackler}}$=1.0), SSRs are still involved in the buckling mode and critical buckle height is long. To obtain sufficient stiffness, the critical ring size should be at least 1.88 times proposal of Blackler (1986) for the case considering H/D=0.5 with r/t=500.

3. Imperfection Sensitivity of CSTs with two SSRs – Geometrically Nonlinear Analysis Including Imperfections (GNIA)

CSTs generally exhibit severe imperfection sensitivity since they have small wall thickness. Thus, changes in the geometry of CSTs during loading and small deviations in geometry should be taken into account in the design stage. Sonat et al. (2015) reported that geometrical imperfections decrease the elastic buckling capacity considerably under linear bifurcation value. There are many reasons of imperfections (deviations from ideal circular shape) such as constructional defects owing to welded seams between two shell strakes, out-of straightness or ovalization of the CS surface due to fabrication, handling and transporting stages (de Paor et al. 2012; Yan et al. 2021; Godoy 2016). Generally, there are two types of imperfections used in the shell analysis, i.e depressions due to welds and eigen-mode affine imperfection shapes. The most detrimental shape of imperfection (also called eigen-mode affine imperfection shapes) was considered in this phase of the study. This pattern is based on the lowest eigenvalue and, the results are conservatively estimated in terms of strength (Godoy 2016; Sun et al. 2018). Greiner and Derler (1995) reported that short or broad CS structures (low H/D ratio) are the most sensitive to eigen-mode affine imperfections when compared to slender shell structures. Thus, GNIA was carried out on a specific case (H/D=0.25 with r/t=500) to investigate the influence of geometrical imperfections on CSTs subjected to external pressure, 0.1t, 0.25t, 0.5t and 1.0t are chosen as imperfection amplitudes in the numerical model. The radial displacement values (u_r) at mid-height along the stagnation meridian were recorded and normalized by the tank shell thickness (t). Ratio of the buckling pressure loads ($q_{\text{GNIA}}/q_{\text{LBA}}$) are plotted against normalized values (u_r/t) as shown in Fig. 10.

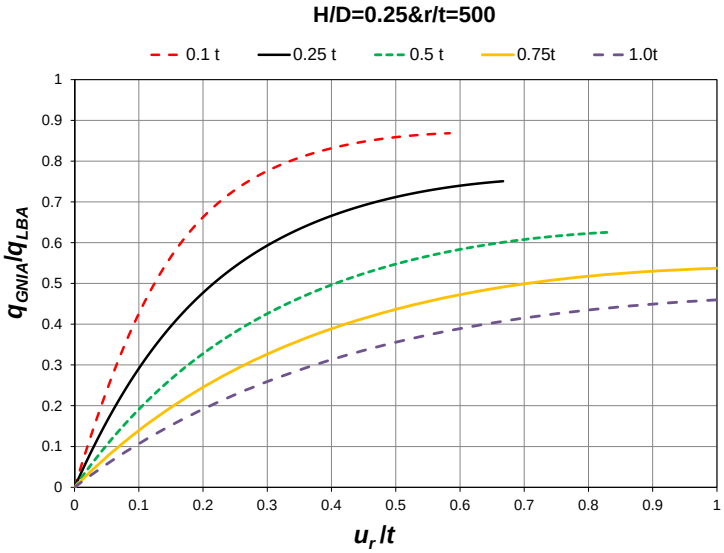

Fig. 10. Relationship between normalized buckling load values and radial displacement for H/D=0.25 with r/t=500 case.

As shown in Fig. 10, as the imperfection amplitude is rised, the buckling strengths determined from GNIA (q_{GNIA}) deviates from q_{LBA}. According to the analysis results, the $q_{cr,\text{GNIA}}/q_{cr,\text{LBA}}$ ratios extend to 0.87, 0.75, 0.63 and 0.46 for imperfection amplitudes of 0.1t, 0.25t , 0.5t, 0.75t and 1.0t, respectively.

4. Conclusions

This paper has examined buckling capacity of CSTs with two identical SSRs under external pressure. Pursuant to this aim, a numerical study was carried out on CSTs with different shell geometries and SSR dimensions by making use of LBA. The analysis results demonstrated that SMA requirement proposed by Blackler (1986) generally provides sufficient strength when the tank structures have high H/D *ratios* and r/t *ratios*. Yet, for low H/D ratios and low r/t ratios, proposal of Blackler underestimates critical buckling pressure of tanks with two identical SSRs. In other words, Blackler's (1986) recommendation generally provides sufficient stiffness for all cases of H/D ratio of 0.75 and 1.0. Proposal of Blackler (1986) slightly underestimates required ring sizes for the r/t of 500, 1000 and 1500 when H/D is equal to 0.5 and for all cases when H/D is equal to 0.25. What is more, GNIA was also executed to examine the influence of geometrical imperfections on buckling strength of the tanks. The first eigenmode (eigenmode-affine pattern) was utilized for imperfection patterns such as 0.1t, 0.25t, 0.5t, 0.75t and

1.0*t*. According to the analysis results, the buckling pressure values obtained from GNIA diverge considerably from LBA results, with a rising difference as the amplitude of imperfection is increased. This means that high imperfection amplitudes lead to a great amount of strength reduction. This affirms that load bearing capacity of the thin-walled CSTs are very sensitive to geometrical imperfections.

Acknowledgements

None declared.

Funding

The authors received no financial support for the research, authorship, and/or publication of this manuscript.

Conflict of Interest

The authors declared no potential conflicts of interest with respect to the research, authorship, and/or publication of this manuscript.

References

Ansourian P (1992). On the buckling analysis and design of silos and tanks. *Journal of Constructional Steel Research*, 23, 273-294.

ANSYS (2010). Version 12.1 On-line User's Manual.

API 650 (2013). Welded tanks for oil storage (12th ed.), American Petroleum Institute, Washington, DC, USA.

Batdorf SB (1947). A simplified method of elastic stability analysis for thin cylindrical shells. NACA TN No.1341.

Biezeno CB, Koch JJ (1939). The buckling of a cylindrical tank of variable thickness under external pressure. *5th International Congress for Applied Mechanics*, ASME, 34-39.

Blackler MJ (1986). Stability of Silos and Tanks under Internal and External Pressure. *PhD thesis*, School of Civil and Mining Engineering, University of Sydney, Australia.

Cao QS, Zhao Y, Zhang R (2018). Wind induced buckling of large circular steel silos with various slenderness. *Thin-Walled Structures*, 130, 101-113.

Çelik Aİ (2022). Impact analysis of cylindrical steel water storage tanks under the seismic action. *International Journal of Advances in Engineering and Pure Sciences*, 34(1), 1-13.

Çelik Aİ, Köse MM (2020). Dynamic buckling analysis of cylindrical steel water storage tanks subjected to Kobe earthquake loading. *Steel Construction*, 13, 128-138.

Çelik Aİ, Köse MM, Akgül T, Apay AC (2018). Directional-deformation analysis of cylindrical steel water tanks subjected to El-Centro Earthquake loading. *Sigma Journal of Engineering and Natural Sciences*, 36(4), 1033-1046.

Çelik Aİ, Köse MM, Akgül T, Apay AC (2019). Effects of the shell thickness on the directional deformation and buckling on the cylindrical steel water tanks under the Kobe Earthquake loading. *Sakarya University Journal of Science*, 23(2), 269-281.

de Paor C, Cronin K, Gleeson JP, Kelliher D (2012). Statistical characterisation and modelling of random geometric imperfections in cylindrical shells. *Thin-Walled Structures*, 58, 9-17.

Donnell LH (1956). Effect of imperfections on buckling of thin cylinders under external pressure. *Journal of Applied Mechanics*, ASME, 23(4), 569-575.

Donnell, LH (1958). Effect of imperfections on buckling of thin cylinders with fixed edges under external pressure. *3rd US National Congress of Applied Mechanics*, ASME, 305-311, New York.

Ebner H (1952). Theoretical and experimental investigations on buckling of cylindrical tanks subjected to reduced pressure. *Stahlbau*, 21, 153-159. (in German)

EN 1993-4-2 (2007). Eurocode 3: Design of Steel Structures, Part 4.2: Tanks, Eurocode 3 Part 4.2, CEN, Brussels.

EN 14015 (2004). Specification for the Design and Manufacture of Site Built, Vertical, Cylindrical, Flat-Bottomed, above Ground, Welded, Steel Tanks for the Storage of Liquids at Ambient Temperature and above. CEN, Brussels.

Esslinger M, Geier B (1976). On the buckling behavior of thin-walled isotropic circular cylinders subjected to external pressure. DVFLR, Institut fur Flugzeugbau, Braunschweig, IB 152-76/03.

Flores FG, Godoy LA (1998). Buckling of short tanks due to hurricanes. *Engineering Structures*, 20(8), 752-760.

Flügge W (1932). Die Stabilität der Kreiszylinderschale. *Ingenieur-Archiv*, 3(5), 463-506. (in German)

Godoy LA (2016). Buckling of vertical oil storage steel tanks: Review of static buckling studies. *Thin-Walled Structures*, 103, 1-21.

Greiner R (2001). Cylindrical Shells under Uniform External Pressure. In: *Buckling of Thin Metal Shells (Ed. Teng JG and Rotter JM)*, Spon Press, London, 154-174.

Greiner R, Derler P (1995). Effect of imperfections on wind-loaded cylindrical shells. *Thin-Walled Structures*, 23(1-4), 271-281.

Guggenburger W (1995). Buckling and postbuckling of imperfect cylindrical shells under external pressure. *Thin Walled Structures*, 23(1-4), 351-366.

Güray E, Yazici G (2015). Sloshing in medium sized tanks under earthquake load. *Gradevinar,* 67(7), 655-662.

Hamdan FH (2000). Seismic behaviour of cylindrical steel liquid storage tanks. *Journal of Constructional Steel Research*, 53(3), 307-333.

Haroun MA, Housner GW (1981). Seismic design of liquid storage tanks. *Journal of Technical Councils of ASCE*, 107(1), 191-207.

Hu W, Bohra H, Azzuni E, Guzey S (2019). The uplift effect of bottom plate of aboveground storage tanks subjected to wind loading. *Thin-Walled Structures*, 144, 106241.

Maheri MR, Abdollahi A (2013). The effects of long term uniform corrosion on the buckling of ground based steel tanks under seismic loading. *Thin-Walled Structures*, 62, 1-9.

Maraveas C, Balokas GA, Tsavdaridis KD (2015). Numerical evaluation on shell buckling of empty thin-walled steel tanks under wind load according to current American and European design codes. *Thin-Walled Structures*, 95, 152-160.

Mehretehran AM, Maleki S (2022). Axial buckling of imperfect cylindrical steel silos with isotropic walls under stored solids loads: FE analyses versus Eurocode provisions. *Engineering Failure Analysis*, 137, 106282.

Rotter JM, Kerr E, Lam HT, Holst JM (2015). Secondary rings for large tanks under external pressure. *Eighth International Conference on Advances in Steel Structures Lisbon*, Portugal.

RV Southwell BA (1913a). On the collapse of tubes by external pressure. *Philosophical Magazine Series 6*, 25(149), 687-698.

RV Southwell BA (1913b). On the collapse of tubes by external pressure–II. *Philosophical Magazine Series 6*, 26(153), 502-511

RV Southwell MA (1915). On the collapse of tubes by external pressure–III. *Philosophical Magazine Series 6*, 29(169), 67-77.

Schmidt H, Binder B, Lange H (1998). Postbuckling strength design of open thin walled cylindrical tanks under wind load. *Thin-Walled Structures*, 31, 203–220.

Shokrzadeh AR, Sohrabi MR (2016a). Buckling of ground based steel tanks subjected to wind and vacuum pressures considering uniform internal and external corrosion. *Thin-Walled Structures*, 108, 333-350.

Shokrzadeh AR, Sohrabi MR (2016b). Strengthening effects of spiral stairway on the buckling behavior of metal tanks under wind and vacuum pressures. *Thin-Walled Structures*, 106, 437-447.

Sonat C, Topkaya C, Rotter JM (2015). Buckling of cylindrical metal shells on discretely supported ring beams. *Thin-Walled Structures*, 93, 22-35.

Sosa, EM, Godoy LA (2010). Challenges in the computation of lower-bound buckling loads for tanks under wind pressures. *Thin-Walled Structures* 48 (12), 935-945.

Spritzer JM, Guzey S (2017a). Nonlinear numerical evaluation of large open-top aboveground steel welded liquid storage tanks excited by seismic loads. *Thin-Walled Structures*, 119, 662-676.

Spritzer JM, Guzey S (2017b). Review of API 650 Annex E: Design of large steel welded aboveground storage tanks excited by seismic loads. *Thin-Walled Structures*, 112, 41-65.

Sun T, Azzuni E, Guzey S (2018). Stability of open-topped storage tanks with top stiffener and one intermediate stiffener subject to wind loading. *ASME Journal of Pressure Vessel Technology*, 140(1), 011204.

von Mises R (1914). Der kritische Ausendruck zylindrischer Rohre. *Zeitschrift des Vereines Deutscher Ingenieure*, 58, 750-755.

Yan XL, Li GQ, Wang YB (2021). Behavior and design of high-strength steel members under bending moment. In: *Behavior and Design of High Strength Constructional Steel (Ed. Li GQ and Wang YB)*, Woodhead Publishing, United Kingdom.

Zdravkov L (2022). Influence of the roof structure on the forces in the top angle under wind loading. *Annual of the University of Architecture, Civil Engineering and Geodesy*, 55(2), 245-254.

Zeybek Ö (2021). Design of cylindrical steel liquid tanks with stepped walls using One-foot method. *Challenge Journal of Structural Mechanics*, 7(4), 162-169.

Zeybek Ö (2022). The stability of anchored cylindrical steel tanks with a secondary stiffening ring. *International Journal of Pressure Vessels and Piping*, 198, 104661.

Zeybek Ö, Topkaya C (2022). Stiffness requirements for wind girders in open-top cylindrical steel tanks. *Thin-Walled Structures*, 176, 109353.

Zeybek Ö, Topkaya C, Rotter JM (2019). Stress resultants for wind girders in open-top cylindrical steel tanks. *Engineering Structures*, 196, 109347.

Zeybek Ö, Topkaya C, Rotter JM (2021). Stability of open-top cylindrical steel tanks with primary stiffening ring under wind loading, *ce/papers*, 4, 1781-1788.

Zhao Y, Lin Y (2014). Buckling of cylindrical open-topped steel tanks under wind load. *Thin Walled Structures*, 79, 83-94.

Challenge Journal of Structural Mechanics

Research Article

Experimental examination of strength and behavior of masonry brick walls strengthened with expanded steel plates

Ezatullah Ahmadzai [a], Zeynep Yaman [a,*], Alper Cumhur [b]

[a] *Department of Civil Engineering, Sakarya University, 54187 Sakarya, Turkey*
[b] *Department of Civil Engineering, Yalova University, 77200 Yalova, Turkey*

ABSTRACT

As primary load-bearing members of masonry buildings, the strength and behavior of masonry brick walls are the most important factors affecting the structural performance for the loads the building is exposed to during its life span. The current paper therefore experimentally examines a structural strengthening method to improve the performance and behavior of masonry brick walls. Masonry walls were strengthened with expanded steel plates of different thicknesses attached to the walls using different numbers of bolts. Five wall specimens were examined under a diagonal static compression test. For strengthening, expanded steel plates were anchored to both sides of un-plastered walls using bolts and were then plastered. The thickness of the steel plates and the number of bolts were examined as experimental variables. The results showed that the strengthened wall specimens using expanded steel plates of different thicknesses and different numbers of bolts increased an average of 45-94% ultimate strength at 245mm displacement, the ductility of all strengthened specimens increased by 114%-180% and an average increment of 280-480% higher energy dissipation capacities compared to the reference specimen. The result shows that strengthening masonry brick walls provides 2 to 3 times higher energy dissipation capacity for the energy generated by seismic effects compared to the reference specimen. The research then indicated the expanded plate thickness in strengthening walls has a direct relation with load-bearing capacity of brick masonry walls. An increase of 33% and 100% in plate thickness resulted to increase in load bearing capacity by 2% and 11.5%, respectively. It has also been observed that specimens did not experience a sudden drop in load carrying capacity. They maintained their stability until the end of the tests and changed their stiffness and ductility.

ARTICLE INFO

Article history:
Received 5 July 2022
Revised 1 August 2022
Accepted 22 August 2022

Keywords:
Masonry brick walls
Strengthening
Expanded steel plates
Diagonal compression test

1. Introduction

Brick masonry structure is one of the preferred and typical method of construction due to several advantages including rapid production, low cost, high heat, and sound isolation (Mezrea et al. 2021; Özyurt et al. 2020; Hejazi et al. 2015; Budak et al. 2004). Brick masonry buildings are very common in Turkey; however, these structures need to be strengthened due to their heterogeneity and mechanical properties. Since brick, the main material of the building structure, does not have sufficient ductility for tensile and shear stresses (İstegün et al. 2018), it exhibits a low energy dissipation capacity (Koç 2016; Korkmaz 2014; Çırak 2011). Low ductility and energy dissipation capacity of brick masonry buildings can cause sudden damage to the walls (Cheng et al. 2020). Therefore, strengthening interventions are required for a great portion of the existing brick masonry buildings to improve structural strength and behavior (Marques et al. 2022; Orulkaya 2019).

As load-bearing members, brick masonry walls are forced to make plastic deformation and displacement in

* *Corresponding author*. Tel.: +90-264-295-5744 ; Fax: +90-264-295-5601 ; E-mail address: zdyaman@sakarya.edu.tr (Z. Yaman)
ISSN: 2149-8024 / DOI: https://doi.org/10.20528/cjsmec.2022.03.004

multi directions with altered amounts under the different types of loads (forces) that the structure is exposed to. The difference in displacements depends on the stiffness of the masonry brick walls (Bahçekapılı 2003). Strength of a masonry building depends on both the bond between brick and mortar (Karaton and Çanakçı 2021) as well as the strength of the masonry material (Güvenir 2019; Erköseoğlu 2014). Although brick masonry walls have sufficient strength under vertical loads (gravity loads, live loads, etc.), they don't have sufficient strength for lateral loads (earthquake loads, etc.). To increase lateral strength and load-bearing capacity, new strengthening techniques should be introduced. The applicability of such a new strengthening technique depends on minimizing the environmental and economic effects of the method (Mezrea et al. 2021).

Many previous studies presented strengthening practices for buildings and structural members (Maali et al. 2019; Aydin et al. 2020; Ağcakoca 2020). In addition, some studies focused on wall strengthening applications. In the past reports, different methods were used for strengthening brick infill walls and brick masonry walls using plaster (Arslan et al. 2020; Sevil et al. 2010), concrete (Kaya 2013; Baran et al. 2014; Ateş 2013; Kalkan 2008), epoxy resin and fiber-reinforced polymer strips (Abdulsalam et al. 2021; Kalali and Kabir 2012), textile (Koutas et al. 2014), and some other materials (Rebelo et al. 2021; Corradi et al. 2020; Hamdy et al. 2018; Chen et al. 2012; Ozsayin et al. 2011; Mosallam 2007; Ehsani et al. 1999). In these studies, strengthened specimens exhibited higher ductility, load-carrying capacities, energy dissipation capacities, stiffness, and seismic resistance performances. Furthermore, brick infill walls were also strengthened using steel profiles (Özbek et al. 2012), steel plates (Papanicolaou et al. 2011), expanded steel plates (Leeanansaksiri et al. 2018; Aykaç et al. 2017; Cumhur 2016), perforated steel plates (Özbek et al. 2019; Özbek 2015; Seydanlıoğlu 2013; Babayani 2012), steel mesh (Tekeli et al. 2014; Özdemir and Eren 2011), steel strips (Özmen 2018) and the impact of strengthening on the behavior of the load-bearing system were examined (Johansson, et al. 2014; Sevil et al. 2010). The results of these studies showed that the load-bearing capacity, energy absorption capacity, diagonal compression capacity, stiffness, and ductility of the reinforced specimens increased.

This research aims to fill the gap in the literature by presenting experimental evidence for strengthening brick masonry walls with expanded steel plates, which is a practical and environmental friendly strengthening method. Since the use of masonry members is a common construction method in Turkey, the strengthening method examined in this study is important as an accessible technique to users in Turkey.

This study presents a rapid and practical technique for strengthening the currently existing and future masonry building walls to improve lateral rigidity and strength of the structure, prevent out-of-plane behaviors of the walls exposed to earthquake loading, and ensure life and structural safety. The study was carried out on 5 test specimens (samples); one was normal wall (reference) and four were strengthened wall specimens. In the experimental study, diagonal static incremental loading was applied to the specimens. For strengthening, expanded steel plates were installed and fixed on both sides of the un-plastered walls using bolt connection. The effect of expanded steel plate thickness and the number of bolts on the wall load-bearing bear capacity were then examined and analyzed under loading.

2. Material and Method

To produce test specimens, expanded steel plates manufactured in Turkey and vertical-hole blocks which are widely used in masonry building construction in Turkey were used in the lab experiments. Standard construction workmanship was performed in the production of the specimens. As load-bearing members in masonry buildings, strengthening of the walls made of vertical-hole blocks with dimensions 135×190×290 mm was examined. A total of 5 sample walls, each with dimensions of 1000x1000 mm (one was the reference and four were strengthened) were tested (Table 1).

The specific weight (γ) of the bricks used in the study was 700 kg/m^3. To determine the characteristics of the bricks, 30 bricks were separately tested to find the brick properties (Fig. 1). The compressive strength of the bricks was examined according to the TS EN 772-1+A1 standard (Table 2).

The thicknesses of the expanded steel plates were 1.5, 2.0, and 3.0 mm with an average yield strength (σ_y) of 280 MPa. The steel plates were processed in a factory using cutting and expanding procedures, and expanded steel plates with perforations having dimensions of 54x26 mm were obtained. No welding or mounting procedures were applied on expanded steel plates (Fig. 2(a)).

Table 1. Specimen properties.

Specimen	Plaster thickness (mm)	Plate thickness (mm)	Bolt interval (mm)	Number of bolts
Reference	25	-	-	-
MBW 1.5-150	25	1.5	150	49
MBW 2.0-150	25	2.0	150	49
MBW 3.0-150	25	3.0	150	49
MBW 3.0-400	25	3.0	400	9

MBW = Masonry Brick Wall

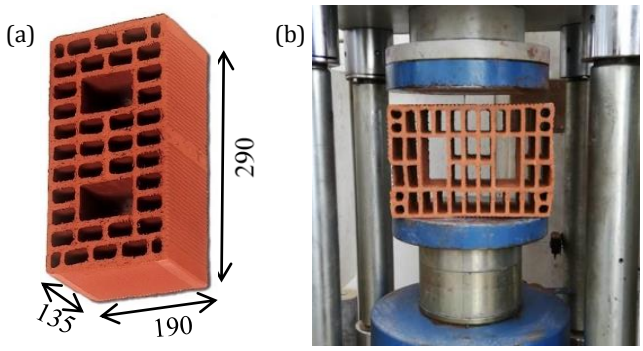

Fig. 1. (a) Vertical-hole brick; (b) Compressive strength tests.

Table 2. Compressive strength tests results of the vertical-hole brick.

		Mean breaking load (kN)	Compressive strength (MPa)
Parallel to holes	Mean	169.6	3.3
	SD	51.4	1.0
Long axis perpendicular to holes	Mean	124.5	3.3
	SD	24.5	0.7
Short axis perpendicular to holes	Mean	30.5	1.3
	SD	11.7	0.5

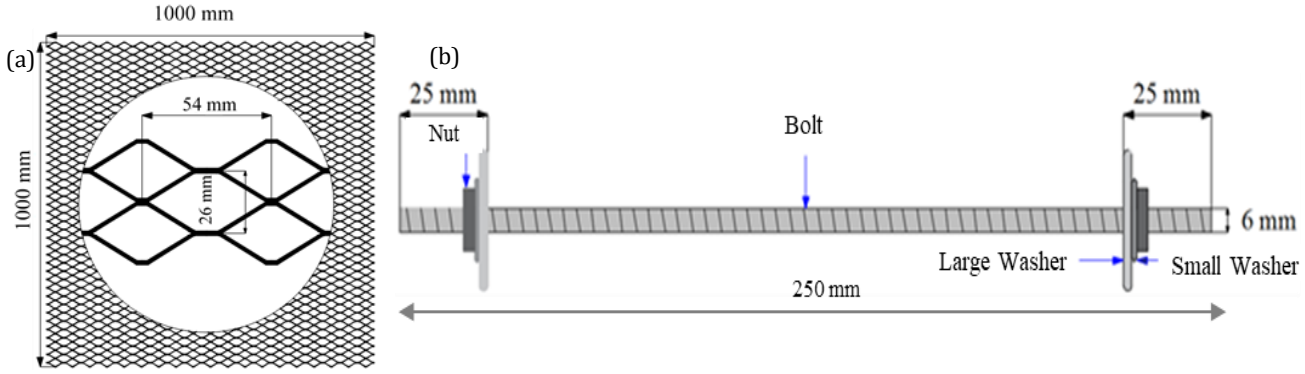

Fig. 2. Materials used in wall strengthening: (a) Expanded steel plate; (b) Geometries of the bolt, washer, and nut.

To attach expanded steel plates to the walls, bolts, washers, and nuts were used (Fig. 2(b)). The bolts were produced by cutting 250 mm-long pieces from 6-mm fully threaded 1-m long S235 steel bars.

Holes were drilled at the determined points on the wall specimens with a drill, expanded steel plates were then placed on the walls, and fixed using bolts, washers, and nuts (Figs. 3 and 4).

Fig. 3. (continued)

Fig. 3. Preparation of the experimental setup.

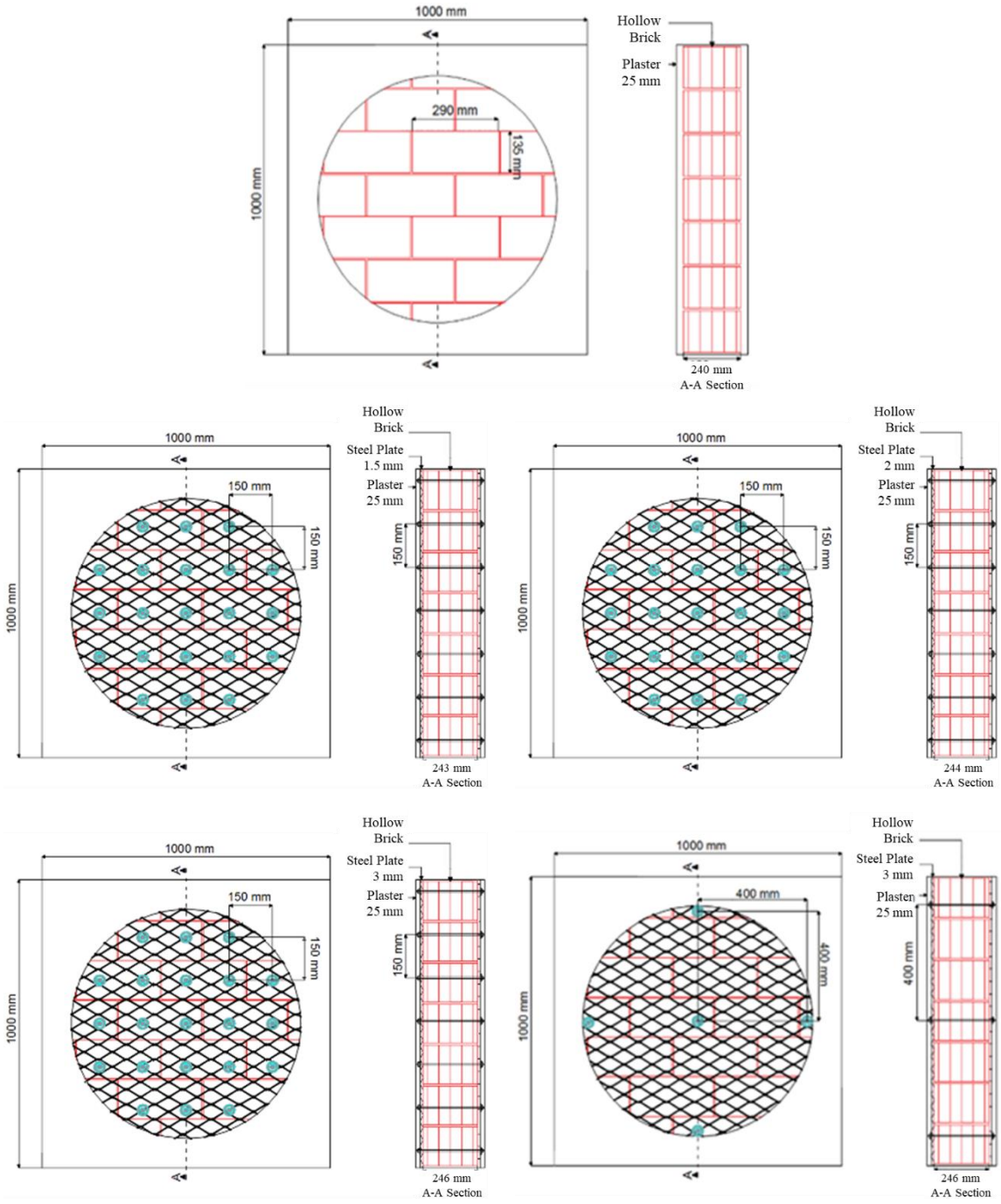

Fig. 4. Design of the test specimens.

The bolts were tightened with 3 Nm tightening torque considering the post-tensioning stress. The same mix composition was used for preparing plaster and mortar. Wall mortar and plaster mixes were prepared using the water-sand-lime-cement ratio given in Table 3.

In the experimental examinations, diagonal compression loading was applied. According to the definition of the diagonal compression test in the ASTM E519, 1/8 of the side span of the side edges to the diagonal loading point are fastened by loading shoes and other parts of the edges are set free during the loading. However, in the real case, depending on earthquake-induced displacements, the contact area of the brick masonry walls with the lateral and vertical peripheral ties can be higher than specified in ASTM E519 (Cumhur et al. 2016). Therefore, in this study, square steel frames with (internal) dimensions of 1000×1000 mm used by Cumhur et al. (2016) to transfer the diagonal load to infill wall specimens (Fig. 5). Steel frames were produced by hinged connected profiles. Hinges ensured transferring the entire applied diagonal load to the test specimens and that the steel frame does not resist to loading.

Table 3. Weight ratio of the materials used in plaster and mortars.

Material	Water	Lime	Sand	Cement
%	10	10	60	20

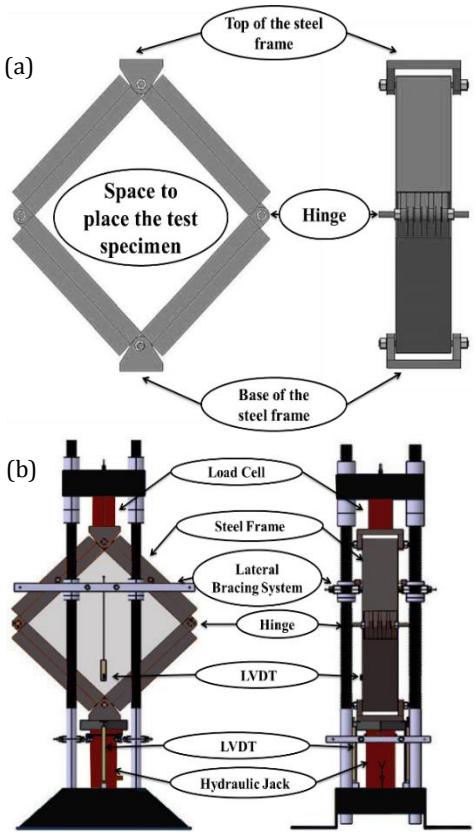

Fig. 5. Experimental study: (a) Steel rigid frame with hinged from four edges; (b) Loading test setup.

Out-of-plane behavior of the frame was prevented using stiffness elements (lateral support system). Thus, the load was transferred to the test specimen diagonally from the center of the frame. The load was applied to the test specimen using single action 1000 kN hydraulic jack (Fig. 6) through a speed-controlled loading system depending on the displacement. The loading speeds varied according to the displacements as follows: 5% up to 10 mm displacement, 25% up to 10-35 mm displacement, and 50% beyond 35 mm displacement.

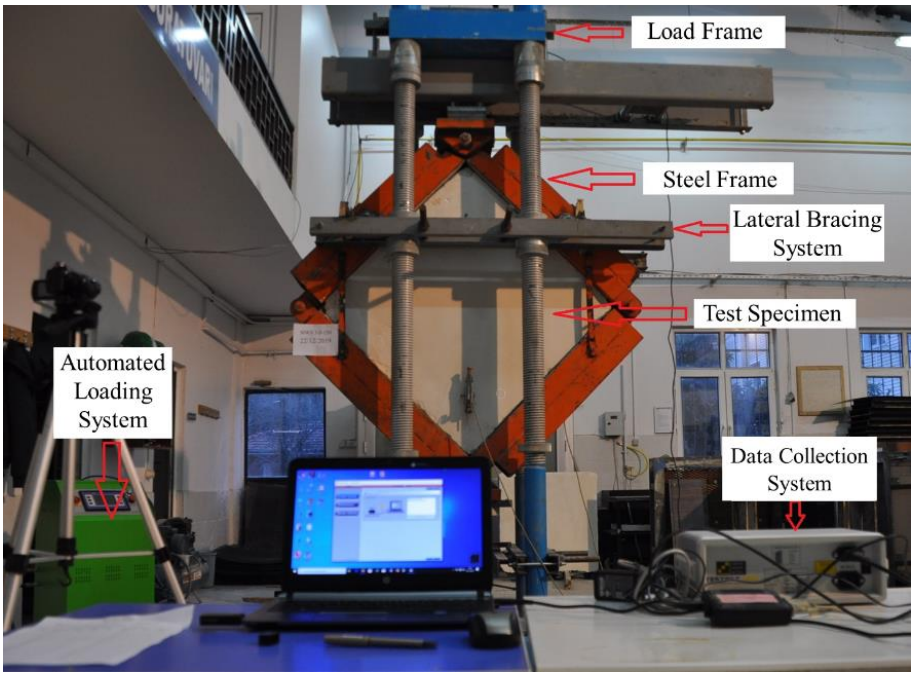

Fig. 6. Test setup.

To measure the displacements in the test specimens, 4 LVDT (Linear Variable Differential Transformer) were used. Two 400 mm LVDT were attached to the base of the rigid frame to measure shortenings of the specimens along the loading axis. Two 50 mm LVDT were placed on the front and back of the test specimens to measure shortenings of the specimens along the loading axis and elongation perpendicular to the loading axis (Fig. 7).

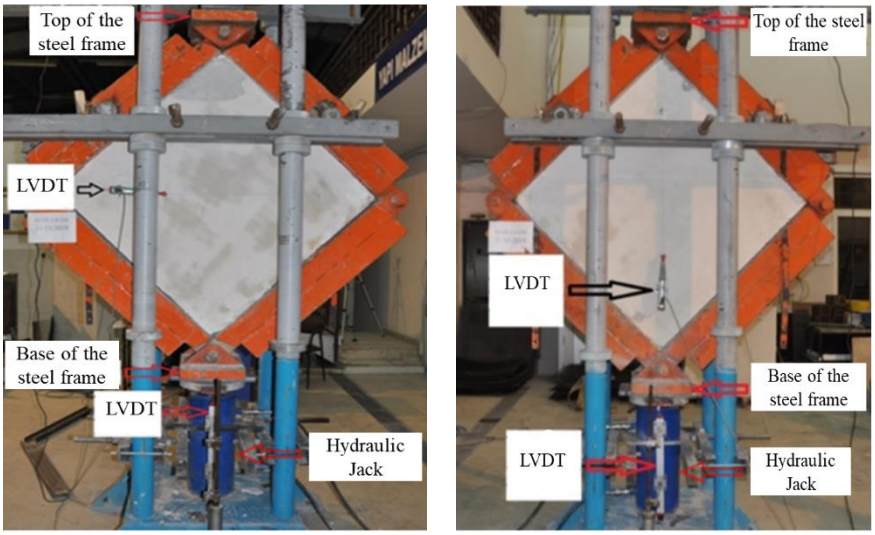

Fig. 7. Placement of LVDTs.

3. Analysis of the Experimental Results

Only plastering layer was applied to both sides of the reference specimen and no strengthening material was used. During the tests, the reference specimen exhibited very brittle behavior and had abrupt load drops. Since abrupt load drops occurred and the reference specimen showed non-ductile behavior, a very limited amount of displacement was observed. After the test started, fine hairline cracks were observed on the both front and back plaster surfaces at a load of 60 kN and a displacement of 31 mm. The first crack was observed 20 cm from the right side of the middle diagonal of the specimen at a load of 85 kN and a displacement of 36 mm. The width of the first crack was measured to be approximately 3 mm. Towards the end of the experiment, the cracks continued to grow and blisters became more evident. The maximum load-carrying capacity of the reference specimen was measured 99.87 kN and the displacement was recorded 25.9 mm. The test was terminated after a displacement of 90 mm since the specimen no longer carry any loads. The contact surface of the reference specimen was measured as about 70% (70 cm).

For the specimen MBW 1.5-150, obvious blisters progressing towards the frame was observed on both front and back surfaces of the specimen around the hinges at a load of 125 kN and a displacement of 91 mm. The maximum load-carrying capacity of the specimen was noted 154.65 kN and the displacement at this load was counted 65.5 mm. The contact surface of the specimen was measured as 65% (65 cm) on average.

For the specimen MBW 2.0-150, obvious lateral blistering was observed on both front and back surfaces of the specimen around the lower hinge due to compression at a load of 141 kN and a displacement of 64 mm. Plus, some blistering progressing towards the frame around the hop hinge was also observed. The maximum load-carrying capacity of the specimen was found to be 160.2 kN and the displacement at this load was calculated as 34 mm. The contact surface of the specimen MBW 2.0-150 was measured as 58% (58 cm) on average.

For the specimen MBW 3.0-150, hairline cracks were observed on the middle region of the plaster both on front and back surfaces of the specimen at a load of 147 kN and a displacement of 28 mm. Furthermore, a significant plaster crack in the loading direction was observed on the back surface of the specimen near the lower hinge and blistering around the top hinge due to compression. On the other hand, at a load of 135 kN and a displacement of 122 mm, lateral cracks and about 30 cm above the lower hinge blistering on both front and back surfaces and plaster blisters progressing towards the frame were observed due to compression. The maximum load-carrying capacity of the specimen MBW 3.0-150 was found to be 160.35 kN and the displacement at this load was calculated as 36.76 mm. The contact surfaces of the specimen MBW 3.0-150 on four corners were measured as 48% (48 cm) on average.

Finally, for the specimen MBW 3.0-400, hairline plaster cracks in the middle region of the front surface were observed at a load of 145 kN and a displacement of 28 mm. Plus, plaster blistering and falling off occurred on the front surface of the specimen near the top and lower hinges due to compression. The maximum load-carrying capacity of the specimen was calculated as 147.28 kN and the displacement at this load was found to be 23.59 mm. The contact surface of the specimen MBW 3.0-400 was measured as 60% (60 cm) on average.

The undamaged state of the specimens, the damage condition after the test and the load-displacement curves are shown in Fig. 8.Test results were summarized in Table 4.

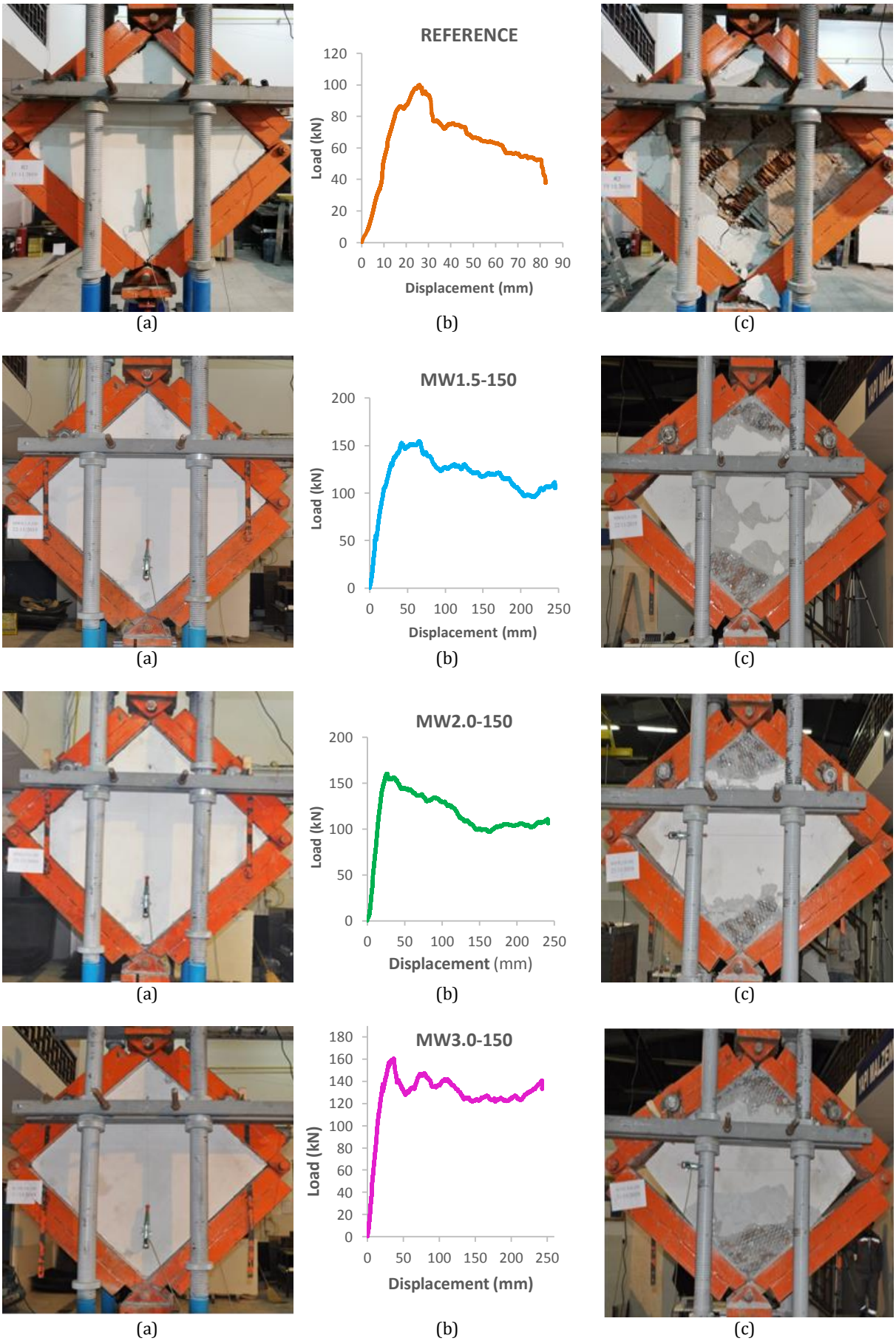

(a) (b) (c)

(a) (b) (c)

(a) (b) (c)

(a) (b) (c)

Fig. 8. (continued)

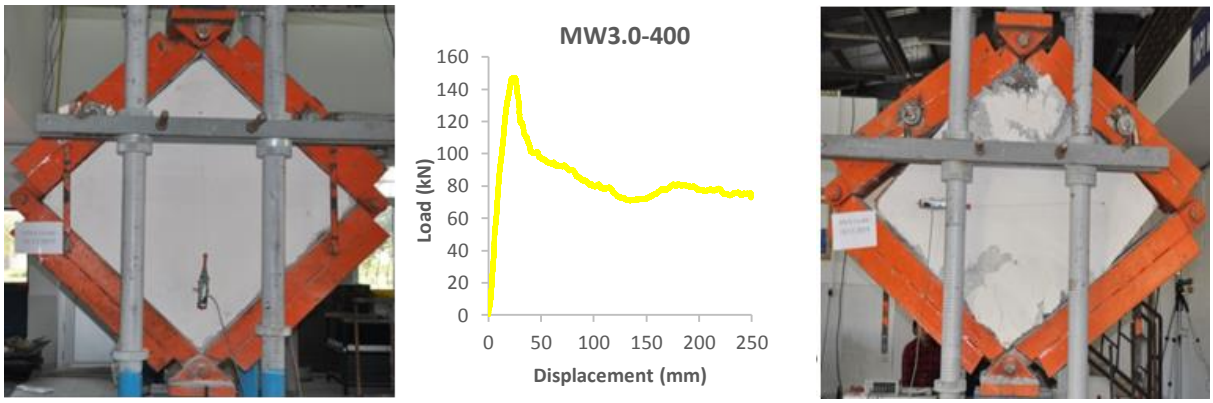

(a) (b) (c)

Fig. 8. Test members: (a) Before the test; (b) Load-displacement curve; (c) After the test.

Table 4. Maximum load-carrying capacities and contact areas of the specimens.

Specimen	Max load (kN)	Displacement at maximum load (mm)	Contact area at maximum load (%)	Maximum displacement (mm)	Average contact area (%)
Reference	99.87	25.91	48.75	82.38	70
MBW 1.5-150	154.65	65.51	39.50	245.25	65
MBW 2.0-150	160.20	34.02	29.50	241.70	58
MBW 3.0-150	160.35	36.76	30.50	243.13	48
MBW 3.0-400	147.28	23.59	18.00	249.18	60

The carrying capacity, stiffness, and ductility capacities of the specimens were calculated according to Fig. 9 using the test results. In the curve, (P_y) is load-carrying capacity at yield, (δ_y) is displacement at yield, (P_{max}) is maximum load-carrying capacity, (δ_0) is displacement at maximum load, (δ_f) is maximum displacement, (P_f) is load-carrying capacity at maximum displacement, (δ_i) is displacement at the beginning of the stiffness curve, (P_t) is load-carrying capacity, and (δ_t) is the displacement corresponding to P_t.

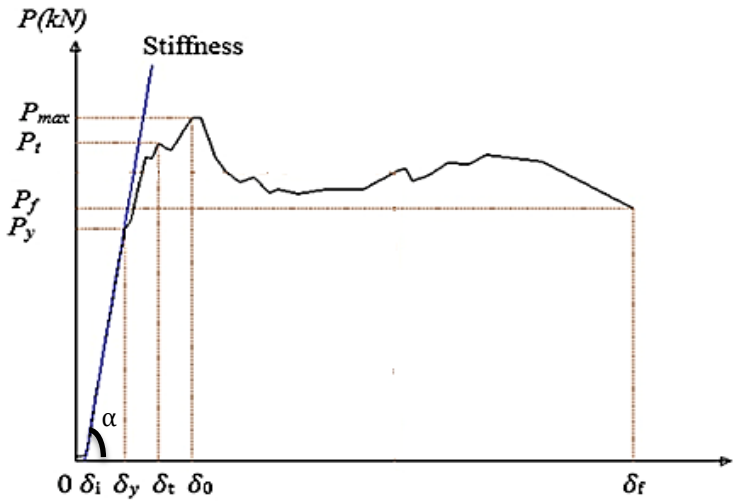

Fig. 9. A sample load-displacement curve used to calculate the ductility of the specimens.

Load-carrying capacity at yield (P_y), maximum load-carrying capacity (P_{max}), load-carrying capacity at maximum displacement (P_f), and relative increase in the ultimate strength values according to the reference specimen are given in Table 5. Ultimate strength values were calculated using the average of (P_{max}) and (P_f) values (Cumhur 2016).

The initial stiffness of the specimens was calculated using the ratio of yield load (P_y) to displacement at yield (δ_y^-) (Table 6).

Table 5. Ultimate strength values and relative increase according to the reference specimen.

Specimen	P_y (kN)	P_{max} (kN)	P_f (kN)	Ult. strength at 245mm displacement (kN)	Relative increase in ult. Strength (%)
Reference	86	99.87	51.3	75.59	-
MBW 1.5-150	105	154.65	108.18	131.42	73.86
MBW 2.0-150	140	160.20	108.15	134.18	77.52
MBW 3.0-150	147	160.35	132.88	146.62	93.97
MBW 3.0-400	140	147.28	72.68	109.98	45.51

Table 6. Stiffness and relative increase in stiffness according to the reference specimen.

Specimen	P_y (kN)	δy (δ_y^-) (mm)	Stiffness (kN/mm)	Relative increase in stiffness (%)
Reference	86	17(15)	5.73	-
MBW 1.5-150	105	18(16)	6.56	14.46
MBW 2.0-150	140	23(21)	6.67	16.28
MBW 3.0-150	147	22(20)	7.35	28.20
MBW 3.0-400	140	21(20)	7.00	22.09

Ductility of the specimens were calculated from the ratio of the maximum displacement to the displacement at yield. The maximum displacement value (δ_f^-) was calculated using the Eq. (1), displacement at yield ($\delta\bar{y}$) using the Eq. (2), and ductility was calculated by Eq. (3).

$$\delta_f^- = \delta_f - \delta_i \quad (1)$$

$$\delta_y^- = \delta_y - \delta_i \quad (2)$$

$$\text{Ductility} = \delta_f^- / \delta_y^- \quad (3)$$

The area under the load-displacement curve gives the energy dissipation capacity of the specimen. The ductility and energy dissipation capacities of the specimens are given in Table 7.

The load-displacement curves of all specimens are shown in Fig. 10(a). Load-carrying capacities, stiffness, ductility, and energy dissipation capacities of the specimens are comparatively given in Figs. 10(b-c-d-e).

Table 7. Ductility and relative increase in ductility according to the reference specimen

Specimen	δ_i (mm)	δ_f (mm)	δ_y (mm)	δ_f^- (mm)	δ_y^- (mm)	Ductility	Ductility ratio (%)	Energy dissipation capacity (kJ)	Relative increase in energy dissipation capacity (%)
Reference	2	82.38	17	80.38	15	5.36	-	5.3	-
MBW 1.5-150	2	245.25	18	243.25	16	15.20	183.71	28.3	433.96
MBW 2.0-150	2	241.70	23	239.70	20	11.99	123.66	29.5	456.60
MBW 3.0-150	2	243.13	22	241.13	21	11.48	114.28	30.6	477.36
MBW 3.0-400	1	249.18	21	247.18	20	12.36	130.64	20.2	281.13

4. Conclusions

This study presents a strengthening method for both existing and future masonry brick walls through examination of 5 test specimens under diagonal static. Expanded steel plates were used for strengthening; thickness and bolt interval were examined as variables. In order to ensure the economic production of test specimens, no special materials were used. The materials used in the production of the specimens were easily available and common materials. Moreover, the examined strengthening method was also an easily applicable technique for a wide range of scenarios.

Based on the observations made during the tests and the analysis of the curves obtained by the experimental data, the following key findings were obtained:

- The un-strengthened reference specimen reached to collapse state immediately after reaching elastic load-carrying capacity due to the stress cracks that occurred under diagonal loading. This was expected behavior for a wall built from masonry brick which is a brittle material. For strengthened specimens, we observed that a great portion of the tensile stresses was covered by expanded steel plates and the walls exhibit composite behavior until the yield of the bolts.
- Ultimate strength at 245mm displacement of all strengthened walls increased in the range of 45%-94% compared to the reference specimen.

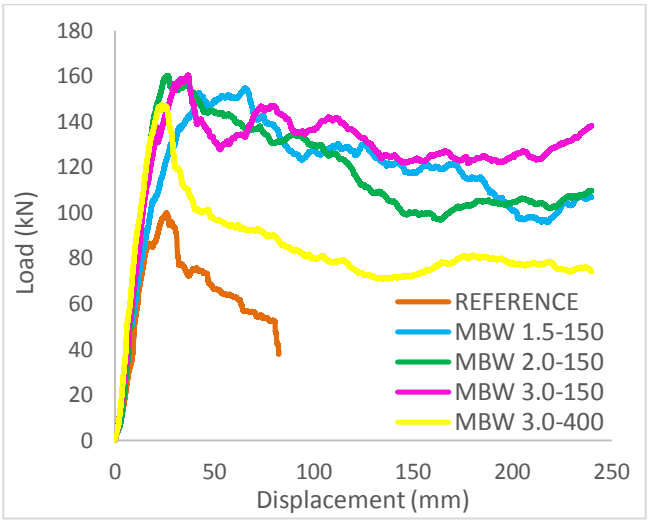

(a)

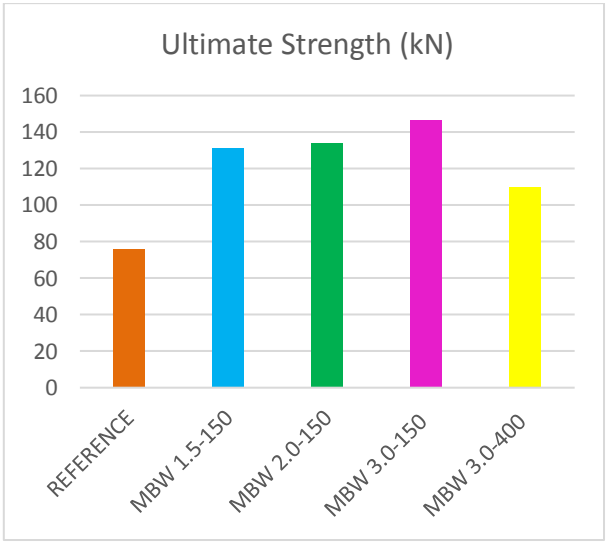

(b)

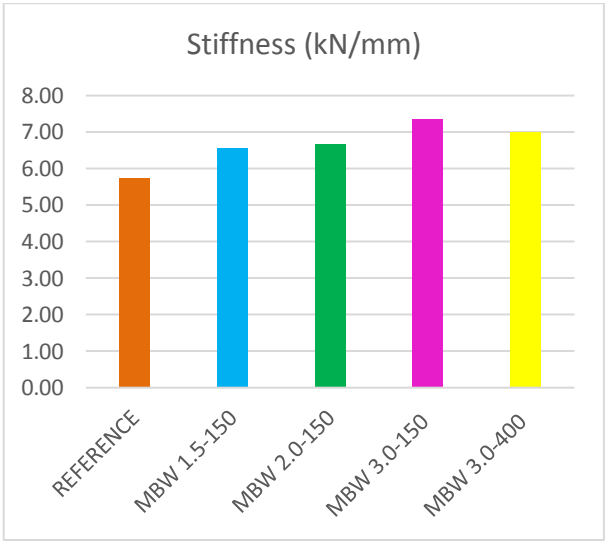

(c)

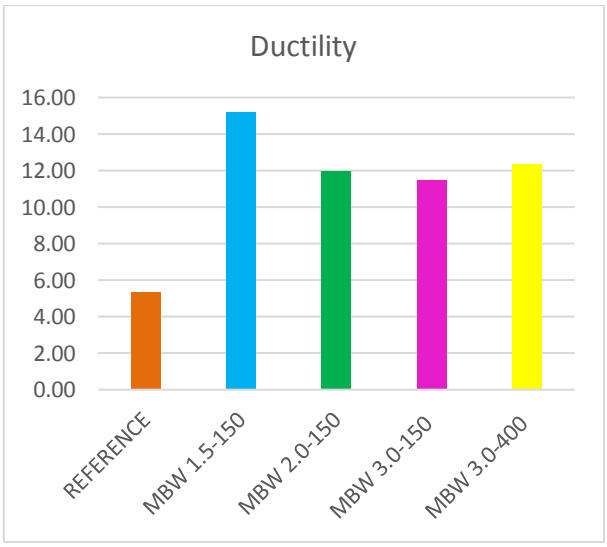

(d)

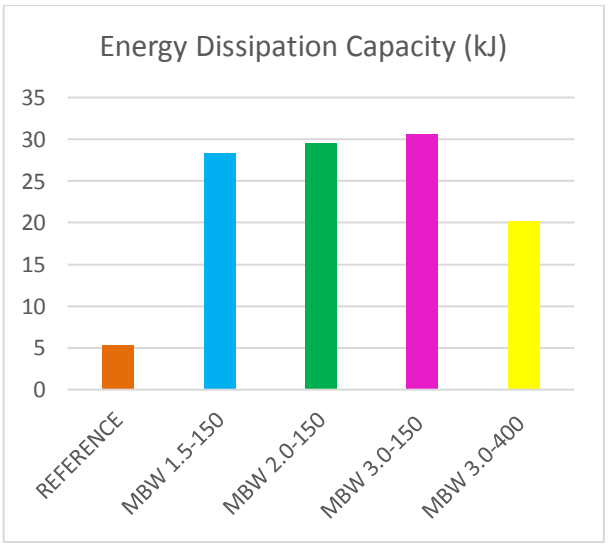

(e)

Fig. 10. Comparative presentation of the specimens' load-carrying capacities, stiffness, ductility, and energy dissipation capacities.

- All strengthened walls exhibited great plastic deformation after reaching the elastic load-carrying capacities and ductile behavior. The ductility of all strengthened specimens increased by 114-180% according to the reference. These results show that strengthening provides 2 to 3 times higher energy dissipation capacity for the energy generated by seismic effects like earthquakes compared to the reference specimen.
- As the plate thickness increased for the same bolt interval, no significant decrease in the load-carrying capacities was observed. In addition, the specimens maintained their integrity until the end of the tests. Accordingly, load-carrying capacities, energy dissipation capacities, ductility, and stiffness of the specimens strengthened with expanded steel plates significantly increased. As the plate thickness increased by 33% and 100% from 1.5 mm, load-carrying capacities were increased by 2% and 11.5%, respectively. It can be therefore argued that increasing plate thickness results in higher strength in masonry brick walls. However, since this increase is not too much, strengthening with 1.5 mm-thick steel plates was found to be the optimum thickness that provides sufficient strengthening performance. For the same plate thickness, even the steel plates fixed to the walls with high bolt intervals (MBW 3.0-400), the ductility increased by 130% compared to the reference specimen.
- Energy dissipation capacities of the strengthened specimens increased by 280-477% according to the reference specimen. The comparison of the specimens with the same plate thickness but different bolt intervals indicated that 65% of the energy dissipation capacity is provided by bolts. Strengthened specimens exhibited significantly higher energy dissipation capacities compared to the reference specimen. However, no significant changes were observed in the energy dissipation capacities of the specimens with the same bolt interval but steel plates of different thicknesses. We, therefore, concluded that the thickness of expanded steel plates does not has a significant impact on the mechanical properties of the walls; however, specimens with a bolt interval of 150 mm exhibited greater mechanical properties compared to the specimens with a bolt interval of 400 mm. Based on these findings we found that the impact of the bolt interval on the strength and behaviors of the members is higher than the impact of steel plate thickness.
- The ductility capacity of the reference wall specimen built with vertical-hole bricks, which are brittle construction materials, was significantly lower compared to the specimens strengthened with expanded steel plates. Compared to the reference specimen, strengthened specimens exhibited an average of 20% higher stiffness, 126% higher ductility, 410% higher energy dissipation capacity, and 72% higher load-carrying capacity.

According to the definition of the diagonal compression test in the ASTM E519, 1/8 of the side span of the neighboring edges to the diagonal loading point are fastened by loading shoes and other parts of the edges are set free during the loading. It is assumed that the wall sides contact with only 12.5% of the lateral-vertical peripheral tie system under the lateral loading and therefore, load applies to the wall through this contact area. In real cases, however, the contact area of the masonry walls with the lateral and vertical peripheral ties can be higher than the estimated value in the ASTM E519 due to the deformations under earthquake effect. The compression tests performed in the current study showed that the contact area of the wall sides with the frame which represents the lateral-vertical peripheral tie system was 60%.

Acknowledgements

The current study is based on the data of the Master's thesis of Ezatullah Ahmadzai, which was supervised by Asst. Prof. Zeynep Yaman and Asst. Prof. Alper Cumhur.

We would like to take the opportunity and thank Asst. Prof. M. Zeki Özyurt, Assoc. Prof. Elif Ağcakoca, M.Eng. Mohammad Saber Sadid, Fibreton Board Member M.Eng. Muhammed Maraşlı and FİBROBETON (https://www.fibrobeton.com.tr/) company for their contributions to this study.

Funding

The authors received no financial support for the research, authorship, and/or publication of this manuscript.

Conflict of Interest

The authors declared no potential conflicts of interest with respect to the research, authorship, and/or publication of this manuscript.

References

Abdulsalam B, Ali AH, ElSafty A, Elshafey N (2021). Behavior of GFRP strengthening masonry walls using glass fiber composite anchors. *Structures,* 29, 1352-1361.

Ağcakoca E, Bıyıklıoğlu E (2020). Experimentally and numerically investigating the performances of aramid fiber-reinforced steel beams under impact loadings. *Arabian Journal for Science and Engineering*, 45(10), 8053-8068.

Arslan ME, Ağcakoca E, Senturk M (2020). Effects of plaster thicknesses on cyclic behavior of infill walls with different materials. *Periodica Polytechnica Civil Engineering*, 63(3), 678-679.

ASTM E519/E519M-10 (2010). Standard Test Method for Diagonal Tension (shear) in Masonry Assemblages. American Society for Testing and Materials, West Conshohocken, Pennsylvania, U.S.A.

Ateş T (2013). İçten ve Dıştan Donatılı Püskürtme Beton ile Güçlendirilen Yığma Duvarların Düzlem Dışı Tekrarlı Yük Altındaki Davranışı. *PhD thesis,* Gazi University, Ankara, Turkey. (in Turkish)

Aydin AC, Yaman Z, Ağcakoca E, Kiliç M, Maali M, Dizaji AA (2020). CFRP effect on the buckling behavior of dented cylindrical shells. *International Journal of Steel Structures*, 20(2), 425-435.

Aykaç B, Özbek E, Babayani R, Baran M, Aykaç S (2017). Seismic strengthening of infill walls with perforated steel plates. *Engineering Structures*, 152, 168-179.

Babayani R (2012). Delikli Çelik Levhalarla Güçlendirilmiş Tuğla Duvarların Tersinir Tekrarlanır Yükler Altındaki Davranış ve Dayanımı, *MSc thesis*, Gazi University, Ankara, Turkey. (in Turkish)

Bahçekapılı S (2003). Mevcut betonarme yapıların depreme karşı güvenliğini belirleme yöntemleri, *M.Sc. Thesis*. Sakarya University, Sakarya, Turkey. (in Turkish)

Baran M, Aktaş M, Aykaç S (2014). Sıvanmış tuğla dolgu duvarların şerit beton/betonarme panellerle güçlendirilmesi. *Gazi Üniversitesi Mühendislik Mimarlık Fakültesi Dergisi,* 29(1), 23-33. (in Turkish)

Budak A, Uysal H, Aydın AC (2004). Kırsal yapıların deprem karşısındaki davranışı. *Atatürk Üniversitesi Ziraat Fakültesi Dergisi*, 35(3-4). (in Turkish)

Chen W, Yeh K, Hwang J, Lu C (2012). Out of-plane seismic behaviour and CFRP retrofitting of RC frames infilled with brick walls. *Engineering Structures*, N.T.U. Taiwan, 34, 213-224.

Cheng S, Yin S, Jing L (2020). Comparative experimental analysis on the in-plane shear performance of brick masonry walls strengthened with different fiber reinforced materials. *Construction and Building Materials*, 259, 120387.

Corradi M, Castori G, Borri A (2020). Repairing brickwork panels using titanium rods embedded in the mortar joints. *Engineering Structures*, 221, 111099.

Cumhur A (2016). Tuğla Dolgu Duvarların Genişletilmiş Çelik Levhalar ile Güçlendirilmesi. *PhD thesis*, Sakarya University, Sakarya, Turkey. (in Turkish)

Cumhur A, Altundal A, Kalkan I, Aykac S (2016). Behaviour of brick infill walls strengthened with expanded steel plates. *Bulletin of Earthquake Engineering*, 14(11), 3231-3258.

Ehsani MR, Saadatmanesh H, Velazquez-Dimas JI (1999). Behavior of retrofitted URM walls under simulated earthquake loading. *Journal of Composites for Construction*, 3(3), 134.

Erköseoğlu G (2014).Seismic Performance of Confined Masonry Construction. *MSc thesis,* Middle East Technical University, Ankara, Turkey.

FEMA 306 (1998). Evaluation of earthquake damaged concrete and masonry wall buildings. Federal Emergency Management Agency, Redwood City, California, U.S.A.

Güvenir E (2019). Yığma Yapıların Bölgesel Risk Dağılımının Belirlenmesi için Alternatif Hızlı Tarama Yönteminin Geliştirilmesi. *MSc thesis*, Hacettepe University, Ankara, Turkey. (in Turkish)

Hamdy G, Kamal O, Al-Hariri O, El-Salakawy T (2018). Plane and vaulted masonry elements strengthened by different techniques–Testing, numerical modeling and nonlinear analysis. *Journal of Building Engineering*, 15, 203-217.

Hejazi F, Noorzaei J, Ali AAA, Jaafar MS (2015). Seismic analysis of interlocking mortarless hollow block. *Challenge Journal of Structural Mechanics*, 1(1), 22-26.

İstegün B, Subaşı A, Çelebi E (2018). Sismik tekstil ile güçlendirilmiş düşey delikli yığma tuğla ve bims blokların üç noktalı kesme deneyi. *Academic Platform-Journal of Engineering and Science*, 7(2), 222-228. (in Turkish)

Johansson P, Geving S, Hagentoft CE, Jelle BP, Rognvik E, Kalagasidis AS, Time B (2014). Interior insulation retrofit of a historical brick wall using vacuum insulation panels: Hygrothermal numerical simulations and laboratory investigations. *Building and Environment*, 79, 31-45.

Kalali A, Kabir MZ (2012). Cyclic behaviour of perforated masonry walls strengthened with glass fiber reinforced polymers. *Scientia Iranica*, 19(2), 151-165.

Kalkan N (2008). Düzlem Dışı Tersinir Yüklenen Yığma Yapıların Donatılı Püskürtme Beton ile Güçlendirilmesi. *PhD thesis*, Gazi University, Ankara, Turkey. (in Turkish)

Karaton M, Çanakçı K (2021). Yığma duvarların mikro modellemesinde harcın çekme dayanımı ve kayma gerilmesi iletim katsayısının çözümler üzerindeki etkisinin incelenmesi. *Dicle Üniversitesi Mühendislik Fakültesi Mühendislik Dergisi*, 12(1), 175-185. (in Turkish)

Kaya F (2013). Yığma Yapıların Polipropilen Lifli Kuru Karışım Püskürtme Beton ile Güçlendirilmesi. *MSc thesis*, Süleyman Demirel University, Isparta, Turkey. (in Turkish)

Koç V (2016). Depreme maruz kalmış yığma ve kırsal yapı davranışlarının incelenerek yığma yapı yapımında dikkat edilmesi gereken kuralların derlenmesi. *Çanakkale Onsekiz Mart Üniversitesi Fen Bilimleri Enstitüsü Dergisi*, 2(1), 36-57. (in Turkish)

Korkmaz A (2014). Farklı yapısal malzeme özelliklerinin yığma yapı davranışına etkisi. *Nevşehir Bilim ve Teknoloji Dergisi*, 3(1), 69-78. (in Turkish)

Koutas L, Bousias SN, Triantafillou TC (2014). Seismic strengthening of masonry-infilled RC frames with TRM: Experimental study. *Journal of Composites for Construction*, 19(2).

Leeanansaksiri A, Panyakapo P, Ruangrassamee A (2018). Ascorbate, seismic capacity of masonry infilled RC frame strengthening with expanded metal ferrocement. *Engineering Structures*, 159, 110-127.

Maali M, Kılıç M, Yaman Z, Ağcakoca E, Aydın AC (2019). Buckling and post-buckling behavior of various dented cylindrical shells using CFRP strips subjected to uniform external pressure: Comparison of theoretical and experimental data. *Thin-Walled Structures*, 137, 29-39.

Marques AI, Ferreira JG, Candeias P, Veiga MDR (2022). Experimental evaluation of brick masonry walls strengthened with TRM (textile reinforced mortar) renders. *Buildings*, 12(6), 840.

Mezrea PE, Ispir M, Balci IA, Bal IE, Ilki A (2021). Diagonal tensile tests on historical brick masonry wallets strengthened with fabric reinforced cementitious mortar. *Structures*, 33, 935-946.

Mosallam AS (2007). Out-of-plane flexural behavior of unreinforced red brick walls strengthened with FRP composites. *Composites Part B: Engineering*, 38(5-6), 559-574.

Orulkaya H A (2019). Mevcut Yığma Yapıların Deprem Yüklerine Karşı Güçlendirilmesinde Püskürtme Beton Kullanımı. *MSc thesis,* Namık Kemal University, Tekirdağ, Turkey. (in Turkish)

Ozsayin B, Yilmaz E, Ispir M, Ozkaynak H, Yuksel E, Ilki A (2011). Characteristics of CFRP retrofitted hollow brick infill walls of reinforced concrete frames. *Construction and Building Materials*, 25(10), 4017-4024.

Özbek E, Can H (2012). Dolgu tuğla duvarların çelik profillerle güçlendirilmesi. *Gazi Üniversitesi, Mühendislik Mimarlık Fakültesi Dergisi*, 27(4), 921-929. (in Turkish)

Özbek E (2015). Delikli Çelik Levhalarla Güçlendirilmiş Tuğla Duvarların Çerçeve Davranışı Üzerindeki Etkisi. *PhD thesis,* Gazi University, Ankara, Turkey. (in Turkish)

Özbek E, Aykaç B, Can H, Kalkan İ, Aykaç S (2019). Delikli levhalarla güçlendirilmiş tuğla duvarların hesabı için öneriler. *Gazi Üniversitesi Mühendislik Mimarlık Fakültesi Dergisi*, 34(1), 1-16.

Özdemir H, Eren İ (2011). Bölme duvarının ve bölme duvar güçlendirilmesinin çerçeve davranışına etkisi. *İTÜDERGİSİ/d*, 8(6), 133-145. (in Turkish)

Özmen R (2018). Tuğla Duvarların Çelik Levha/Şerit Kullanılarak Kesme Davranışının Iyileştirilmesi. *MSc thesis,* Gazi University, Ankara, Turkey. (in Turkish)

Özyurt MZ, Mohammadi M, Cumhur A (2020). Genişletilmiş çelik levhalarla güçlendirilmiş blok tuğla duvarlarda bulon aralığının dayanım ve davranış üzerindeki etkisi. *Avrupa Bilim ve Teknoloji Dergisi*, 365-373. (in Turkish)

Rebelo F, Figueiredo A, Correia Lopes G, Ferreira TM, Vicente R (2021). Development of retrofitting solutions: remedial wall ties for masonry enclosure brick walls. *Buildings*, 11(1), 28.

Sevil T, Baran M, Canbay E (2010). Tuğla dolgu duvarların B/A çerçeveli yapıların davranışına etkilerinin incelenmesi; deneysel ve kuramsal çalışmalar. *International Journal of Engineering Research and Development*, 2(2), 35-42. (in Turkish)

Seydanlıoğlu M (2013). Delikli çelik levhalarla güçlendirilmiş tuğla duvarların tekdüze yükler altındaki davranışı. *MSc thesis*, Gazi University, Ankara, Turkey. (in Turkish)

Tekeli H, Akyürek O, Deniz M, Hersat E, Kara N, Tosun U (2014). Betonarme çerçevede dolgu duvarların hasır çelik donatılı sıva ile güçlendirilmesi. *BEU Journal of Science*, 3(2), 179-191. (in Turkish)

TS EN 772-1+A1 (2015). Methods of test for masonry units - Part 1: Determination of compressive strength. Turkish Standards Institution, Ankara, Türkiye.

Zhu H, Wan KT, Satekenova E, Zhang D, Leung CK, Kim J (2018). Development of lightweight strain hardening cementitious composite for structural retrofit and energy efficiency improvement of unreinforced masonry housings. *Construction and Building Materials*, 167, 791-812.

Challenge Journal of Structural Mechanics

Research Article

Numerical evaluation of reinforced concrete slabs with fixed support under impact load

Tolga Yılmaz [a,*], Hasan Selim Şengel [b]

[a] *Department of Civil Engineering, Konya Technical University, 42250 Konya, Turkey*
[b] *Department of Civil Engineering, Eskişehir Osmangazi University, 26040 Eskişehir, Turkey*

ABSTRACT

Reinforced concrete (RC) structural members may be subjected to impact load besides quasi-static load or other dynamic loads like earthquake and wind loads in their service periods. Many research emphasized that although impact load acts on structural members for a short time, it caused considerable damage to these members or even collapses the whole structure. Thus, it becomes crucial to consider and accurately evaluate the impact load effect in the design process. The present study intends to introduce a finite element model (FEM) verified with the test data for the accurate evaluation of load-deflection behavior and damage patterns of the fixed supported RC slabs exposed to impact load. First, a nonlinear FEM including strain-rate effect for both concrete and steel reinforcement, and crack visualization algorithm has been established by using LS-DYNA software. Then, the dynamic responses obtained by the present FEM have been compared with the experimental data presented in a previous study existing in the literature and it is found that the present FEM yields accurate results for the RC slab subjected to impact load and it can be safely used in the design process. In the second part of the study, using the verified FEM, the effects of applied input impact energy, the application point of impact load, and hammer geometry on the dynamic responses and failure characteristics of the RC slabs exposed to the impact loading were investigated and interpreted in detail.

ARTICLE INFO

Article history:
Received 28 July 2022
Revised 15 August 2022
Accepted 14 September 2022

Keywords:
Impact load
Reinforced concrete slab
Finite element method
LS-DYNA software

1. Introduction

Reinforced concrete (RC) slabs constitute functional areas in the structures. Besides, the main two duties of the RC slabs in the structural system are the transfer of the vertical loads to the beams, columns, load-bearing walls, and shear walls and the distribution of the lateral dynamic loads to vertical load-bearing structural members. The conventional design of the RC slab is performed by considering vertical loads such as dead and live loads and lateral earthquake and wind loads. However, recently, there is increasing concern about the design of the structural members against the low-velocity impact loads because there are many collision scenarios where velocities are up to 10 m/s in civil engineering. The rock fall, the vehicle crashes on bridge abutments, aircraft landing on the airport runway, ice or ship collisions to offshore structures, and collisions of the masses drifted by the tsunami, flood, and landslide to the structures can be examples of impact scenarios (Yilmaz et al. 2022). Unlike static loads, impact loads generate the inertia effects and the strain-rate effects. Furthermore, although the impact loads act on structural elements in a very short time, they may lead to remarkable damage to structural members or even an entire collapse of the structure. Fig. 1 depicts some examples of the failure of the structural element and the collapse of the structures due to impact load. The disregarding impact load effect at the design level may cause damage or collapse. Therefore, the dynamic responses and failure characteristics of the RC structural members subjected to impact load should be determined and considered in the design

* *Corresponding author*. Tel.: +90-332-205-1769 ; E-mail address: tyilmaz@ktun.edu.tr (T. Yılmaz)
ISSN: 2149-8024 / DOI: https://doi.org/10.20528/cjsmec.2022.03.005

stage. However, the design concept for the RC elements against the impact loads has not been fully manifested, and also design codes do not recommend an obvious evaluation to calculate dynamic responses and determine impact-induced failure modes of RC members. Besides, since there is no fully accepted standard test setup in the literature for performing impact experiments, the researchers developed various test setups such as pendulum and drop weight to examine impact behavior (Sha and Hao 2013; Shi et al. 2021; Yilmaz et al. 2019). In the literature, there are many studies focused on parameters that can be effective on the impact response of the RC slabs. In these studies, the parameters such as the concrete compressive strength (Anas et al 2022a; Said and Mouwainea 2022), the steel reinforcement ratio (Mizushima et al. 2022; Yılmaz et al. 2020), the steel reinforcement placement inclinations (Vijay et al. 2020), the corroded steel rebars (Daneshvar et al. 2021), the thickness of the slab (Hering et al. 2020), the pre-stress and post-tensioned applications (Al Rawi et al. 2020; Kumar et al. 2018; Thai and Kim 2017), the support layouts (Anil et al. 2015; Yılmaz et al. 2020), the opening existing in the slab (Yilmaz et al. 2022) were studied. There are also studies related to the behavior of the RC slab strengthened with Carbon, Glass, and Bazalt Fiber Reinforced Polymer (FRP) subjected to impact load in the literature (Anas et al. 2022b; Almusallam et al. 2015; Chen et al. 2020; Radnić et al. 2015; Soltani et al. 2020; Yılmaz et al. 2018). Furthermore, the effect of the FRP rebars on impact responses of the slabs was also studied (Mousavi and Shafei 2019; Sadraie et al. 2019). Based on the experimental research investigated in the scope of the literature review performed, it can be concluded that impact experiments require specific test setups and advanced measurement techniques. At this point, for realistic and rapid evaluation of the impact resistance of the RC structural elements, it is worthwhile to say that the numerical studies based on the finite element method (FEM) have an important role.

Fig. 1. Collapse of structure/structural member due to impact load (Do et al. 2018).

Consequently, the main motivation of this study is to establish a FEM verified with test data to predict the dynamic response and damage characteristics of the RC slabs with fixed support. First, the FEM of the RC slabs, which considers the strain-rate effect for the concrete and steel materials and the crack visualization algorithm, by using LS-DYNA software has been introduced. The presented model is calibrated with the results obtained from an experimental study presented by Kumar et al. (2018). After the good agreement between test and numerical results was demonstrated, using the present model, a parametric study was carried out. In the parametric study, the effects of applied input impact energy, the application point of impact load, and hammer geometry on the impact behavior of the RC slabs are investigated and interpreted in detail.

2. Details of the Experiment used for Verification of Numerical Analysis

The comprehensive experimental study presented by Kumar et al. (2018) in which the conventional reinforced concrete (RC) and prestressed concrete plates subjected to impact force is investigated has been utilized for verification of the presented numerical model. In the experimental program, two RC slabs with dimensions of 800x800x100 mm. The concrete compressive strength after 28 days from the cast was determined as 48.4 MPa. The maximum size of coarse aggregate used for the manufacture of the RC slabs was 10 mm. Besides, natural sand was used as fine aggregate. The Ordinary Portland Cement of 43 grade has been used for the concrete mix. The ratio of concrete mix ingredients was 1:1.74:1.68 (cement/fine aggregate/coarse aggregate). The RC slab was designed using deformed steel rebars with high yield strength. The diameter of the steel bars was 8 mm. The steel rebars were spaced at 140 mm in the two directions of the RC slab. The average yield strength of the rebars was determined as 609 MPa with a uniaxial tension test. In the experimental program conducted by Kumar et al (2018), the RC slabs tested under impact load had fixed boundary conditions. The rotations and translations of plate edges were constrained. Impact energy has been applied to the center of the RC slabs by dropping freely a steel hammer. The weight of the hammer was 242.85 kg. The geometric shape of the hammer was a cylinder with a diameter of 100 mm. The input impact energies transferred to two RC slabs are 1.190 kJ and 2.380 kJ, which corresponds hammer drop heights of

500 mm and 1000 mm, respectively. The dimensions and rebar arrangement of the RC slabs and the setup used for carrying out experiments are illustrated in Fig. 2(a) and Fig. 2(b), respectively. The time histories of the impact load acting on the RC slabs and the displacements measured from the center point of the RC slabs on the tension side, recorded during tests, have been used to verify the presented FEM of the RC slabs. Furthermore, impact load-induced crack on the tension side of the two RC slabs has been compared to damage distributions obtained by the numerical model.

3. Details of the Presented FEM Model

In the study, LS-DYNA software is utilized for the generation of the FEM of the RC slabs with fixed support under the impact load. (LS-DYNA Keyword user's manual 2018). LS-DYNA could conduct nonlinear dynamic analysis using an explicit solver. Furthermore, LS-DYNA includes several concrete material models such as Winfrith Model, Continuous Surface Cap Model, and Concrete Damage Model (MAT_072R3) to model concrete material exposed to impulsive loading. Thus, LS-DYNA software is commonly preferred by structural engineers to evaluate the dynamic responses and failure characteristics of structural members exposed to blast and impact loads (Li et al. 2017; Chen et al. 2015, 2020; Do et al. 2018a, 2018b). The presented FEM is composed of four main parts: the RC slab, steel reinforcement, the rigid hammer, and rigid support. An 8-node hexahedron solid element with tri-linear shape functions, using one-point integration plus viscous hourglass control is used for modeling the concrete slab, hammer, and support while steel rebars were modeled by Hughes-Liu beam element with 2×2 Gauss quadrature integration.

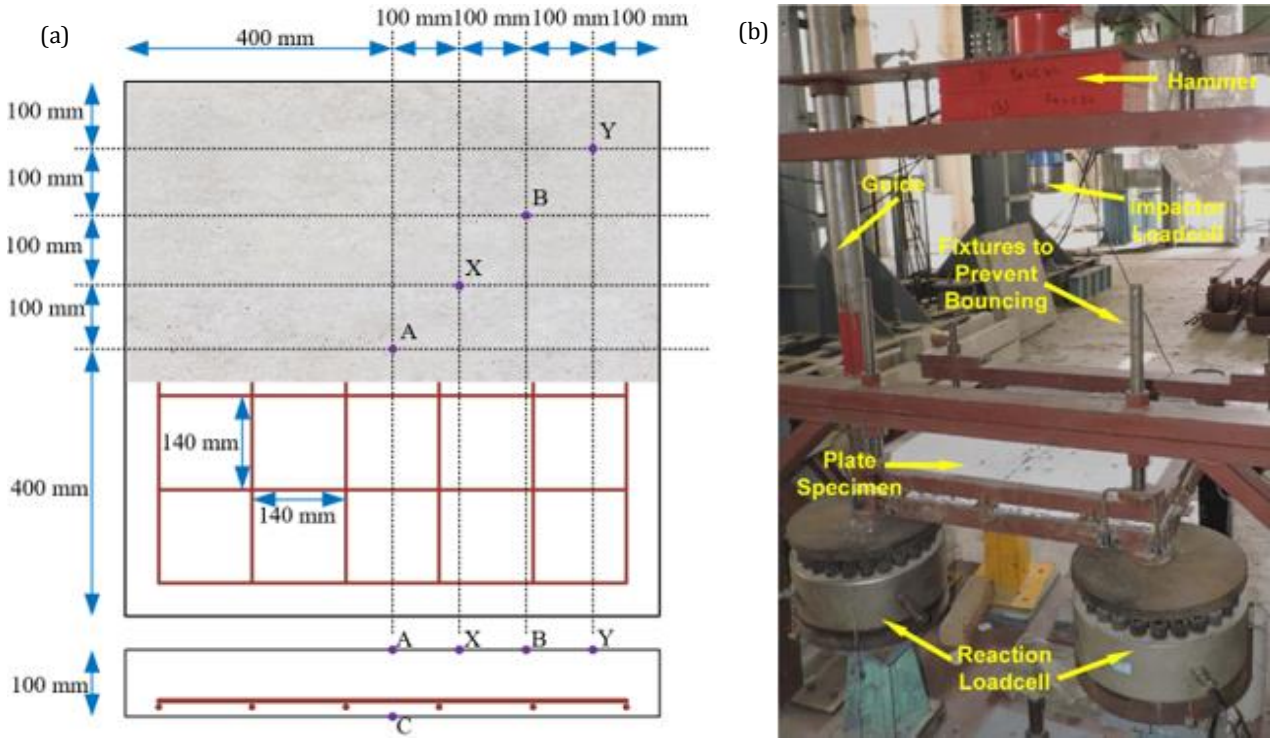

Fig. 2. (a) The geometric dimensions and rebar details of the RC slabs; (b) Test setup.

In the scope of the present FEM, it has been assumed the contact behavior between concrete and steel reinforcements was perfectly bonded using the keyword named *CONSTRAINED_LAGRANGE_IN_SOLID. It is determined from the mesh convergence study that when concrete element size is assumed as 20 mm, the results of numerical analysis convergence to those obtained by experiments. Besides, the mesh study indicates that further refinement has no considerable effect on the results although it causes more computational time. During the collision, firstly, the curved surface of the rigid hammer contacts the concrete. Thus, to represent actual behavior and calculate impact forces compatible with that of experiments, mesh refinement is required for the hammer. Mesh size has been assumed as 10 mm for the rigid hammer. It should be emphasized here that the mesh size values which are chosen for the RC slab and the rigid hammer in the present FEM have been commonly used in previous studies for the RC slabs and the hammers, which are similar sizes (Şengel et al. 2022; Li et al. 2019, 2020).

The impact load was applied to the RC Slabs by defining the initial impact velocity to the hammer utilizing *INITIAL_VELOCITY_GENERATION keyword. In the experiments used for verification, impact velocities are given as 3.130 m/s and 4.427 m/s for drop heights of 500 mm and 1000 mm, respectively. These values have been assigned to the rigid hammer to apply impact forces to the RC slabs. Fig. 3 illustrates the FEM of the RC slab, steel reinforcement, rigid support, and rigid hammer.

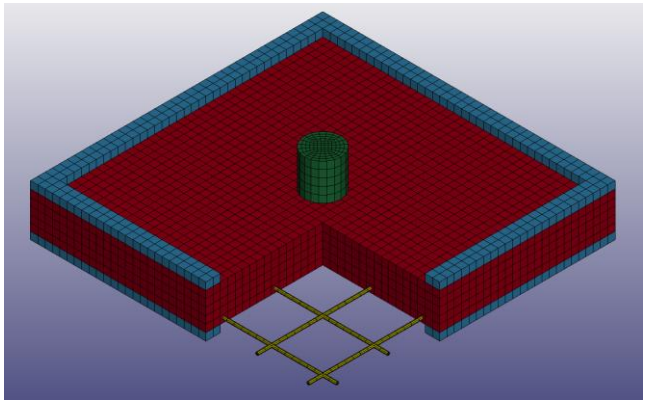

Fig. 3. The FEM of the rigid hammer, steel reinforcement, the RC slab, and the rigid support.

In the present FEM, concrete was modeled with the Winfrith material model (MAT_084-085). Winfrith concrete model was introduced for the nuclear industry to perform finite element analysis for the evaluation of the local and global response of the RC structures subjected to impact and blast loading and then implemented in LS-DYNA. This plasticity model is based on the shear failure surface presented by Ottosen (1977):

$$Y(I_1,J_2,J_3) = aJ_2 + \xi\sqrt{J_2} + bI_1 - 1 \tag{1}$$

$$\xi = \begin{cases} k_1 \cos\left[\frac{1}{3}\cos^{-1}(k_2\cos(3\theta))\right] & \cos(3\theta) \geq 0 \\ k_1 \cos\left[\frac{\pi}{3} - \frac{1}{3}\cos^{-1}(-k_2\cos(3\theta))\right] & \cos(3\theta) \leq 0 \end{cases} \tag{2}$$

where I_1 is the first invariant of stress tensor representing volumetric response, J_2 and J_3 are the second and third invariants of the deviatoric stress tensor. a, b, k_1 and k_2 are the functions of $T=f_t/f_c$ and these parameters can be determined from uniaxial, biaxial, and triaxial compression and uniaxial tension tests. f_t and f_c refer to tensile and compressive strengths of concrete, respectively. The meridional shape parameters a and b can be expressed using T and three non-dimensional constants, which are α=1.16, β=0.5907445, and γ=-0.613724, as follows (Maazoun et al. 2022):

$$b = \frac{1+T\alpha\frac{\gamma}{3}-\alpha^2\frac{\gamma}{3}-\frac{\alpha}{T}}{\alpha^2\frac{\beta}{3}-3\alpha-T\alpha\frac{\beta}{3}} \tag{3}$$

$$a = \beta b + \gamma \tag{4}$$

The k_1 and k_2 that defines the shape of the shear failure surface can be calculated as follows (Maazoun et al. 2022):

$$k_2 = \cos\left[3\tan^{-1}\left(\frac{1}{\sqrt{3}} - \frac{2h}{e\sqrt{3}}\right)\right] \tag{5}$$

$$k_1 = \frac{e}{\cos\left[\frac{1}{3}\cos^{-1}(k_2)\right]} \tag{6}$$

The e and h constants that take place in Eqs. (5) and (6) can be expressed as follows:

$$e = \frac{\sqrt{3}}{T}\left(1 - bT - T^2\frac{a}{3}\right) \tag{7}$$

$$h = \frac{3+3b-a}{\sqrt{3}} \tag{8}$$

Fig. 4(a) depicts the bi-linear concrete material model representing the uniaxial stress-strain relationship. The compression behavior of concrete was represented via the elastoplastic curve that has ultimate strain (ε_{cu}). While tension behavior was characterized as linear up to the peak tensile stress corresponding to cracking strain (ε_{cr}), the post-peak response was defined as a linear decrease. The ultimate tensile strain (ε_{tu}) was calculated based on the function of the concrete fracture energy (Thai and Kim 2014). The Winfrith model is capable of representing cracking, crushing, and shear retention behavior considering crack width and aggregate size and it is applied with eight-node continuum elements with a single integration point. The Winfrith model can capture crack generation, and the determination of crack is based on the theory presented by Wittman et al. (1988). When concrete tensile strength is exceeded, the crack occurs and propagates by generating a gap whose size is defined by crack width. The linear strain softening response can be characterized as in Fig. 4(b) with fracture energy (G_f), tensile strength (f_t), and crack width (w) (Maazoun et al. 2022).

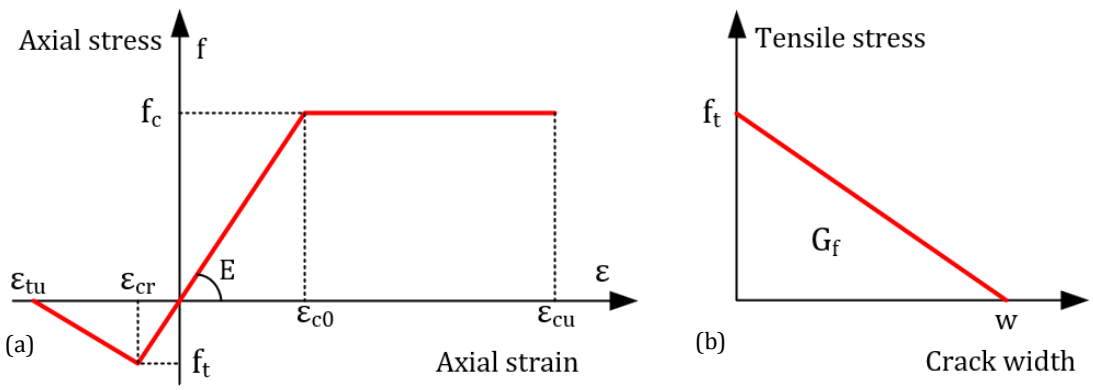

Fig. 4. (a) Stress-strain behavior of concrete; (b) Strain softening response.

The mass density (R0) 2400 kg/m^3, tangent modulus (TM) 34000 MPa, Poisson's ratio (PR) 0.20, uniaxial compressive strength (UCS) 48.4 MPa, uniaxial tensile strength (UTS) and aggregate size (ASIZE) 10 mm are required input parameters for definition Winfrith concrete model, and the rest of parameters are calculated by LS-DYNA based on these values. In the numerical analysis, the tensile strength of concrete has been neglected, however, a small value is assigned to the tensile strength for the establishment of the material model. The steel reinforcements are defined with the elastic-plastic material model. The material card ∗MAT_PIECEWISE_LINEAR_PLASTICITY (MAT_24) allows users to define an arbitrary stress-strain curve for the representation of nonlinear behavior. The yield strength and elastic modulus belonging to steel material have been defined as 609 MPa and 200000 MPa, respectively. Poisson's ratio and density were 0.3 and 7850 kg/m^3, respectively.

Impulsive loading such as impact and blast exhibits different behavior than static loading and it leads to an increase in the compressive and tensile strength of materials. The increase of material strength under high rate loading is known as the strain-rate effect (Hao et al. 2013; Sha and Hao 2013; Hao and Hao 2014; Malvar and Crawford 1998; Do et al. 2018a; CEB Code 1990). There exist many studies focused on the effect of the strain rate on the material properties, and accordingly the results of the finite element simulations in the literature. These studies unveil that the strain-rate effect should be regarded in the material model for the correct prediction of the dynamic responses and failure characteristics of structural elements exposed the impulsive loads (Li and Hao 2013; Li and Hao 2014; Chen et al. 2015; Jiang and Chorzepa 2015; Do et al. 2018a, 2018b). The strain rate effect is considered by multiplying the tensile and compression strengths belonging to steel and concrete material with a dynamic increase factor (DIF). The DIF refers to a ratio of dynamic strength to static strength and is defined for a wide spectrum of strain-rate values. A considerable number of empirical formulations have been developed to characterize the strain rate effect for concrete and steel materials in the literature (CEB 1990; Malvar 1998; Malvar and Ross 1998; Malvar and Crawford 1998; Fan et al. 2011; Hao and Hao 2014). The strain-rate effect can be included in the Winfrith concrete model via the option existing in its material card. For considered strain rate, the tensile (DIF_t) and compression (DIF_c) DIFs belonging to concrete, taking place in the Winfrith model, have been given in Eqs. (9) and (10) (Thai and Kim 2014).

$$\mathrm{DIF_t} = \left(\frac{\dot{\varepsilon}}{\dot{\varepsilon}_{0T}}\right)^{1.016\delta} \text{ and } \mathrm{DIF_c} = \left(\frac{\dot{\varepsilon}}{\dot{\varepsilon}_{0C}}\right)^{1.026\alpha} \quad \text{for } \dot{\varepsilon} < 30 \text{ s}^{-1} \tag{9}$$

$$\mathrm{DIF_t} = \eta\dot{\varepsilon}^{1/3} \text{ and } \mathrm{DIF_c} = \gamma\dot{\varepsilon}^{1/3} \text{ for } \dot{\varepsilon} > 30 \text{ s}^{-1} \tag{10}$$

The terms taking place in Eqs. (9) and (10) can be defined as follows:

$$\delta = \frac{1}{10+0.5f_c} \tag{11}$$

$$\alpha = \frac{1}{5+0.75f_c} \tag{12}$$

$$\log_{10}\eta = 6.933\delta - 0.492 \tag{13}$$

$$\log_{10}\gamma = 6.156\alpha - 0.49 \tag{14}$$

$$\dot{\varepsilon}_{0T} = 30x10^{-6} \text{ s}^{-1} \tag{15}$$

$$\dot{\varepsilon}_{0C} = 3x10^{-6} \text{ s}^{-1} \tag{16}$$

where f_c is the concrete cube strength and should be defined in a unit of MPa. Furthermore, the enhancement of elastic modulus with the effect of strain rate has (DIF_E) been considered in the Winfrith material model as follows:

$$\mathrm{DIF_E} = 0.5\left[\left(\frac{\dot{\varepsilon}}{\dot{\varepsilon}_{0T}}\right)^{0.016} + \left(\frac{\dot{\varepsilon}}{\dot{\varepsilon}_{0C}}\right)^{0.026}\right] \tag{17}$$

Besides, ∗MAT_PIECEWISE_LINEAR_PLASTICITY (MAT_24) allows users to define the strain rate effect. The tensile and compression DIF relations of steel material have been defined according to equations proposed by Malvar (1998). For considered strain rate $\dot{\varepsilon}$, both tensile and compressive DIFs of steel material (DIF_{St}) can be calculated with Eq. (18).

$$\mathrm{DIF_{St}} = \left(\frac{\dot{\varepsilon}}{10^{-4}}\right)^{\mu} \tag{18}$$

The μ coefficient existing in Eq. (18) can be written as based on the steel yield strength (f_y) as follows:

$$\mu = 0.074 - \frac{0.04f_y}{414} \tag{19}$$

In the FEM presented, the rigid material behavior has been assigned to the steel hammer and steel support. Also, all translational and rotational movements of rigid support were restrained. The RC slab was located between steel supports for clamping similar to that of experiments. The penalty-based ∗AUTOMATIC_SURFACE_TO_SURFACE contact algorithm was used for modeling the both contact between the rigid support and the RC slab and the contact between the rigid hammer and the RC slab. While for the contact between the rigid hammer and the RC slab, the contact stiffness scale factors were taken as 0.15, the contact stiffness scale factors were defined as 1.0 for the contact between the rigid support and the RC slab. Besides, the ∗AUTOMATIC_NODES_ TO_SURFACE contact algorithm was used for modeling contact between hammer and steel reinforcements. A full bond between concrete and rebars was generated with ∗CONSTRAINED_LAGRANGE_IN_SOLID algorithm.

4. Parametric Study

In the scope of the parametric study, the FEM of the eight RC slabs with fixed support has been generated to investigate the effects of input impact energy, the location of the point at which impact load is applied, and the hammer geometry on the dynamic responses and failure characteristics of the RC slabs. Table 1 shows RC slab specimens used for the parametric study and the investigated parameters in the parametric study.

Table 1. RC slab test specimens and the investigated parameters

RC slabs	Drop height	Impact load application point	Hammer geometry
S1	500 mm	Center	Cylinder
S2	500 mm	Center	Hemisphere
S3	500 mm	Diagonal	Cylinder
S4	500 mm	Diagonal	Hemisphere
S5	1000 mm	Center	Cylinder
S6	1000 mm	Center	Hemisphere
S7	1000 mm	Diagonal	Cylinder
S8	1000 mm	Diagonal	Hemisphere

S1 and S5 test specimens are FEM of two RC slabs that have been tested in the experimental study conducted by Kumar et al. (2018), and they are used for verification of the present FEM. The geometric dimensions and reinforcement details were identical for these slabs and they had been presented in Fig. 2(a). The rest of the test specimens in the parametric study have also the same geometric dimensions and reinforcement details. Similar to the experimental program conducted by Kumar et al. (2018), input impact energies of 1.190 kJ and 2.380 kJ have been applied to the center of S1 and S5 (Point A in Fig. 2(a)), respectively, by assigning impact velocities of 3.130 m/s and 4.427 m/s to steel hammer with the weight of 242.85 kg. These two input impact energies have been assumed as one of the variables of the parametric study. However, the weight of the steel hammer has been kept constant for all RC slabs in numerical analysis. The second variable of the parametric study is the application point of the impact load. Two different impact load application points exist in numerical analysis. One is the center of the RC slabs (Point A in Fig. 2(a)) and another is the point at one-four of the diagonal line of the RC slabs (Point B in Fig. 2(b)). The last variable investigated in the parametric study is the geometric shape of the steel hammer. A cylinder hammer with a diameter of 100 mm which is taken place experimental program performed by Kumar et al. (2018) and a hemispheric hammer with a radius of 50 mm are two different hammer geometries that are included in the present FEM to investigate the effect of impactor geometry. It should be noted here that these two hammer geometries have the same weight of 242.85 kg. In the parametric analysis, under the effect of the applied input impact energy to the RC slabs, time-histories of the impact loads that act on RC slabs, and the displacements measured at the center of the RC slab were calculated. Besides, von-Misses stress distributions and crack patterns which have been obtained by the numerical analysis were presented. According to applied input impact energy, the impact forces, displacements, and load-displacement curves have been presented in Fig. 5. Besides, Table 2 summarizes the dynamic responses including peak impact forces, maximum and residual displacements, and the energy absorption capacities calculated from the area under the impact load versus displacement curves. Furthermore, Table 3 shows the comparison of the numerical results of S1 and S5 RC slabs and the experimental results presented in the study of Kumar et al. (2018).

Table 2. Dynamic responses obtained from numerical analysis

RC slabs	Peak impact forces (kN)	Max displacements (mm)	Residual displacements (mm)	Energy absorption capacities (J)
S1	273.26	10.58	5.51	1292.67
S2	99.41	12.74	8.64	1062.51
S3	264.03	2.50	0.70	398.56
S4	97.57	0.89	-0.23	76.06
S5	361.77	18.99	14.00	2640.56
S6	123.10	25.74	19.34	2195.39
S7	355.88	3.48	1.66	657.73
S8	119.93	0.93	-0.21	89.27

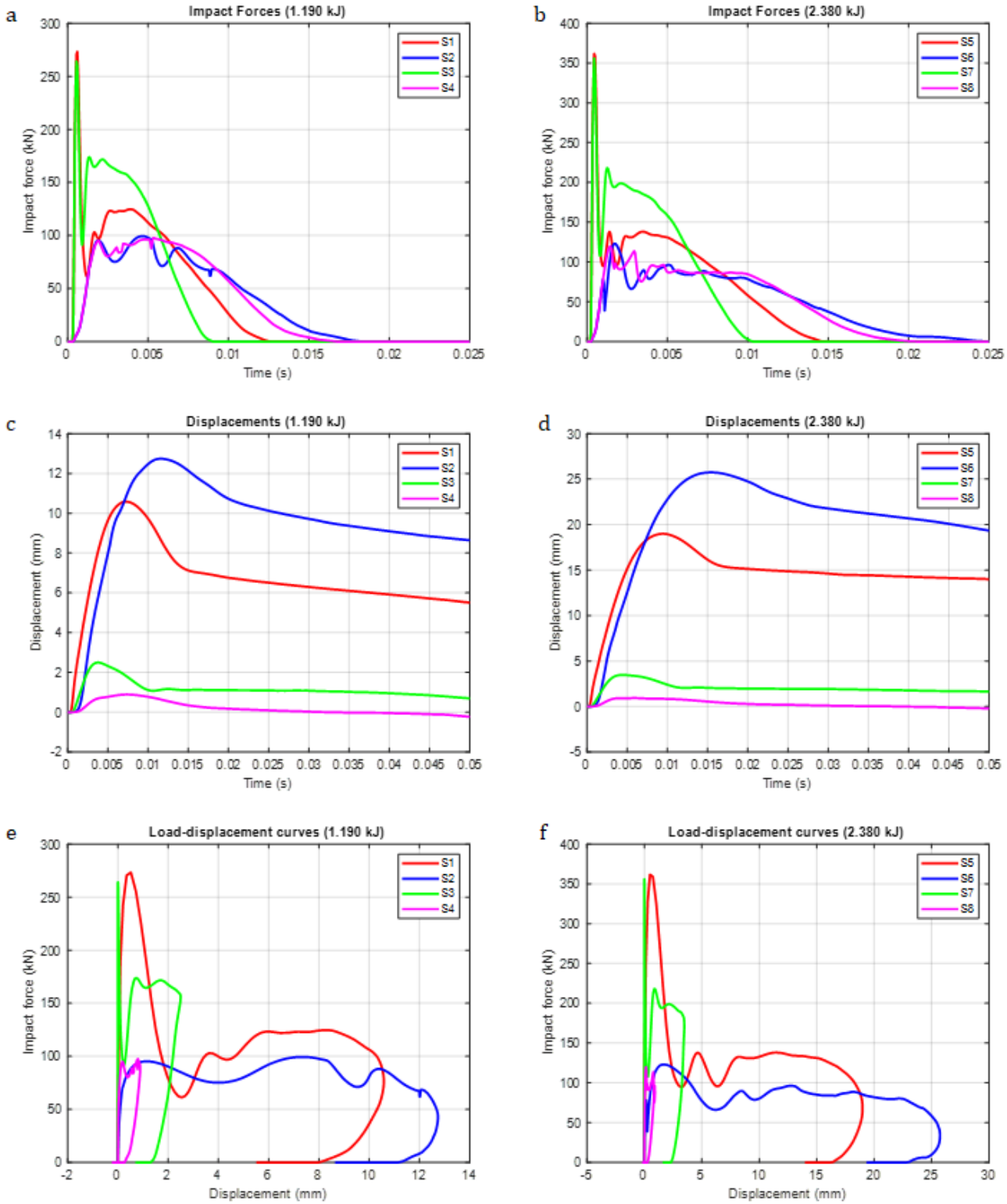

Fig. 5. (a) - (b) Time histories of impact forces; (c) - (d) Time histories of displacements; (e) - (f) Load-displacement curves.

Table 3. Comparison of numerical results and experimental results (Kumar et al. 2018).

RC slabs	Peak impact forces (kN)			Maximum mid-span displacements (mm)			Residual Displacements (mm)		
	Num.	Exp.	Ratio	Num.	Exp.	Ratio	Num.	Exp.	Ratio
S1	273.26	259.10	5%	10.58	9.76	8%	5.51	3.31	66%
S5	361.77	355.46	2%	18.99	19.97	5%	14.00	12.14	15%

When the results in Table 3 are examined, it is found that there is pretty good accordance between numerical and experimental results in terms of impact forces and maximum mid-span displacements. However, for residual displacements, there are up to 66% differences between numerical and experimental results. It should be also emphasized that when applied input impact energy is increased, this difference has become remarkably lower. Authors consider that alongside the good accordance between numerical and experimental results, which were observed for impact forces and maximum displacements, the differences in residual displacements are also acceptable for impact simulations where loading occurs in a very short time. Many factors such as the non-homogeneous nature of concrete, rigors on accurate estimation of strain-rate effect and damping of materials, and exact support conditions in numerical analysis contrary to real support conditions that have included many frictional movements, the complex interaction between contact areas during the collision may lead to differences numerical and experimental results. Furthermore, similar acceptable differences between numerical and experimental residual displacements have been observed in the comprehensive numerical studies in the literature (Othman and Marzouk 2014; Huang et al. 2021; Liu et al. 2020; Batarlar and Saatci 2022). Eventually, it is thought that the presented FEM could be safely used for impact responses of the RC slabs with fixed support.

When the numerical results are examined, it is found that for both applied input impact energy the application point of impact load has a quite negligible effect on the maximum impact forces. When impact load is applied to Point B instead of Point A, the decrease in maximum impact load is under 3.3%. However, the application of impact load on Point B instead of A decreased the mid-span maximum and residual displacements, and energy absorption capacities considerably, especially when high impact energy is applied. For high input impact energy, shifting impact load to Point B, decreased the mid-span maximum and residual displacements, and energy absorption capacities 28 times, 92 times, and 25 times, respectively. Eccentric impact loading has led to less maximum and residual displacement on account of the restraint provided by the supporting (Anas et al. 2022c).

Numerical results show that the cylinder hammer produces the greater maximum impact forces, however, impact duration is shorter. A similar tendency has been reported in the previous comprehensive analytical study (Li et al. 2019). When results are examined, it is determined that the cylinder hammer led to approximately 2.7-3.0 times greater impact forces. However, mid-span maximum and residual displacement increased with the use of the hemispheric hammer. As a result of impact load and displacement tendencies, the energy absorption of the RC slabs subjected impact load applied using a cylinder hammer is greater and they experience more ductile behavior. Furthermore, there is an important issue related to maximum and residual displacements that should be explained. As above mentioned, the impact load applied with a hemispheric hammer cause higher displacement values, however, this is true when the displacement measurement has been taken from near the collision region which is the surrounding area of the impact load application point (Li et al. 2019). Otherwise, this behavior tendency becomes reverse and the cylinder hammer generates higher displacements. For example, when the impact load is applied to point B, if the maximum and residual displacements at mid-span, which is relatively far from impact point B, are examined, it is seen that S3 and S7 exhibit greater displacement than S4 and S8, respectively. For a better understanding of this behavior tendency, the maximum displacement measurements taken from four points on the diagonal of the S5 and S6 test specimens have been presented in Fig. 6. Impact loads had been applied to the slab center of these specimens. When Fig. 6 is examined, it is found while in the collision zone, the hemisphere hammer generates higher displacement values, but away from this region cylinder hammer causes maximum displacements. Hemisphere hammer leads to localize damage with its penetrative effect and correspondingly increased the displacements that occurred in the collision zone. Away from the collision zone, the local damage effect of the hemisphere hammer remarkable decrease, cylinder hammer which produces greater impact forces becomes more effective on displacements.

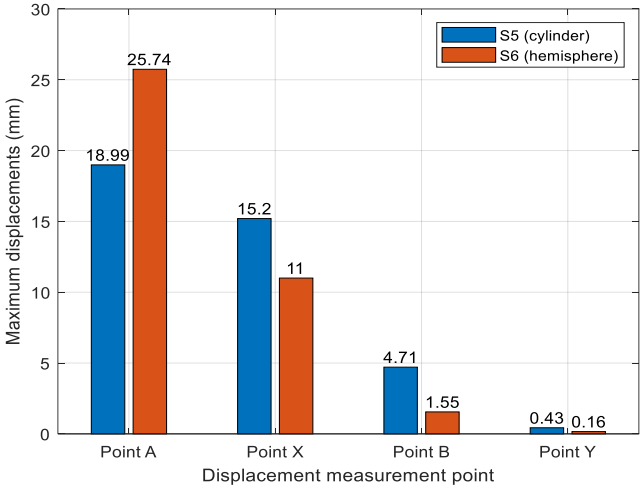

Fig. 6. The comparison of the maximum displacements measured at the diagonal of the S5 and S6.

When impact energy applied to the RC slabs is increased, the force transferred to the slabs and damages occurred also increased, and thus, the maximum and residual displacements, and energy absorption capacities increased. With the increase of input impact energy, while maximum impact forces increase up to 35%, maximum and residual displacements increased up to 2 and 2.5 times, respectively. Besides, it is found that the energy absorption capacities increased 1.2-2.1 times with the effect of higher input impact energy applied. Fig. 7 illustrates von-Misses stress distributions and crack patterns obtained from numerical analysis. It is seen from Fig. 7 that damage is concentrated more collision region. Besides, while cylinder hammers cause more damage, the hemisphere hammer leads to penetrative local damaged. The increase of impact energy applied to slabs remarkably increased the damages.

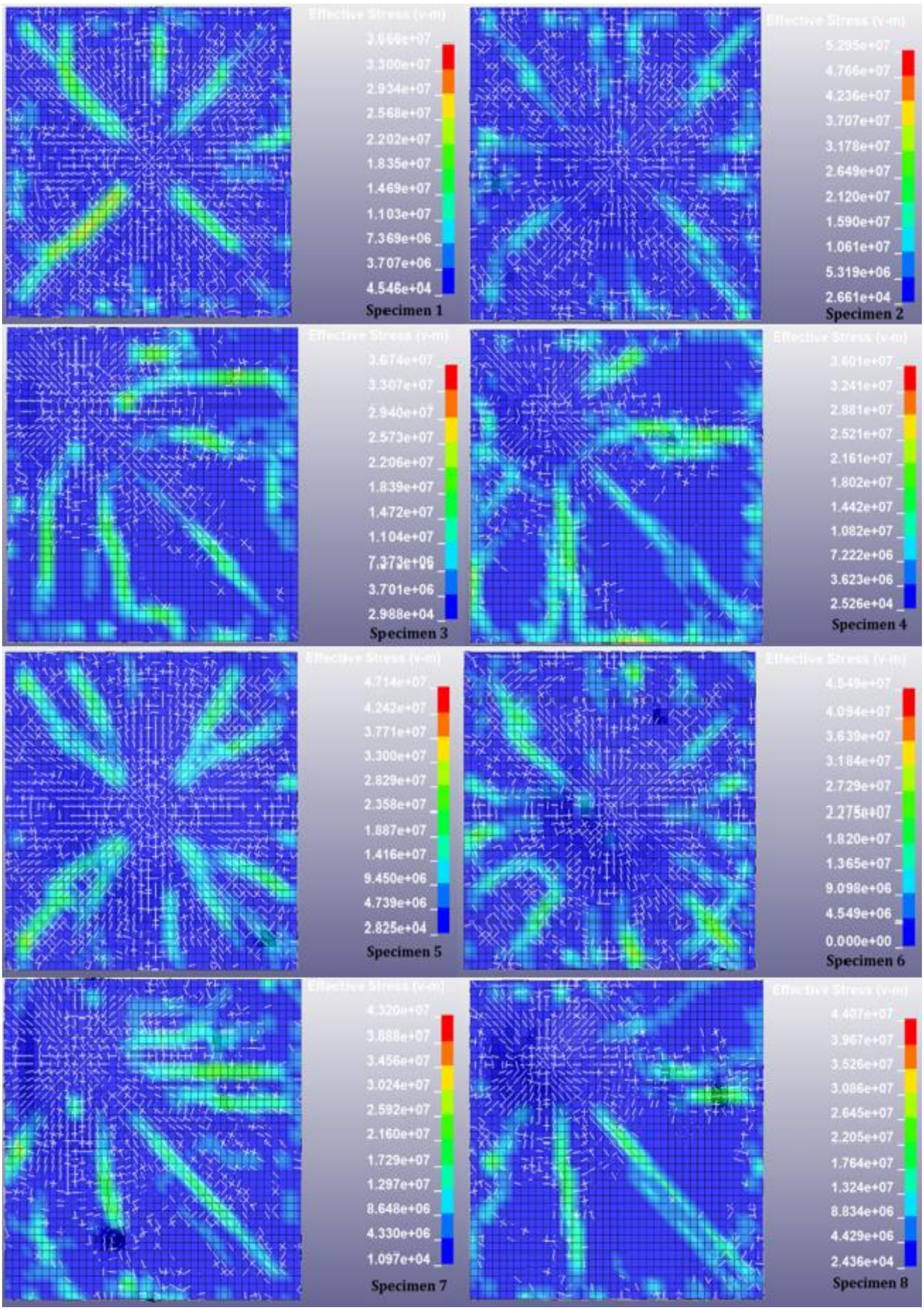

Fig. 7. von-Misses stress distributions and crack patterns obtained numerical analysis.

5. Conclusion

The present study introduces a detailed FEM including strain-rate effect, and crack visualization algorithm for evaluation of the RC slabs with fixed support under the effect of impact load. The proposed FEM has been verified with experimental results existing in a study previously presented in the literature. Then, a parametric study where the effects of impact energy applied, the impact load application point, and the hammer geometry on the dynamic responses and failure characteristics of the RC slabs are investigated. The results obtained from the parametric analysis are summarized below:

- The application point of impact load has a quite negligible effect on the maximum impact forces. However, instead of slab center, eccentric impact loading generates less mid-span maximum and residual displacements and energy absorption capacities.
- Impact loading with a cylinder hammer causes greater impact forces however impact duration becomes short. The cylinder hammer led to approximately 2.7-3.0 times greater impact forces. When the displacement measurement has been taken from the near field of the impact load application point, the hemispheric hammer causes higher displacement values due to localize damage thanks to its penetrative behavior. However, for the displacement measurements away from the collision zone, it is observed that the cylinder hammer yields higher displacement responses.
- With the increase of impact energy applied, the maximum impact forces increase up to 35%, while maximum and residual displacements, and the energy absorption capacities up to 2, 2.5, and 2.1 times, respectively.
- The authors also consider that for the future studies present FEM could be improved with the implementation of the bond-slip model instead of the assumption of the perfect bond between the concrete and reinforcement.

Acknowledgements

None declared.

Funding

The authors received no financial support for the research, authorship, and/or publication of this manuscript.

Conflict of Interest

The authors declared no potential conflicts of interest with respect to the research, authorship, and/or publication of this manuscript.

References

Al Rawi Y, Temsah Y, Baalbaki O, Jahami A, Darwiche M (2020). Experimental investigation on the effect of impact loading on behavior of post- tensioned concrete slabs. *Journal of Building Engineering,* 31, 101207.

Almusallam T, Al-Salloum Y, Alsayed S, Iqbal R, Abbas H (2015). Effect of CFRP strengthening on the response of RC slabs to hard projectile impact. *Nuclear Engineering and Design*, 286, 211–226.

Anas SM, Alam M, Umair M (2022a). Effect of design strength parameters of conventional two-way singly reinforced concrete slab under concentric impact loading. *Materials Today: Proceedings,* 62, 2038–2045.

Anas SM, Alam M, Tahzeeb R (2022b). Impact response prediction of square RC slab of normal strength concrete strengthened with (1) laminates of (i) mild-steel and (ii) C-FRP, and (2) strips of C-FRP under falling-weight load. *Materials Today: Proceedings*, In Press.

Anas SM, Alam M, Shariq M (2022c). Damage response of conventionally reinforced two-way spanning concrete slab under eccentric impacting drop weight loading. *Defence Technology,* In Press.

Anil Ö, Kantar E, Yilmaz MC (2015). Low velocity impact behavior of RC slabs with different support types. *Construction and Building Materials*, 93, 1078–1088.

Batarlar B, Saatci S (2022). Numerical investigation on the behavior of reinforced concrete slabs strengthened with carbon fiber textile reinforcement under impact loads. *Structures*, 41, 1164–1177.

CEB-FIP Model Code 90 (1993). Comite Euro-International du Beton, Thomas Telford Ltd., London.

Chen W, Hao H, Chen S (2015). Numerical analysis of prestressed reinforced concrete beam subjected to blast loading. *Materials and Design*, 65, 662–674.

Chen W, Pham TM, Elchalakani M, Li H, Hao H, Chen L (2020). Experimental and numerical study of basalt FRP strip strengthened RC slabs under impact loads. *International Journal of Structural Stability and Dynamics*, 2040001.

Daneshvar K, Moradi MJ, Ahmadi K, Hajiloo H (2021). Strengthening of corroded reinforced concrete slabs under multi-impact loading: Experimental results and numerical analysis. *Construction and Building Materials*, 284, 122650.

Do TV, Pham TM, Hao H (2018a). Dynamic responses and failure modes of bridge columns under vehicle collision. *Engineering Structures*, 156, 243–259.

Do TV, Pham TM, Hao H (2018b). Numerical investigation of the behavior of precast concrete segmental columns subjected to vehicle collision. *Engineering Structures*, 156, 375–393.

Fan W, Yuan W, Yang Z, Fan Q (2011). Dynamic demand of bridge structure subjected to vessel impact using simplified interaction model. *Journal of Bridge Engineering*, 16(1), 117–126.

Hao Y, Hao H (2014). Influence of the concrete DIF model on the numerical predictions of RC wall responses to blast loadings. *Engineering Structures*, 73, 24–38.

Hao Y, Hao H, Jiang GP, Zhou Y (2013). Experimental confirmation of some factors influencing dynamic concrete compressive strengths in high-speed impact tests. *Cement and Concrete Research*, 52, 63–70.

Hering M, Bracklow F, Kühn T, Curbach M (2020). Impact experiments with reinforced concrete plates of different thicknesses. *Structural Concrete*, 21(2), 587–598.

Huang Z, Chen W, Tran TT, Pham TM, Hao H, Chen Z, Elchalakani M (2021). Experimental and numerical study on concrete beams reinforced with Basalt FRP bars under static and impact loads. *Composite Structures*, 263, 113648.

Jiang H, Chorzepa MG (2015). An effective numerical simulation methodology to predict the impact response of pre-stressed concrete members. *Engineering Failure Analysis*, 55, 63–78.

Kumar V, Iqbal MA, Mittal AK (2018). Experimental investigation of prestressed and reinforced concrete plates under falling weight impactor. *Thin-Walled Structures*, 126, 106–116.

Li H, Chen W, Hao H (2019). Influence of drop weight geometry and interlayer on impact behavior of RC beams. *International Journal of Impact Engineering*, 131, 222–237.

Li H, Chen W, Hao H (2020). Factors influencing impact force profile and measurement accuracy in drop weight impact tests. *International Journal of Impact Engineering*, 145, 103688.

Li H, Chen W, Pham TM, Hao H (2021). Analytical and numerical studies on impact force profile of RC beam under drop weight impact. *International Journal of Impact Engineering*, 147, 103743.

Li J, Hao H (2013). Influence of brittle shear damage on accuracy of the two-step method in prediction of structural response to blast loads. *International Journal of Impact Engineering*, 54, 217–231.

Li J, Hao H (2014). Numerical study of concrete spall damage to blast loads. *International Journal of Impact Engineering*, 68, 41–55.

Li J, Hao H, Wu C (2017). Numerical study of precast segmental column under blast loads. *Engineering Structures*, 134, 125–137.

Liu B, Fan W, Huang X, Shao X, Kang L (2020). A simplified method to predict damage of axially-loaded circular RC columns under lateral impact loading. *International Journal of Concrete Structures and Materials*, 14(32), 1–24.

Maazoun A, Matthys S, Atoui O, Belkassem B, Lecompte D (2022). Finite element modelling of RC slabs retrofitted with CFRP strips under blast loading. *Engineering Structures*, 252, 113597.

Malvar LJ, Ross CA (1998). Review of strain rate effects for concrete in tension. *ACI Materials Journal*, 95(6), 735–739.

Malvar LJ (1998). Review of static and dynamic properties of steel reinforcing bars. *ACI Materials Journal,* 95(5), 609–616.

Malvar LJ, Crawford JE (1998). Dynamic increase factors for concrete. *DTIC Document*, 1998.

Marzouk HOH (2014). Numerical investigation of reinforced concrete slabs under impact loading. *Proceedings of the 10th Fib International PhD Symposium in Civil Engineering*, Canada.

Mizushima Y, Iino N (2022). Behavior of thin reinforced concrete slabs and effect of reinforcement bars subjected low-velocity impact. *Structures*, 38, 832–847.

Mousavi T, Shafei E (2019). Impact response of hybrid FRP-steel reinforced concrete slabs. *Structures*, 19, 436–448.

Ottosen NS (1977). A Failure Criterion for Concrete. *ASCE Journal of the Engineering Mechanics Division*, 103(4), 527–535.

Radnić J, Matešan D, Grgić N, Baloević G (2015). Impact testing of RC slabs strengthened with CFRP strips. *Composite Structures*, 121, 90–103.

Sadraie H, Khaloo A, Soltani H (2019). Dynamic performance of concrete slabs reinforced with steel and GFRP bars under impact loading. *Engineering Structures*, 191, 62–81.

Said AMI, Mouwainea EM (2022). Experimental investigation on reinforced concrete slabs under high-mass low velocity repeated impact loads. *Structures*, 35, 314–324.

Şengel S, Erol H, Yılmaz T, Anıl Ö (2022). Investigation of the effects of impactor geometry on impact behavior of reinforced concrete slabs. *Engineering Structures*, 263, 114429.

Sha Y, Hao H (2013). Laboratory tests and numerical simulations of barge impact on circular reinforced concrete piers. *Engineering Structures*, 46, 593–605.

Shi C, Zhang J, Zhang J, Shao F, Zhang Y, Zhang M (2021). Experimental study and numerical analysis on impact resistance of civil air defense engineering shear wall. *Advances in Civil Engineering*, 2021, 7376909.

Soltani H, Khaloo A, Sadraie H (2020). Dynamic performance enhancement of RC slabs by steel fibers vs. externally bonded GFRP sheets under impact loading. *Engineering Structures*, 213, 110539.

Thai DK, Kim SE (2014). Failure analysis of reinforced concrete walls under impact loading using the finite element approach. *Engineering Failure Analysis*, 45, 252–277.

Thai DK, Kim SE (2017). Numerical simulation of pre-stressed concrete slab subjected to moderate velocity impact loading. *Engineering Failure Analysis*, 79, 820–835.

Vijay TJ, Kumar MM, Sofia G, Abiraami R (2020). Impact behaviour of reinforced concrete slabs embedded with inclined reinforcements. *Materials Today: Proceedings,* In Press.

Wittmann FH, Rokugo K, Brühwiler E, Mihashi H, Simonin P (1988). Fracture energy and strain softening of concrete as determined by means of compact tension specimens. *Materials and Structures*, 21(1), 21–32.

Yilmaz T, Anıl Ö, Erdem RT (2022). Experimental and numerical investigation of impact behavior of RC slab with different opening size and layout. *Structures*, 35, 818–832.

Yilmaz T, Kiraç N, Anil Ö (2019). Experimental investigation of axially loaded reinforced concrete square column subjected to lateral low-velocity impact loading. *Structural Concrete*, 20(4), 1358–1378.

Yılmaz T, Kirac N, Anil Ö, Erdem RT, Kacaran G (2020). Experimental investigation of impact behaviour of RC Slab with different reinforcement ratios. *KSCE Journal of Civil Engineering*, 24(1), 241–254.

Yılmaz T, Kıraç N, Anil Ö, Erdem RT, Sezer C (2018). Low-velocity impact behaviour of two way RC slab strengthening with CFRP strips. *Construction and Building Materials*, 186, 1046–1063.

Yılmaz T, Kıraç N, Anıl Ö, Erdem RT, Hoşkal V (2020). Experimental and numerical investigation of impact behavior of reinforced concrete slab with different support conditions. *Structural Concrete*, 21(6), 2689–2707.